Pontifícia Universidade Católica
do Rio de Janeiro

Jessica Gil Londoño

Nano-TiO_2-based charge transfer complexes with oxygen vacancies for visible light photocatalytic processes

Dissertação de Mestrado

Dissertation presented to the Programa de Pós–graduação em Engenharia Química, de Materiais e Processos Ambientais, do Departamento de Engenharia Química e de Materiais of PUC-Rio in partial fulfillment of the requirements for the degree of Mestre em Engenharia Química, de Materiais e Processos Ambientais.

Advisor: Prof. Bojan Marinkovic

Rio de Janeiro
November 2022

Pontifícia Universidade Católica
do Rio de Janeiro

Jessica Gil Londoño

Nano-TiO$_2$-based charge transfer complexes with oxygen vacancies for visible light photocatalytic processes

Dissertation presented to the Programa de Pós–graduação em Engenharia Química, de Materiais e Processos Ambientais of PUC-Rio in partial fulfillment of the requirements for the degree of Mestre em Engenharia Química, de Materiais e Processos Ambientais. Approved by the Examination Committee:

Prof. Bojan Marinkovic
Advisor
Departamento de Engenharia Química e de Materiais – PUC-Rio

Prof. Jordi Llorca Piqué
Universitat Politècnica de Catalunya (UPC)

Dir. Rech. Vincent Goetz
Universidade de Perpignan Via Domitia (UPVD)

Prof. Anderson Gabriel Marques da Silva
Pontifícia Universidade Católica PUC-Rio

Rio de Janeiro, November 30th, 2022

Jessica Gil Londoño

Graduated in physics from the Universidad del Valle, Cali, Colombia in 2019: laureate thesis entitled *Study of coherence properties and interferometry based on Bose-Einstein Condensates*. Participation and recognition in different research projects and national/international conferences.

Bibliographic data

Gil Londoño, Jessica

Nano-TiO_2-based charge transfer complexes with oxygen vacancies for visible light photocatalytic processes / Jessica Gil Londoño; advisor: Bojan Marinkovic. – 2022.

94 f: il. color. ; 30 cm

Dissertação (mestrado) - Pontifícia Universidade Católica do Rio de Janeiro, Departamento de Engenharia Química e de Materiais, 2022.

Inclui bibliografia

1. Engenharia Química e de Materiais – Teses. 2. TiO_2-ACAC. 3. TiO_2-GA. 4. Complexos de Transferência de Carga. 5. Espécies Reativas de Oxigênio. 6. Vacâncias de Oxigênio. 7. Fotodegradação. I. Marinkovic, Bojan. II. Pontifícia Universidade Católica do Rio de Janeiro. Departamento de Engenharia Química e de Materiais. III. Título.

CDD: 620.11

“La vida no es la fiesta que habíamos imaginado, pero ya que estamos aquí,
bailemos.” : Fernando Aramburu.
To my parents, Carlina Londoño Duque and Josafat Humberto Gil Marín.
To my brothers Katherine Gil and Edward Gil, To Patrick Petit and Jacob.
In memorian of Martha and Carlos.

Acknowledgments

To my advisor, Prof. Bojan Marinkovic, for opening the doors of his office for me whenever I needed to discuss my work, for reading my articles and my dissertation carefully and thoroughly, for the feedback and for the time dedicated to the long discussions we had, for allowing me to teach him what I was learning because, as he says: “a good advisor is one who learns from his students”.

To the evaluation committee, professors Jordi Llorca Piqué, Vincent Goetz and Anderson Gabriel Marques da Silva. Thank you for taking the time to read this dissertation.

To our collaborators, professors Marco Cremona, Klaus Krambrock, Marcelo E.H. Maia da Costa, Omar Ginoble Pandoli and researchers Raphaela de Oliveira, Druval Santos de Sá and Rafael dos Santos Carvalho for allowing me to use their equipment to characterize my samples and for their willingness to discuss some of my results and for the feedback.

To Lidija Mancic and the laboratory staff Anja Donsen, Juliana Viol, Emanuel Pessanha and Henrique Meira da Silva for their confidence, teachings and continuous support during the development of this research.

To my friends from the physics department Lanna, Thais, Aline, Lucas, João, Caique, Junior, Livio, Fredy and especially to Juan David, for opening the doors of their houses, their laboratories and, mainly, for giving me a family in Brazil.

To the professors of the physics department Isabel Cristina dos Santos Carvalho, Alexander Argüello Quiroga for opening the doors of their laboratories to me, for the coffee time and for the support. I am especially grateful to professor Marco Cremona, who took the time not only to talk about research and academic life, but also to show me the Pontifical Catholic University of Rio de Janeiro (PUC-Rio) and the different postgraduate programs that it offers. Without him, I probably would not have ventured to do a postgraduate course at PUC-Rio.

To my Salsa friends in Brazil Carolina, Tito, Sonia, Francisco, Nestor, Victor and Plinio, for sharing their passion for music and dance with me. To my other friends, especially to Laura, Angie, Camila, Angélica, Mario, Astrid, Diana, Lorena, Priscila and professors César and Efrain for their words of support and motivation, for believing in my work and for their friendship.

To the Pontifical Catholic University of Rio de Janeiro for the tuition exemption, for access to the equipment, personnel and infrastructure that allowed me to grow professionally and personally.

To ANP (National Agency of Petroleum, Natural Gas and Biofuels), Finep (Funding Authority for Studies and Projects) and MCTI (Ministry of Science, Technology and Innovation) for the master degree scholarship, provided through the ANP Human Resources Program for the Oil and Gas Sector – PRH-ANP/MCTI.

To my family. To my parents Carlina and Humberto, to my brothers Katherine and Edward, to Patrick Petit, Jacob, the Petit family, Rosalba, Sandra Jiménez and Delia Burgos for making possible each stage of this journey called life, for their support, for teaching me with their examples the meaning of the words love, discipline, unconditionality, honesty, responsibility, hard work and excellence. Thank you because each of their efforts have been valuable. This is my greatest token of gratitude to them. Therefore, this research is by them and for them!

This study was financed in part by the Coordenação de Aperfeiçoamento de Pessoal de Nível Superior - Brasil (CAPES) - Finance Code 001. Additionally, this study was partially financed with monetary resources from Project FINEP 605 (PUC-Rio Intersecretarial Oil and Gas Program) - PRH-ANP – Agreement 01.19.0211.00 (ANP Human Resources Training Program for the Oil, Natural Gas and Biofuels Sector).

Abstract

Gil Londoño, Jessica; Marinkovic, Bojan (Advisor). **Nano-TiO_2-based charge transfer complexes with oxygen vacancies for visible light photocatalytic processes**. Rio de Janeiro, 2022. 94p. Dissertação de Mestrado – Departamento de Engenharia Química e de Materiais, Pontifícia Universidade Católica do Rio de Janeiro.

TiO_2-based visible-light-sensitive nanomaterials are widely studied for photocatalytic applications under UV-Vis radiation. Among the mechanisms of visible light sensitization, extrinsic oxygen vacancies have been introduced into TiO_2 and charge transfer complexes (CTCs) have been formed between chelating ligands, such as acetylacetone, and nanocrystalline TiO_2 (TiO_2-ACAC). On the other hand, it was found in the literature that nanocrystalline anatase-coupled glutaric acid (TiO_2-GA) exhibits high photocatalytic efficiency under UV due to its high surface area. However, the influence of extrinsic oxygen vacancies on the photocatalytic performance of TiO_2-based CTCs is unknown and the sensitization of TiO_2 to visible light by functionalization with glutaric acid (TiO_2-GA) and its photocatalytic performance under visible light radiation have not yet been investigated. In this work, surface/bulk extrinsic oxygen vacancies were introduced into TiO_2-ACAC through calcination at 270 °C under static air, Ar and H_2 atmospheres and visible-light-sensitive TiO_2-GA nanomaterials were synthesized *via* sol-gel and calcined under static air at 270 °C. TiO_2-ACAC and TiO_2-GA CTCs were characterized by XRPD, FTIR, TGA, DRS, PL, EPR and XPS techniques. FTIR results proved the formation of the CTC through bidentate chelating interaction between TiO_2 and GA. TiO_2-GA CTCs calcined at 270 °C under static air exhibited a long absorption tail in the visible light spectrum due to the formation of F^+ centers and bulk Ti^{3+} defects. Tetracycline (TC) photodegradation using scavengers and the correlation with EPR-spin trapping highlighted the key role of the superoxide radical in the TC degradation by TiO_2-ACAC and TiO_2-GA CTCs under low-power visible light radiation. The increased extrinsic oxygen vacancies concentration was not beneficial for photocatalytic performance of TiO_2-ACAC CTCs, since bulk extrinsic oxygen vacancies additionally acts as recombination centers. In fact, the TiO_2-ACAC CTC with the lowest extrinsic oxygen vacancies concentration exhibited the highest photocatalytic performance for TC degradation due to an adequate distribution of extrinsic bulk oxygen vacancies, which led to the trapped electrons undergoing repeated hopping, reducing the recombination rates and improving the efficiency in the superoxide radicals production. On the other hand, the high content of GA organic molecule ineffectively bounded to the TiO_2 surface were not beneficial for photocatalytic performance of TiO_2-GA CTCs, since the organic molecule that is not effectively bounded to the TiO_2 surface reduced the active sites in the TiO_2-GA nanostructure. Our findings indicated that TiO_2-ACAC and TiO_2-GA CTCs are able to degrade pollutants *via* interactions with electronic holes and principally superoxide radicals and also, provided fundamental information about the influence of surface/bulk extrinsic oxygen vacancies on photocatalytic performance, lattice parameters, optical and photochemical properties of TiO_2-based CTCs.

Keywords

TiO_2-ACAC; TiO_2-GA; Charge-Transfer Complexes; Reactive Oxygen Species; Oxygen Vacancies; Photodegradation.

Resumo

Gil Londoño, Jessica; Marinkovic, Bojan. **Complexos de transferência de carga baseados em nano-TiO_2 com vacâncias de oxigênio para processos fotocatalíticos à luz visível**. Rio de Janeiro, 2022. 94p. Dissertação de Mestrado – Departamento de Engenharia Química e de Materiais, Pontifícia Universidade Católica do Rio de Janeiro.

Os nanomateriais sensíveis à luz visível baseados em TiO_2 são amplamente estudados para aplicações fotocatalíticas sob radiação UV-Vis. Entre os mecanismos de sensibilização à luz visível, vacâncias de oxigênio extrínsecas foram introduzidas em TiO_2 e complexos de transferência de carga (CTCs) foram formados entre ligantes quelantes, como acetilacetona, e TiO_2 nanocristalino (TiO_2-ACAC). Por outro lado, foi encontrado na literatura que o ácido glutárico acoplado à anatase nanocristalina (TiO_2-GA) apresenta alta eficiência fotocatalítica sob UV devido à sua alta área superficial. No entanto, a influência das vacâncias de oxigênio extrínsecas no desempenho fotocatalítico dos CTCs à base de TiO_2 é desconhecida e a sensibilização do TiO_2 à luz visível por funcionalização com ácido glutárico (TiO_2-GA) e seu desempenho fotocatalítico sob radiação de luz visível ainda não foram investigados. Neste trabalho, vacâncias de oxigênio extrínsecas de superfície/volume foram introduzidas em TiO_2-ACAC através de calcinação a 270 °C sob ar estático, atmosferas de Ar e H_2 e nanomateriais de TiO_2-GA sensíveis à luz visível foram sintetizados *via* sol-gel e calcinados sob ar estático a 270 °C. Os CTCs de TiO_2-ACAC e TiO_2-GA foram caracterizados pelas técnicas de XRPD, FTIR, TGA, DRS, PL, EPR e XPS. Os resultados de FTIR comprovaram a formação do CTC através da interação quelante bidentada entre TiO_2 e GA. Os CTCs de TiO_2-GA calcinados a 270 °C sob ar estático exibiram uma longa cauda de absorção no espectro de luz visível devido à formação de centros F^+ e defeitos Ti^{3+}. A fotodegradação da tetraciclina (TC) usando sequestrantes e a correlação com EPR-spin trapping destacaram o papel fundamental do radical superóxido na degradação da TC pelos CTCs de TiO_2-ACAC e TiO_2-GA sob radiação de luz visível de baixa potência. O aumento da concentração de vacâncias de oxigênio extrínsecas não foi benéfico para o desempenho fotocatalítico dos CTCs de TiO_2-ACAC, uma vez que as vacâncias de oxigênio extrínsecas no volume também atuam como centros de recombinação. De fato, o CTC de TiO_2-ACAC com a menor concentração de vacâncias de oxigênio extrínsecas exibiu o maior desempenho fotocatalítico para degradação da TC devido a uma distribuição adequada de vacâncias de oxigênio extrínsecas no volume, o que fez com que os elétrons aprisionados sofressem saltos repetidos, reduzindo as taxas de recombinação e melhorando a eficiência na produção de radicais superóxido. Por outro lado, o alto teor de molécula orgânica de GA ineficientemente ligada à superfície do TiO_2 não foi benéfica para o desempenho fotocatalítico dos CTCs de TiO_2-GA, uma vez que a molécula orgânica que não é efetivamente ligada à superfície do TiO_2 reduziu os sítios ativos na nanoestrutura de TiO_2-GA. Nossas descobertas indicaram que os CTCs de TiO_2-ACAC e TiO_2-GA são capazes de degradar poluentes *via* interações com buracos eletrônicos e principalmente radicais superóxido e também forneceram informações fundamentais sobre a influência das vacâncias de oxigênio extrínsecas de superfície/volume no desempenho fotocatalítico, parâmetros de rede, propriedades ópticas e fotoquímicas dos CTCs baseados em TiO_2.

Palavras-chave

TiO_2-ACAC; TiO_2-GA; Complexos de Transferência de Carga; Espécies Reativas de Oxigênio; Vacâncias de Oxigênio; Fotodegradação.

Table of contents

List of figures

List of tables

List of Abreviations

ACAC – Acetylacetone

BC – Black carbon BET – Brunauer-Emmett-Teller

BQ – Benzoquinone

CB – Conduction band

CFCs – Chlorofluorocarbons

CTC – Charge-transfer complex

DRS – Diffuse reflectance spectroscopy

DSC – Differential scanning calorimetry

DTG – Derivative Thermogravimetry

EPR – Electron paramagnetic resonance

FTIR – Fourier transform infrared spectroscopy

GA – Glutaric acid

HOMO – Highest occupied molecular orbital

IPA – Isopropyl alcohol or isopropanol

LED – Light-emitting diode

LMCT – Ligand-to-metal charge transfer

PL – Photoluminescent emission spectroscopy

ROS – Reactive oxygen species

SETOV – Single-electron-trapped oxygen vacancy

TC – Tetracycline

TGA – Thermogravimetric analysis

UV – Ultraviolet

UV-VIS Ultra violet-visible spectroscopy

VB – Valence band

XRPD – X-ray Powder diffraction

Je suis de ceux qui pensent que la science a une grande beauté. Un scientifique dans son laboratoire est non seulement un technicien : il est aussi un enfant placé devant des phénomènes naturels qui l'impressionnent comme des contes de fées.

Marie Curie, *Madame Curie, Ève Curie.*

1
Introduction

Semiconductor-based nanomaterials such as TiO_2 have attracted the interest of researchers and industry due to their potential applications for environmental remediation through the activation of photocatalytic processes [11, 12], which allow the photodegradation of pollutants [13, 14] and the generation of H_2 from water splitting [3].

Anatase is the most stable TiO_2 phase for nanoparticles smaller than 14 nm [15] and it is also the TiO_2 phase that has shown the highest photocatalytic efficiency [16, 17]. However, its low absorption of visible light [3] is the main limitation for the application of photocatalysts, that can be excited through renewable and sustainable energy sources such as solar radiation [14].

In order to solve this limitation and to promote visible light photocatalytic processes, charge transfer complexes were synthesized in this study *via* sol-gel through the anchoring of small organic molecules, such as acetylacetone and glutaric acid, at the anatase TiO_2 surface. Additionally, the influence of point defects (oxygen vacancies) on the photocatalytic performance, optical and photochemical properties of TiO_2-based complexes were studied.

As the authors are aware, the influence of oxygen vacancies on the photocatalytic performance of TiO_2-Acetylacetone and the sensitization of TiO_2 to visible light by functionalization with glutaric acid and its photocatalytic performance under visible light radiation have not yet been investigated. Therefore, this dissertation arises from the interest in filling these knowledge gaps.

This document is structured in 7 chapters, including the introduction. In chapter §2, the fundamentals of photocatalytic process and the mechanisms that will be used to synthesize TiO_2-based visible-light-sensitive nanomaterials are succinctly presented. Chapter §3 is focused on the proposal of this research work. Chapter §4 describes the synthesis and characterization techniques of the charge transfer complex formed between TiO_2 and Acetylacetone. In addition, this chapter presents the study of the extrinsic oxygen vacancies in TiO_2-Acetylacetone charge transfer complex and their effects on optical and photochemical properties. In chapter §5, the synthesis processes of the charge transfer complexes formed between TiO_2 and Glutaric acid are described and the study of the functionalization of anatase nanoparticles with Glutaric acid and their photochemical and photocatalytic properties are presented. Finally, Chapter §6 presents the general conclusions and prospects for future works and Chapter §7 contains the bibliographical references.

2
Previous work

2.1
Environmental pollution and antibiotic residues in wastewater

In recent years, the presence of drugs and pharmaceuticals products in water has generated a worldwide concern, being classified as emerging contaminants [18, 19] due to the presence of high levels of biologically active residual antibiotics with high biological stability and high hydrophilicity [20], resulting in ecological toxicity and extreme antibiotic resistance [21]. Among broad-spectrum antibiotics, tetracycline (TC) is one of the most widely used antibiotics in humans [22] and is also used as a growth promoter in animals [20, 23]. However, more than 50% of tetracycline is not absorbed by humans and animals. Therefore, the removal of tetracycline antibiotic residues from wastewater becomes important, since the high concentration of these metabolites, transmitted mainly through the food chain (Figure 2.1), can generate potential long-term adverse effects for human health and for ecosystems [24, 25]. Traditional methods to treat antibiotics, such as tetracycline, have low efficiency [23, 26] and some of them are expensive and require high energy consumption [20].

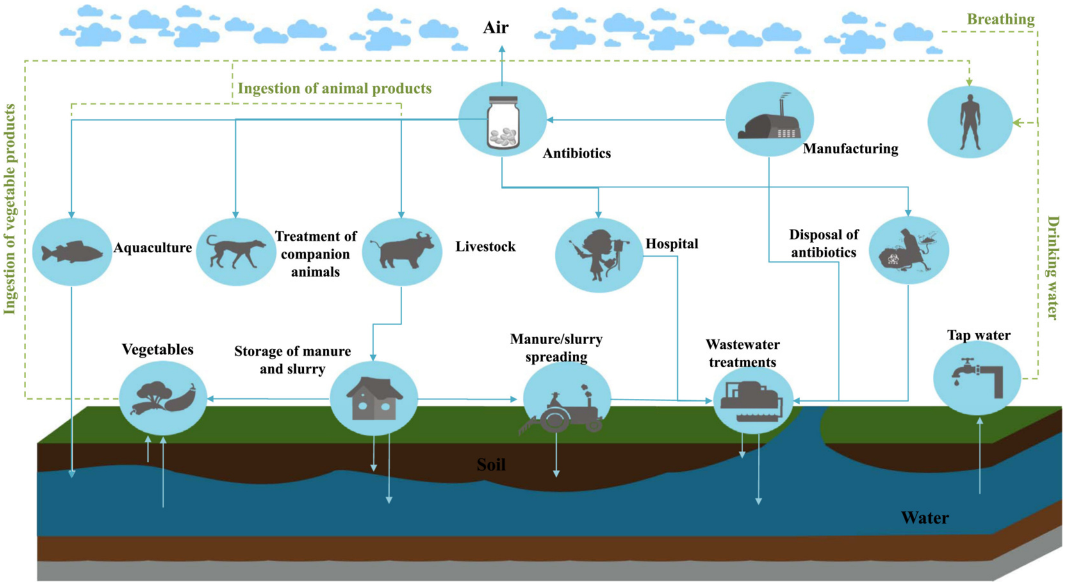

Figure 2.1: Human exposure to antibiotic metabolites coming from antibiotic residues in the environment. [1].

In this context, photocatalysis emerges as an alternative and sustainable method to degrade this type of pollutants due to its low cost, high efficiency and low energy consumption. Additionally, this method allows for reducing or eliminating the antibacterial activity of antibiotics. Table 2.1 summarize the advantages, disadvantages and influencing parameters of the different methods to TC removal.

Table 2.1: Comparison between tetracycline removal methods. Table taken from the reference [10].

Method	**Advantages**	**Disadvantages**	**Influencing parameters**
Ozonation	High process efficiency Lesser O_3 consumption Environmentally safe, i.e., no sludge production Improve efficiency by catalyst utilization	High cost Lesser solubility in water Possible production of carcinogenic by-product (bromate) Mass transfer limitation	Ozone dose pH and temperature of the reaction medium Type of catalyst Initial TC concentration
Fenton process	High performance Simplicity Non-toxic Environmentally safe end products generation, i.e., H_2O, O_2 Possibility of catalyst utilization to improve the efficiency Possibility of combination with other non-biodegradable methods to improve efficiency	Strict pH range High H_2O_2 consumption Ferric sludge generation	Operating pH and temperature Ferrous ion concentration H_2O_2 concentration Initial TC concentration
Photolysis / Photocatalysis	Reaction conditions easily met Complete decomposition of organic matter Strong redox ability Low cost Long durability No adsorption saturation Potential upscale possibility	Inefficient visible light utilization Rapid degradation of photogenerated intermediate compounds Mass transfer limitations	Intensity of radiation Type of catalysts Water hardness pH Redox conditions Initial TC concentration Humic acid concentration
Sonolysis / sonochemical oxidation	Green or safe technique No or negligible secondary pollution Ultrasound waves clean catalyst surface thereby increasing catalyst efficiency Low cost reactors In combination with Fenton process reduce sludge generation	Non-selective mechanism High energy consumption High maintenance cost	Ultrasonic power pH Initial TC concentration Reaction time Redox potential

Photocatalysis is also a promising alternative for the development of cleaner energy through the H_2 production [27, 28, 3], for the removal of NO_x [29], sulfur and gaseous sulfur dioxide [13], for bacterial inactivation [30, 31, 32] and for the reduction of CO_2, CH_4, chlorofluorocarbons (CFCs), tropospheric O_3, black carbon (BC) and other major contributors to climate change [14, 33].

2.2
Fundamentals of the photocatalytic process

The main goal of current research in photocatalysis is related to the use of energy from renewable sources, such as the sun, through which chemical reactions can be accelerated, contributing to environmental remediation [11, 12].

Photocatalytic processes, shown in Figure 2.2, involve a series of oxidation and reduction (redox) reactions at the semiconductor surface, promoted through the light absorption with energy higher than the band-gap energy of the semiconductor material. As a result of photoexcitation of the semiconductor, electrons (e^-) are excited from the valence band (VB) to conduction band (CB) and electronic holes (h^+) are generated in the valence band of the semiconductor. The photogenerated charge carriers can undergo different pathways: (1) migration of charge carriers to the surface and (2) recombination of e^-/h^+ pair at the surface/bulk of the semiconductor.

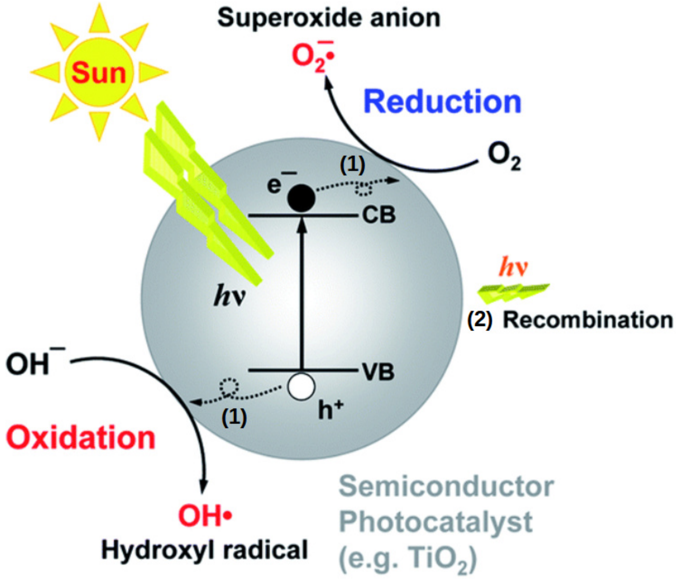

Figure 2.2: Mechanisms involved in the photocatalytic process. Imagen adapated from [2].

The migration of photogenerated charge carriers to the surface leads to the generation of reactive oxygen species (ROS), such as superoxide ($O_2^{-\bullet}$) and hydroxyl ($OH^\bullet$) radicals, as a consequence of the reducing and oxidizing oxygen and water molecules, originating from the reaction medium. These types of radicals decompose organic and inorganic compounds adsorbed on the semiconductor surface [7]. The main reactions of the photodegradation of pollutants in the presence of a metal oxide semiconductor are described below [14]:

$$\text{Semicondutor} + h\nu \rightarrow e^- + h^+ \tag{2-1}$$

$$O_2 + e^- \rightarrow O_2^{-\bullet} \tag{2-2}$$

$$H_2O + h^+ \rightarrow H^+ + OH^\bullet \tag{2-3}$$

$$O_2^\bullet + H^+ \rightarrow HO_2^\bullet \tag{2-4}$$

$$HO_2^\bullet + HO_2^\bullet \rightarrow H_2O_2 + O_2 \tag{2-5}$$

$$e^-/h^+ \overset{O_2/H_2O}{\rightarrow} \text{ROS} \overset{\text{Pollutant}}{\rightarrow} \text{Inorganic prod} \tag{2-6}$$

2.3
TiO_2-based photocatalytic materials

Photocatalytic reactions are promoted in the semiconductor material only if the electronic band structure of the semiconductor satisfies some of the following conditions:

- The minimum energy level of the conduction band must be more negative than the redox potential of the acceptor species.
- The maximum energy level of the valence band must be more positive than the redox potential of the donor species.

TiO_2 is the most widely used semiconductor for photocatalytic applications since it satisfies the condition previously described, as shown in Figure 2.3, and also due to its high chemical stability, non-toxicity, low production cost and chemical compatibility [34].

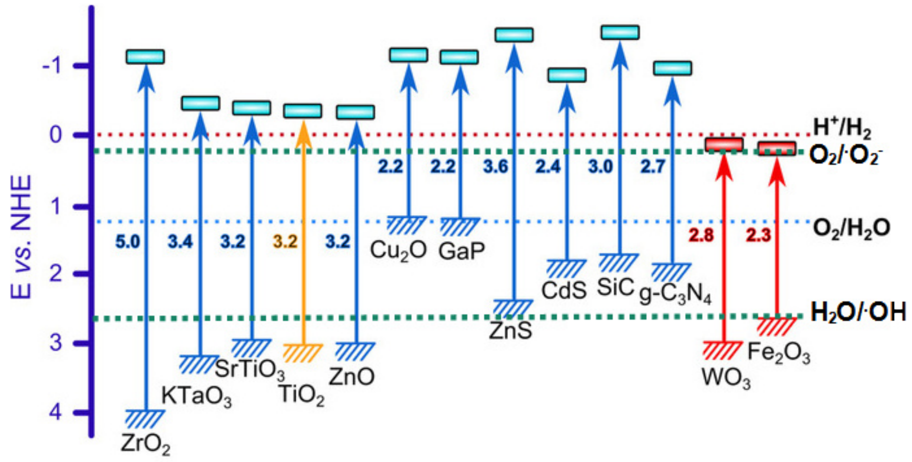

Figure 2.3: Band-gap energies and position of the CB and VB edges of different semiconductors in relation to the redox potentials of water splitting and ROS species. Imagen adapted from [3].

TiO_2 can adopt 11 different crystal structures [35]. However, the main crystalline polymorphs of titania are anatase, rutile and brookite. Although rutile is thermodynamically stable, the phase stability of titania is a function of particle size, with anatase being the most stable phase for nanoparticles smaller than 14 nm [15]. Anatase and rutile are the most widely used TiO_2 polymorphs in photocatalysis applications. The difference of these crystal structures can be described by different arrangements of their (TiO_6) octahedra. The crystal structures of rutile and anatase have a tetrahedral structure. However, the octahedra are edge and vertex-connected for rutile, while for anatase, the octahedra are vertex-connected, as shown in Figure 2.4.

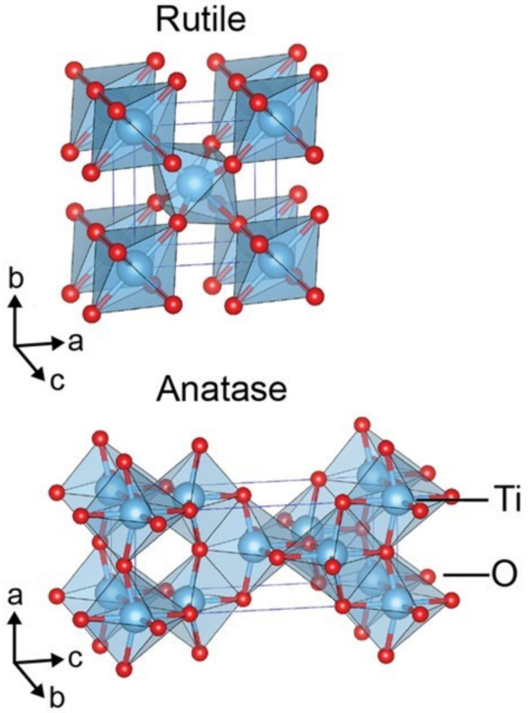

Figure 2.4: Crystal structure motifs of Anatase and Rutile. Image adapated from [4].

Anatase exhibits better photocatalytic efficiency due to higher density of active sites on the surface [16] and long electron-hole pair lifetime compared to rutile [17]. However, TiO_2, like other semiconductor materials, has intrinsic limitations associated with low light absorption in the visible spectrum and high recombination rate of photogenerated charge carriers [3, 14, 34].

2.4
Visible light sensitization of TiO_2

In order to use the renewable source such as solar radiation, whose emission in the visible spectrum corresponds to 44%, to activate the photocatalytic processes, different mechanism to sensitize TiO_2 to visible light have been studied [14, 36, 37].

Among the mechanisms of visible light sensitization, the introduction of extrinsic oxygen vacancies [38, 39, 40, 41, 42] and the functionalization of nanomaterials by anchoring organic molecules at the nanomaterial surface [8, 43, 44, 45, 46, 47] are being developed, since organic molecules, such as diketones and dicarboxylic acids, can form charge transfer complexes (CTC) with the nanocrystalline TiO_2 *via* chelating ligands.

On the other hand, studies conducted by Scolan et al. [48] and Siwińska et al. [49] have revealed that the hydrolysis-condensation rates of the metal alkoxide can be controlled through the addition of the chelating ligands, such as acetylacetone (ACAC), during sol-gel synthesis, allowing the synthesis of metal oxides with smaller crystallite sizes and consequently, with high specific surface area.

2.5
Sol-gel as a versatile synthesis route to produce metal oxide nanostructures

Sol-gel is a widely used wet chemistry method to produce ceramic nanoparticles in general and is also one of the most versatile synthesis routes to obtain metal oxides nanostructures due to its relatively low complexity, low energy cost and high control of the reaction pathways, which allow synthesizing different types of nanostructures with several shapes and high homogeneity [5, 50, 51]. In this synthesis method, inorganic and organic-inorganic hybrid nanomaterials are obtained through water-induced polymerization reactions. The main steps involved in the sol-gel synthesis method are hydrolysis, polycondensation and gelation [5]. Figure 2.5 shows the steps involved in the sol-gel route and its versatility.

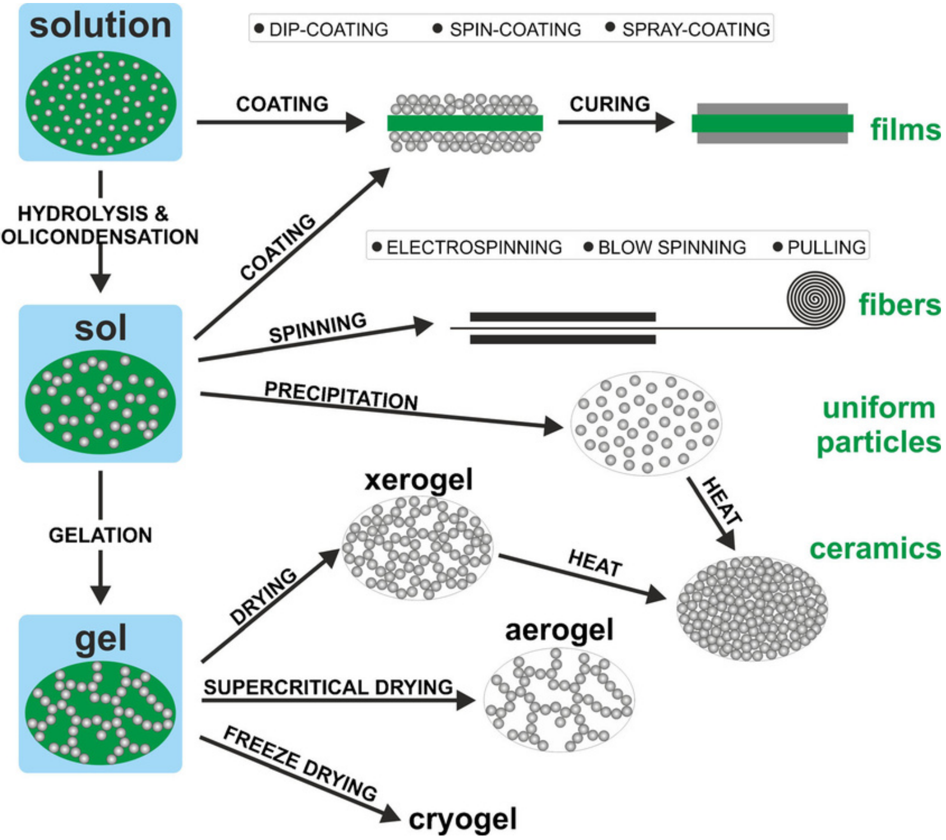

Figure 2.5: Steps of the sol-gel synthesis route and different products obtained by this synthesis method [5].

The TiO_2 nanopowders are obtained *via* sol-gel route, using titanium (IV) isopropoxide, as metal alkoxide precursor, dissolved in ethanol and mixed with an acidic aqueous solution to promote hydrolysis and condensation reactions [43, 52, 53]. During hydrolysis, titanium alkoxide (TiOR) reacts with water, substituting alkoxy groups (OR) for hydroxyl groups (OH) (Equation 2-7), coming from water [54]. Simultaneously, the condensation process is activated, forming a colloidal suspension (sol), this reaction mechanism involves the bonding between metal hydroxide groups, which causes a hydrated metal-oxide network (Equation 2-8) [54]. The condensation process proceeds, increasing the polymeric chains and the viscosity, leading to the formation of the gel (network in continuous liquid phase).

$$\mathrm{TiOR} + \mathrm{mH_2O} \rightarrow \mathrm{Ti(OR)}_{4-m}(\mathrm{OH})_m + m\mathrm{ROH} \tag{2-7}$$

$$\begin{gathered} \mathrm{Ti-OH + OR - Ti \rightarrow Ti - O - Ti + ROH} \\ \mathrm{Ti-OH + OH - Ti \rightarrow Ti - O - Ti + H_2O} \end{gathered} \tag{2-8}$$

Metal alkoxides, such as titanium (IV) isopropoxide, are very reactive, giving rise to long polymer chains that make difficult the obtaining of titanium nanoparticles *via* the sol-gel synthesis route [48, 52, 54]. To obtain nanoparticles with desirable properties, chelating ligands, such as diketones and carboxylic acid, have been added during the sol-gel synthesis process. Scolan et al. [48] and Siwińska et al. [49] showed that the addition of these complexing agents allows to control the hydrolysis and polycondensation rates, giving rise to the formation of nanoparticles. In fact, Scolan et al. [48] reported that increasing of the complexing ratio $\left(\frac{[ACAC]}{[Ti]}\right)$, using acetylacetone as complexing agent, from 1 to 5 led to a reduction in the nanoparticles size from 7 to 1.5 nm. Habran et al. [52] synthesized nanoparticles with a diameter of $\sim$4 nm using acetylacetone, as a complexing agent, and a complexing ratio of 2.

2.6
Visible light sensitization of anatase through extrinsic oxygen vacancies: colour centers

The physicochemical properties of materials can be tuned through defects formation. Oxygen vacancies ($\mathrm{V_O^{\bullet\bullet}}$ - oxygen ion missing from its lattice site), titanium vacancies ($\mathrm{V_{Ti}^{''''}}$ - titanium ion missing from its lattice site), oxygen interstitial ($\mathrm{O_i^{''}}$ - oxygen ion located at an interstitial lattice site) and titanium interstitial ($\mathrm{Ti_i^{\bullet\bullet\bullet\bullet}}$ - titanium ion located at an interstitial lattice site) are the common point defects found in $\mathrm{TiO_2}$ [55].

$\mathrm{V_O^{\bullet\bullet}}$ is one of the most common point defects on titania reported in the literature due to its low formation enthalpies [55], therefore, its relative ease of creation [7]. Among all the synthesis methods to create oxygen vacancies in the TiO_2 structure, thermal treatments under reducing atmospheres are one of the most used approaches [7].

Ceramic ionic materials, such as TiO_2, must maintain charge neutrality [56]. Therefore, using the standard Kröger-Vink notation, the defect equilibria of oxygen vacancies formation in titania could be governed through a charge balance described by the following equation [38, 55, 57]:

$$2\mathrm{O}_\mathrm{O}^\mathrm{x} \Longleftrightarrow 2\mathrm{V}_\mathrm{O}^{\bullet\bullet} + 4\mathrm{e}' + \mathrm{O}_2. \tag{2-9}$$

The formation of the oxygen vacancy in TiO_2 involves the creation of the color centers, called F-centers (from Farbe, the German word for color), where the oxygen vacancy site can be occupied by zero, one or two electrons, leading to the formation of color centers F^{++}, F^{+} and F [55, 58], respectively:

$$\mathrm{V}_\mathrm{O} + 0\mathrm{e}^- = \mathrm{V}_\mathrm{O}^{\bullet\bullet} \equiv \mathrm{F}^{++}. \tag{2-10}$$

$$\mathrm{SETOV} = \mathrm{V}_\mathrm{O} + 1\mathrm{e}^- = \mathrm{V}_\mathrm{O}^{\bullet} \equiv \mathrm{F}^{+} \tag{2-11}$$

$$\mathrm{V}_\mathrm{O} + 2\mathrm{e}^- = \mathrm{V}_\mathrm{O}^{\mathrm{x}} \equiv \mathrm{F} \tag{2-12}$$

Additionally, depending on the formation mechanism and defect equilibria, oxygen vacancies in titania could also lead to the presence of divalent and trivalent titanium [6, 59], as shown in Figure 2.6.

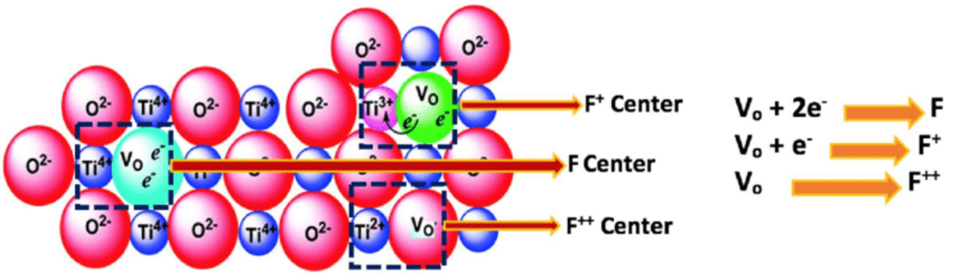

Figure 2.6: Charge compensation process in oxygen deficient TiO_2. Creation of F-centers, divalent and trivalent titanium [6].

Therefore, oxygen vacancies have a direct effect on the electronic structure and, consequently, on the optical properties of TiO_2, since the F-centers and trivalent titanium form donor levels below the conduction band of titania, sensitizing TiO_2 to visible light [6, 38]. Oxygen vacancies in TiO_2, also affect the structure of titania. In fact, other authors have related that the oxygen vacancies induce changes in the binding energies of titanium and oxygen atoms and have also observed lattice distortions in the TiO_2 unit-cell [38, 39, 40, 60].

Some authors have reported that the photocatalytic performance of TiO_2 can be described as a function of the location and concentration of oxygen vacancies, since bulk oxygen vacancies act as recombination centers while surface oxygen vacancies act as electron traps and active sites, improving the photocatalytic performance [7, 40, 41, 61], as shown in pathways (4) and (6) in Figure 2.7.

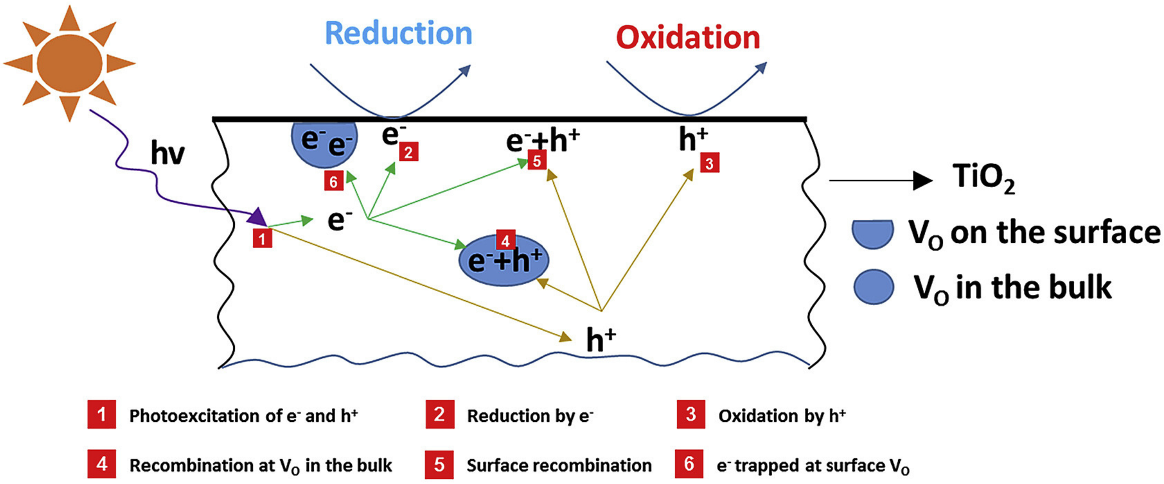

Figure 2.7: Pathways of charge migration and/or recombination in oxygen-deficient TiO_2 under photoexcitation. [7].

2.7
Visible light sensitization of TiO_2 by coupling with chelanting ligands: ligand-to-metal charge transfer (LMCT) mechanism

The photosensitization of TiO_2 to visible light with organic molecule such as acetylacetone [8, 43, 44], cathecol [45], dopamine [46] and carboxylic acids [47], such as glutaric acid (GA), is generated *via* the ligand-to-metal charge transfer (LMCT) mechanism. In this mechanism, electrons are transferred from the highest occupied molecular orbital (HOMO) of the organic molecule to the conduction band (CB) of the semiconductor (transition (1) in Figure 2.8) [8, 62], increasing the light absorption capacity of the semiconductor material in the visible spectrum.

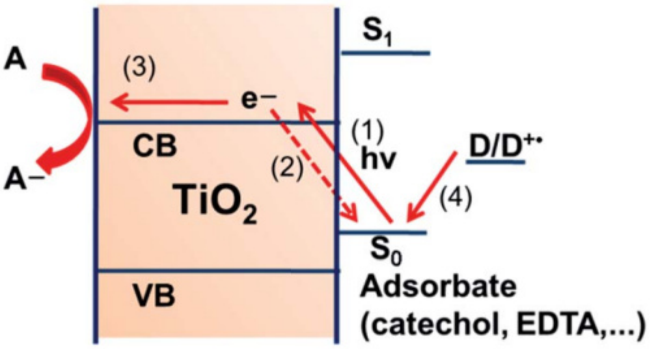

Figure 2.8: LMCT mechanism [8].

As a result of the electronic transition generated in the LMCT mechanism, electronic holes are generated in the HOMO of the organic molecule, being able to recombine with e^- (transition (2) in Figure 2.8) and/or migrate to the surface to interact with donor species (transition (4) in Figure 2.8). In addition, electrons in CB are being able to migrate to the surface to interact with acceptor species (transition (3) in Figure 2.8).

The LMCT mechanism have been widely reported for TiO_2-based nanomaterials [8, 43, 44, 45, 46, 47] and also for other semiconductors materials, such as Mg_2TiO_4 [63] and Fe alkoxide [64]. Sannino et al. [44], Habran et al. [52] and Almeida et al. [43] photosensitized TiO_2 to visible light using acetylacetone as complexing agent (TiO_2-ACAC). However, Sannino et al. [44] obtained the TiO_2-ACAC charge transfer complex (CTC) in amorphous state following a different synthesis route than the one proposed in this work. Habran et al. [52] and Almeida et al. [43] obtained crystalline TiO_2-ACAC CTCs and observed the presence of oxygen vacancies in the CTCs. However, the work carried out by these authors did not focus on studying the effects of oxygen vacancies on the physicochemical properties and on the photocatalytic performance of TiO_2-ACAC CTCs.

On the other hand, among all the studies carried out on the functionalization of TiO_2 by anchoring carboxylic acids on the nanomaterial surface, only four studies on the interaction between GA and TiO_2 surface have been reported [65, 66, 67, 68]. Zapata-Tello et al. [65] studied UV degradation in low-density polyethylene (LDPE) films through heterostructures based on TiO_2, LDPE and GA (LDPE/GA-TiO_2). Montes-Zavala et al. [66] and González-Rodríguez et al. [67] studied the effects of the functionalization of titanium dioxide particles with a GA layer on the rheological properties. Bakre et al. [68] reported that TiO_2 modified with GA (TiO_2-GA) exhibited better photocatalytic activity under UV radiation than Degussa TiO_2 P-25 in the degradation of methylene blue. Nonetheless, as the authors are aware, the sensitization of TiO_2 to visible light by functionalization with glutaric acid (TiO_2-GA) and its photocatalytic performance under visible light radiation have not yet been investigated.

3
Proposal

3.1
General objective

Develop visible light-sensitive structures based on TiO_2 anatase nanoparticles anchored to complexing agents to increase the efficiency of the photodegradation of aqueous organic pollutants.

3.2
Specific objectives

1. To synthesize *via* sol-gel two nano-hybrids sensitive to visible light based on anatase conjugated with acetylacetone (TiO_2-ACAC) and glutaric acid (TiO_2-GA) in order to evaluate their photocatalytic efficiencies for the degradation of tetracycline.
2. To evaluate the influence of oxygen vacancies on the physicochemical properties and photocatalytic activity of the TiO_2-ACAC nano-hybrids, such as TiO_2-ACAC and TiO_2-GA.
3. To evaluate the efficiency of formation of reactive oxygen species by the charge transfer complexes (CTCs) formed between TiO_2 and complexing agents (ACAC and GA) through photocatalytic tests in aqueous media using suitable scavengers.

4

Extrinsic point defects in TiO_2-Acetylacetone charge transfer complex and their effects on optical and photochemical properties

4.1

Experimental methods

4.1.1

Synthesis of TiO_2-ACAC CTCs nanopowders

The synthesis of TiO_2-Acetylacetone Charge Transfer Complexes was carried out through the sol-gel route [48, 52], using the initial molar ratio of [ACAC]/[Ti] = 2.0. The synthesis process was carried out in five steps. In the first step, 30 mL of titanium (IV) isopropoxide $Ti(OiPr)_4$ (97%, Sigma Aldrich, San Luis, MO, USA) was slowly dropped under magnetic stirring into the alcolic solution of 20 mL of Acetylacetone (99%) with 100 mL of ethanol ($\geq$ 99.8%), provided by Sigma Aldrich, San Luis, MO, USA, whereupon a yellow solution was obtained. The yellow solution remained for 40 minutes under magnetic stirring at room temperature. Later, in the second stage of the process, 180 mL of the aqueous solution of HNO_3 (0.015M), where the HNO_3 was provided by Sigma Aldrich, San Luis, MO, USA, were added dropwise into the yellow solution to generate hydrolysis reaction. In the third stage, the solution was heated to 60°C and kept under magnetic stirring for 8 h to promote condensation reaction. Afterward, the yellow sol of TiO_2 was dried on Petri dishes at room temperature for 15 h, obtaining a gel TiO_2-ACAC RT. Next, in the fifth stage, the gel was dried at 100 °C for 15 h to obtain an orange xerogel of TiO_2 coated with acetylacetone, denoted as TiO_2-ACAC. Figure 4.1 shows the scheme of the synthesis process of the TiO_2-ACAC nanoparticles by the sol-gel route.

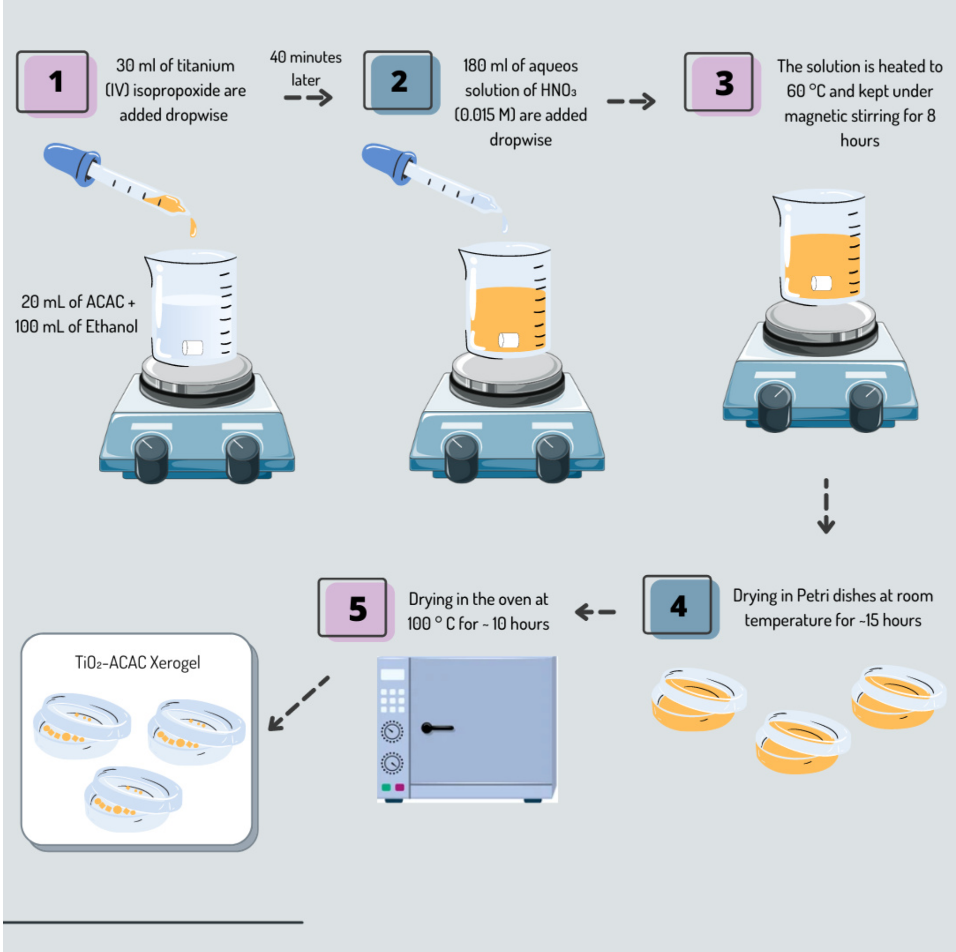

Figure 4.1: Schematic illustration of the synthesis process of TiO_2-ACAC nanoparticles through sol-gel route.

The TiO_2-ACAC xerogel was grounded in an agate mortar and calcined for 2 h, using a horizontal tubular furnace, at 270 °C under static air, pure argon and hydrogen atmospheres. Table 4.1 presents the samples nomenclature.

Table 4.1: TiO_2-ACAC CTC nanopowders nomenclature.

Samples	**Description**
TiO_2-ACAC 270	TiO_2-ACAC Calcined at 270 °C under static air
TiO_2-ACAC Ar 270	TiO_2-ACAC Calcined at 270 °C under argon atmosphere with a flow rate of 50 $mL \cdot min^{-1}$
TiO_2-ACAC H_2 270	TiO_2-ACAC calcined at 270 °C under hydrogen atmosphere with a flow rate of 50 $mL \cdot min^{-1}$

4.1.2

Characterization techniques

The phase composition of TiO_2-ACAC CTCs was characterized through X-ray powder diffraction (XRPD), using a Bruker D8 Advance diffractometer (Bruker, Karlshure, Germany) and operating with Cu Kα radiation in the

Bragg-Brentano configuration within the 2θ range between 20° and 80° with a step size of 0.02° per 1 second. In order to extract the information related to the phase composition and the unit-cell parameters of the CTCs, X-ray powder diffraction data were analyzed by the Rietveld method through Topas-Version 5 software (Bruker, Karlshure, Germany). Fundamental parameters approach was used for the definition of instrumental profile of the diffractometer, *i.e.*, a standard sample (LaB_6) was used for the adjustment of the fundamental parameters. Unit-cell and background parameters, together with scale factor, were only used for the refinement of experimental patterns. Structural parameters were not considered for refinement.

The diffuse reflectance spectroscopy (DRS) was carried out using a Perkin-Elmer Lambda 650 UV/Vis spectrophotometer (Perkin-Elmer, Waltham, MA, USA), in a wavelength range from 800 nm to 250 nm in steps of 1 nm, using α-Al_2O_3 as a reference. The band-gap energy of the CTCs was computed from diffuse reflectance spectra using the Kubelka-Munk function for indirect semiconductors, described by the following equation:

$$[F(R)hv]^{1/2} = C\,(hv - E_g)\,; \;\; F(R) = \frac{(1-\%R)^2}{2\%R}, \tag{4-1}$$

where the $F(R)$ function represents the absorption coefficient, E_g corresponds to the band-gap energy and %R is the reflectivity of the materials.

The thermogravimetric (TGA) analysis were performed using a Perkin-Elmer Simultaneous Thermal Analyzer, STA-6000 (Perkin-Elmer, Waltham, MA, USA), within a temperature range between 30 °C and 800 °C with a heating rate of 10 $°C \cdot min^{-1}$, under static air flow of 20 $mL \cdot min^{-1}$.

The photoluminescence emission spectroscopy (PL) was carried out at room temperature using a Spectroflurometer Photon Technology International, model Quanta Master 40, under Xenon lamp excitation at 350 nm.

The valence states of titanium on the surface of TiO_2-ACAC CTCs were identified by X-ray photoelectron spectroscopy (XPS) using an Alpha 110 hemispherical analyzer (VG Thermo Scientific, Waltham, MA, USA) and the Al K_α line (1486.6 eV) radiation. For the analysis, the spectra of the photoelectrons associated with the electrons of Ti 2p energy levels were measured, using the C 1s line with the energy of 284.7 eV for the energy correction. The intensities of the spectra were calculated through the integrated areas of the different peaks using the CasaXPS software.

Bulk extrinsic oxygen vacancies of TiO_2-ACAC CTCs were determined by electron paramagnetic resonance (EPR) at 300 K using a commercial MiniScope MS400 spectrometer (Magnettech, Germany) operating at 9.43 GHz with a 100 kHz field modulation and an amplitude of 0.2 mT. The magnetic field is generated by a Varian (9") electromagnet coupled to a Heinzinger (Germany) current source. The temperature (300 K) was guaranteed by a He flux cryosystem, ESR 900 (Oxford, England). For Landé g-factor calibration, a standard sample of 2,2-Diphenyl-1-picrylhydrazyl (DPPH) with g = 2.0037 was used. The experimental parameters used in the measurements were 10 mW of microwave power, field centered at 337 mT with application interval of 10 mT, scan time of 60 s and 4096 integration points.

The ROS involved in the photocatalytic mechanism of TiO_2-ACAC CTCs were analyzed through EPR measurements coupled to the spin trapping method and EPR detection with probe reagents. ROS generated by TiO_2-ACAC CTCs under visible light radiation were identified using 0.2 M of DMPO (5,5-dimethyl-1-pyrroline n-oxide, CAS 3317-61-1, 96%, Oakwood, EUA), as spin trap, and 10 mg of photocatalyst, both in aqueous medium and in acetonitrile (ACN) solution. The formation of DMPO-OH* and DMPO* adducts in aqueous solution was detected by EPR simulation employing Easyspin@ routine in Matlab. For the DMPO-OH* adduct, the spin Hamiltonian parameters given by the electron spin S = 1/2 interacting with the nuclear spins of ^{14}N (I = 1) and ^{1}H (I = 1/2) with $a_N = a_H = 1.49$ mT were used [69]; while for the DMPO* adduct, the parameters given by S = 1/2 with $a_N = 1.46$ mT were employed. Additionally, the formation of DMPO-OOH* and DMPO* adducts in ACN solution was detected using the spin Hamiltonian parameters for DMPO-OOH* adduct, given by S = 1/2 interacting with the nuclear spin of ^{14}N and ^{1}H with $a_N = 1.30$ mT and $a_{H(\beta)} = 1.00$ mT; and S = 1/2 interacting with I = 1 of ^{14}N with $a_N = 1.36$ mT for DMPO*. The quantification of superoxide radical production by TiO_2-ACAC CTCs was carried out by double integration of the EPR spectra of the aqueous solution containing 0.1 M Hydroxy-TEMP (2,2,6,6-tetramethylpiperidinol, CAS 768-66-1, 99%, Sigma-Aldrich, EUA), as probe reagents, and 10 mg of photocatalyst.

4.1.3

Measurement of the photocatalytic performance for the TC photodegradation and the efficiency of reactive oxygen species (ROS) production

The photocatalytic performance of TiO_2-ACAC CTCs was measured using the same equipment and following a similar procedure to that reported by Almeida et al. [70]. The measurements were carried out using 5 mg·L^{-1} of Tetracycline, as a testing pollutant, and 50 mg·L^{-1} of the photocatalysts (TiO_2-ACAC CTCs). Figure 4.2 shows the setup of the photocatalytic system used in this study.

The photocatalysts were activated through photons supplied by a DULUX D/E 26 W residential fluorescent lamp with visible light emission (wavelength range from 400 nm to 700 nm) and irradiance of 0.23 W $\cdot$cm^{-2} [70]. The lamp was placed inside a transparent quartz sleeve with a cylindrical geometry (internal diameter 3.2 cm, thickness 0.15 cm and length 11 cm).

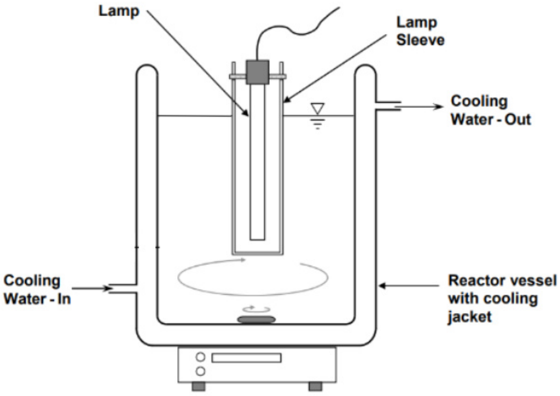

Figure 4.2: Photocatalysis system set-up, image adapted from [9].

To keep the temperature fixed at room temperature during the testing process, cold water was circulated around the outer wall of the cylindrical reactor cavity. The total time of the experimental process was set to 420 min, including adsorption-desorption equilibrium and photocatalysis; during this time, the solution contained in the reactor was kept under continuous magnetic stirring.

The experimental process was divided into two stages. In the first stage, the pollutant and photocatalyst in an aqueous solution remained in the dark for 1 h to reach the adsorption–desorption equilibrium. After that, the lamp was switched on and 5 mL aliquots were withdrawn from the reactor at intervals of 1 h for 6 hours. The aliquot was filtered using a Merck Millipore filter of 0.45 μm and deposited in a quartz cuvette to be analyzed through an Agilent 8453 UV-Vis spectrophotometer. The percentage of the TC photodegradation was determined by the decrease in the absorption peak of TC at the wavelength of 358 nm. To ensure the reliability of the results, photodegradation measurements were performed in duplicate. Therefore, the photodegradation results presented in this study correspond to the mean value with its respective error.

On the other hand, to determine the efficiency of ROS formation in the TiO_2-ACAC CTCs, the concentration of photocatalyst was increased from 50 mg $\cdot$ L^{-1} to 100 mg $\cdot$ L^{-1} to increase photoactive sites. The scavenger molecule benzoquinone (BQ) (5.4 mg $\cdot$ L^{-1}) was added, before starting the photocatalytic test, to the initial aqueous solution of the pollutant. This molecule inhibits the participation of $^{\bullet}O_2^-$ radicals in the pollutant degradation process. The $^{\bullet}$OH radicals efficiency in the TiO_2-ACAC CTCs for the photodegradation process was evaluated through the addition of the isopropanol (IPA) scavenger ($6.0\ mg \cdot L^{-1}$) to the initial aqueous solution of the pollutant. In this case, the IPA molecule restricts the participation of $^{\bullet}$OH radical in the pollutant degradation process.

4.2
Results

4.2.1
XRPD of TiO_2-ACAC CTCs

The crystal phase analysis of the TiO_2-ACAC 270, TiO_2-ACAC Ar 270 and TiO_2-ACAC H_2 270 nanopowders were carried out by XRPD. The XRPD patterns of TiO_2-ACAC CTCs, presented in the Figure 4.3, exhibited diffraction peaks corresponding to the (101), (004), (200), (211), (204), (220), and (215) crystallographic planes of anatase phase (PDF-2: 21-1272).

The calcination process under reducing atmospheres led to slight displacement towards higher angles in the diffraction peaks of TiO_2-ACAC CTCs (inset of Figure 4.3a). This slight shift in the diffractions peaks is directly related to the decrease of the lattice parameters due to crystal structure relaxation generated by the increasing of the extrinsic oxygen vacancies concentration in the TiO_2-ACAC structure (*vide infra* §4.2.4). This shift in the diffraction peaks was also observed for defective TiO_2 with oxygen vacancies by Pan et al. [38] and Chen et al. [39]. The decrease in the unit-cell volume of the CTCs calcined under reducing atmospheres, compared to the cell volume of the CTC calcined under static air, is presented in Figure 4.3b.

The lattice parameters of the TiO_2-ACAC CTCs, as determined by the Rietveld refinement (see the XRPD patterns fitting in Figure S1, Supplementary Information), are shown in Table S1 (see the Supplementary Information).

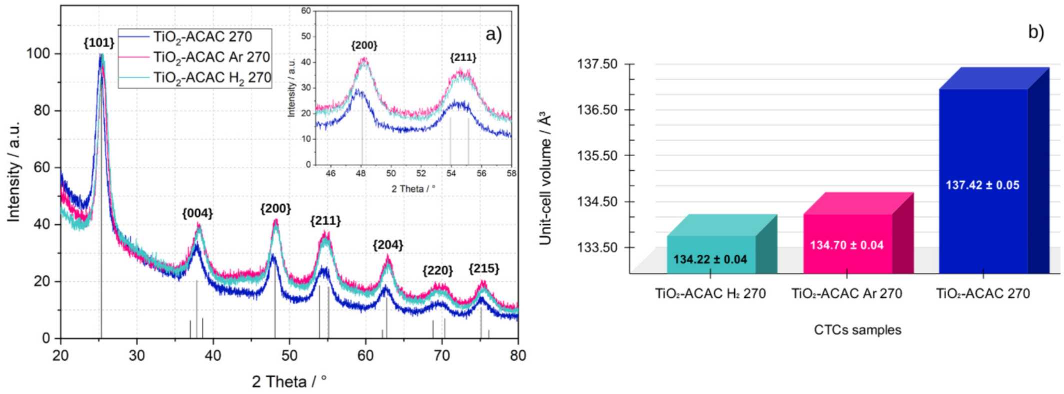

Figure 4.3: (**a**) XRPD patterns of TiO_2-ACAC 270, TiO_2-ACAC Ar 270 and TiO_2-ACAC H_2 270, (**b**) Comparison between the unit-cell volumes of the CTCs calcined at 270 °C.

4.2.2

TGA of TiO_2-ACAC CTCs

The quantity of the acetylacetone in the TiO_2-ACAC CTCs was determined through the overall mass loss due to acetylacetone fragmentation, which occurs in the temperature range from 150 °C to $\sim$ 490 °C (Figure 4.4) [43, 71]. As expected, the calcination process led to a decrease in the organic molecule content in the CTCs, from 13.1% for xerogel to 3.5% for TiO_2-ACAC 270, due to the partial volatilization of ACAC during the calcination at 270° [43, 71]. However, a higher percentage of acetylacetone was detected for CTCs calcined under reducing atmospheres (7.4% for hydrogen atmosphere and 5.5% for argon atmosphere) compared to CTC calcined under static air (3.5%). This result is in accordance with the observation by Almeida et al. [70], who reported that the acetylacetone fragmentation corresponds to an oxidative process. Therefore, as observed in Figure 4.4, calcination under reducing atmospheres was expected to lead to the presence of a higher percentage of acetylacetone in the TiO_2-ACAC CTC. Nevertheless, a high amount of ACAC bounded to the TiO_2 surface can be undesirable, since ACAC could occupy the active sites at the photocatalyst surface and might negatively impact on the photocatalytic performance of the TiO_2-ACAC CTCs.

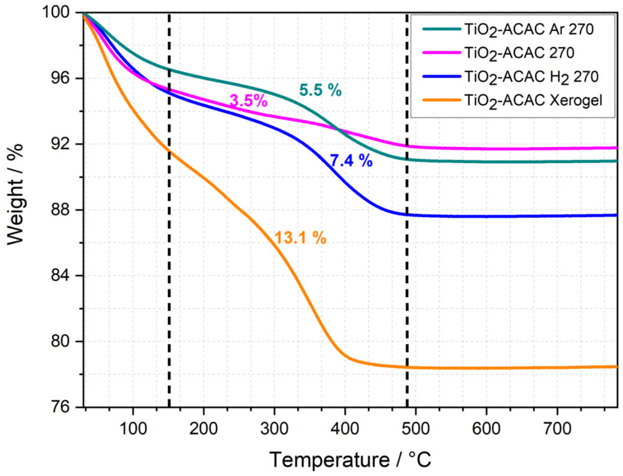

Figure 4.4: TGA curves of all TiO_2-ACAC CTCs. The vertical dashed lines denote the temperature range corresponding to the overall mass loss of ACAC onto TiO_2 surface. The percentages represent the total mass loss of ACAC in the temperature range from 150 °C to 490 °C.

4.2.3
Optical properties of TiO_2-ACAC CTCs

Figure 4.5 represents the DRS spectra of TiO_2-ACAC xerogel, TiO_2-ACAC 270, TiO_2-ACAC Ar 270 and TiO_2-ACAC H_2 270, where the sensitization to the visible light of the TiO_2 was evidenced due to two processes. The first process corresponds to ligand-to-metal charge transfer (LMCT) mechanism formed between ACAC and TiO_2, observed for TiO_2-ACAC xerogel [72, 44, 52], while the second process corresponds to extrinsic oxygen vacancies, formed through the calcination process, in the TiO_2-ACAC CTCs.

As a result of the ligand-to-metal charge transfer (LMCT) mechanism and the coupling between the LMCT mechanism and the extrinsic oxygen vacancies, three features were identified in the DRS spectra (Figure 4.5). The first feature (Figure 4.5a) corresponds to xerogel absorption, presented a long absorption tail in the visible light spectrum compared to TiO_2 [39], with an apparent band-gap energy of 2.40 eV (Figure 4.5b), in accord to Habran et al. [52], Almeida et al. [43] and Sannino et al. [44]. The sample showed orange color.

A second feature, showed by TiO_2-ACAC 270, exhibited a higher visible light absorption compared to xerogel with a slight decrease in light absorption starting at 600 nm and an apparent band-gap energy of 1.14 eV (Figure 4.5b), showing a dark brown color, similar to that reported by Almeida et al. [43] for TiO_2-ACAC 300 material. The dark brown color presented by the TiO_2-ACAC 270 can be attributed to the extrinsic oxygen vacancies created through volatilization of the acetylacetone molecules bounded to

TiO_2 surface, during the calcination process under static air, as proposed by Almeida et al. [70]. Wang et al. [73], Pan et al. [38] and Sinhamahapatra et al. [74] reported that extrinsic oxygen vacancies create intermediate energy levels within semiconductor band-gap, resulting in increased visible light sensitization in TiO_2-ACAC 270.

On the other hand, the CTCs calcined under reducing atmospheres (TiO_2-ACAC Ar 270 and TiO_2-ACAC H_2 270 materials) were classified within the third regime of visible light absorption. These complexes evidenced a darker coloration than the previously described sample (TiO_2-ACAC 270), showing almost complete visible light absorption, with an apparent band-gap energy close to 0.5 eV (0.44 eV for TiO_2-ACAC H_2 270 and 0.46 eV for TiO_2-ACAC Ar 270, see Figure 4.5b). This significant increase in visible light absorption resulted from the interplay between the increase of extrinsic oxygen vacancies concentration, through the calcination under reducing atmospheres, and the LMCT mechanism.

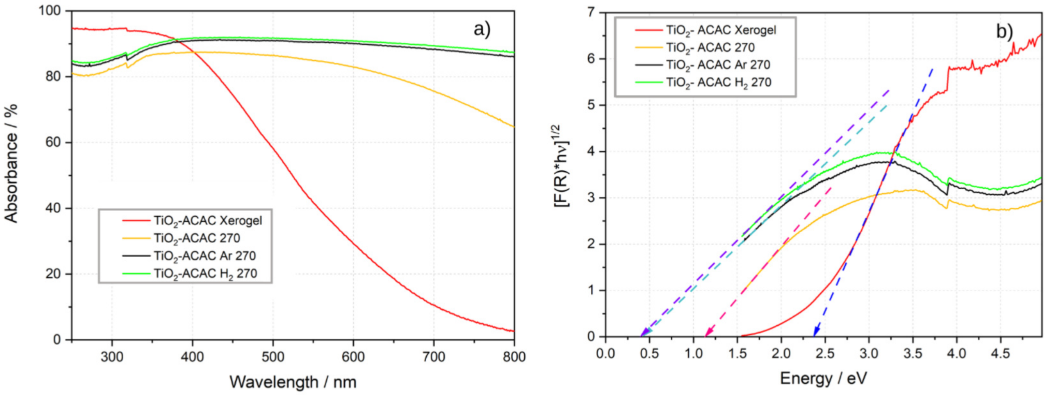

Figure 4.5: (**a**) DRS curves and (**b**) Kubelka-Munk plots of the TiO_2-ACAC xerogel, TiO_2-ACAC 270, TiO_2-ACAC Ar 270, TiO_2-ACAC H_2 270.

Photoluminescence (PL) emission spectra of the TiO_2-ACAC CTCs were acquired to evaluate the LMCT mechanism between ACAC and TiO_2 and the creation of the optical centers due to extrinsic oxygen vacancies. Emission spectra, in the energy range of 1.82 - 3.0 eV, with excitation at 3.57 eV ($\lambda_{exc} = 350$ nm), were deconvoluted keeping the same parameters of the known bands. Figure 4.6 illustrates the deconvolution of PL emission spectra of TiO_2-ACAC xerogel (a), TiO_2-ACAC 270 (b), TiO_2-ACAC Ar 270 (c) and TiO_2-ACAC H_2 270 (d).

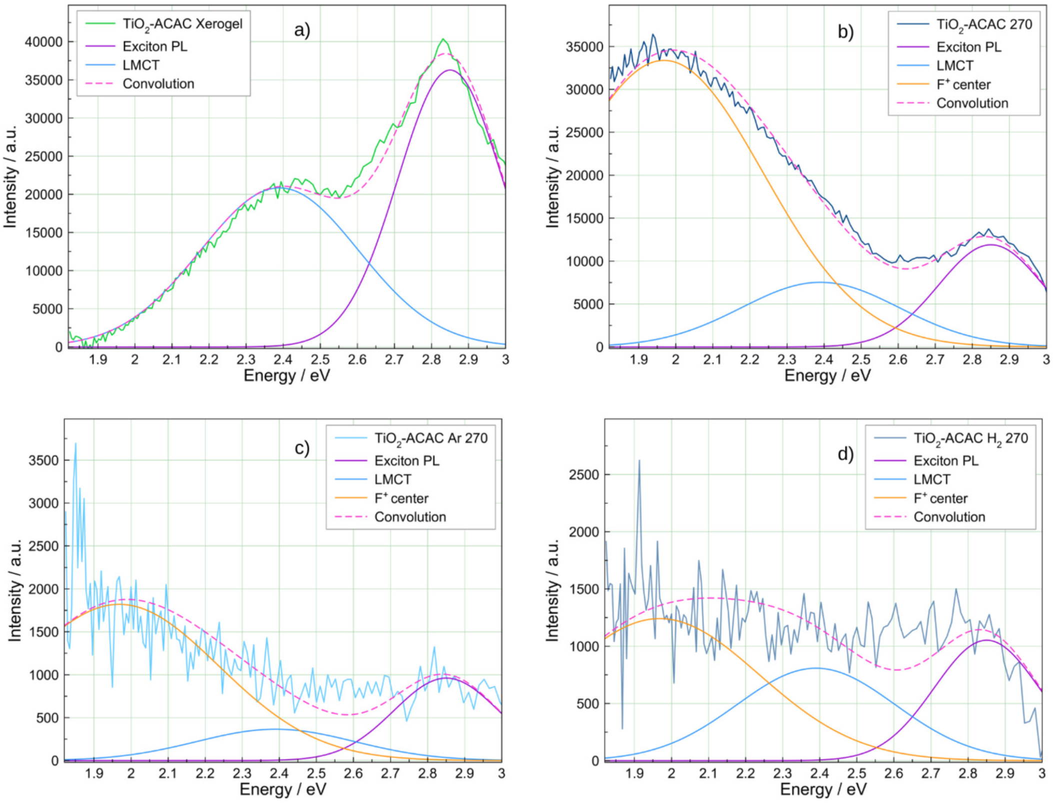

Figure 4.6: Photoluminescence emission spectra of (**a**) TiO_2-ACAC xerogel, (**b**) TiO_2-ACAC 270, (**c**) TiO_2-ACAC Ar 270 and (**d**) TiO_2-ACAC H_2 270.

In all PL emission spectra, two bands were observed with maxima at 2.85 eV and 2.40 eV, and HWHM of 0.17 and 0.25 eV, respectively. The band centered at 2.85 eV was attributed to the exciton photoluminescence [75, 76, 77] and the other band (at 2.40 eV) to the emission photons due to decay of free electrons from the anatase conduction band (CB) to the highest occupied molecular orbital (HOMO) of ACAC, through the LMCT mechanism [43, 52, 72, 44].

In the photoluminescence emission spectra of the calcined CTCs (TiO_2-ACAC 270 (b), TiO_2-ACAC Ar 270 (c) and TiO_2-ACAC H_2 270 (d), a third emission band was observed with a maximum at 1.97 eV and a HWHM of 0.32 eV. Serpone [58] and Chen et al. [59] attributed the band situated around 1.7 – 2.1 eV region (729 – 590 nm) due to transition from the excited state of the F^+ center (denoted F^{+*} center) to its corresponding ground state. This means that the third band of PL emission spectra of calcined TiO_2-ACAC CTCs can be attributed to deep trap states originated from oxygen vacancy associated with F^+ center, *i.e.*, single electron trapped in oxygen vacancies (SETOV) [77] (Equation 4-3).

$$\mathrm{V_O + 2e^- = V_O^x \equiv F} \tag{4-2}$$

$$\mathrm{SETOV} = \mathrm{V_O} + 1\mathrm{e}^- = \mathrm{V_O^{\bullet}} \equiv \mathrm{F}^+ \qquad (4\text{-}3)$$

$$\mathrm{V_O} + 0\mathrm{e}^- = \mathrm{V_O^{\bullet\bullet}} \equiv \mathrm{F}^{++} \qquad (4\text{-}4)$$

Additionally, a significant decrease in the intensity of the photoluminescence emission spectra was observed for the CTCs calcined under reducing atmospheres, feature that could be attributed to the increased concentration of extrinsic oxygen vacancies (*vide infra §4.2.4*), that can lead to different processes such as: (1) Auger recombination [78, 79], (2) shallow electron trapping [39, 80], and (3) radiative recombination *via* the trap-assisted recombination mechanism [81, 82], which do not contribute to the intensities in the range between 1.82 and 3.0 eV.

4.2.4
Electron paramagnetic resonance and X-ray photoelectron spectroscopy of TiO_2-ACAC CTCs

The presence of the oxygen vacancies in the calcined CTCs was also evidenced through electron paramagnetic resonance spectra at room temperature. Figure 4.7 shows the EPR signals of the TiO_2-ACAC CTCs, where the first derivative of the absorption spectra of all CTCs in the resonance condition showed the same behaviour, with a Landé g-factor = 2.00, characteristic of the SETOV (attributed to bulk extrinsic oxygen vacancy $\mathrm{V_O^{\bullet}}$) in the anatase [83]. Trivalent titanium ions (g = 1.96 – 1.99) [84] were not evidenced in the EPR signals of the CTCs. Therefore, charge compensation in the structure of TiO_2-ACAC CTCs would occur predominantly through an electronic compensation process, where the removal of an oxygen atom in TiO_2 implies the presence of zero, one or two electrons in the oxygen vacancy site, leading to the formation of color centers F^{++}, F^+ and F (Equations 4-2 - 4-4 in section §4.2.3) [58, 55], respectively.

In addition, the SETOV concentrations of the CTCs were determined by double integrations of the EPR signals and their comparison with a standard $CuSO_4$ sample. The SETOV concentration of TiO_2-ACAC H_2 270 (1.30×10^{16} cm^{-3}) is approximately 1.3 times of SETOV concentration of TiO_2-ACAC Ar 270 (1.06×10^{16} cm^{-3}) and about five times higher than in TiO_2-ACAC 270 (2.80×10^{15} cm^{-3}), evidencing an increase in the concentrations of bulk extrinsic oxygen vacancies for CTCs calcined under reducing atmospheres, in agreement with the photoluminescence, DRS and XRPD results.

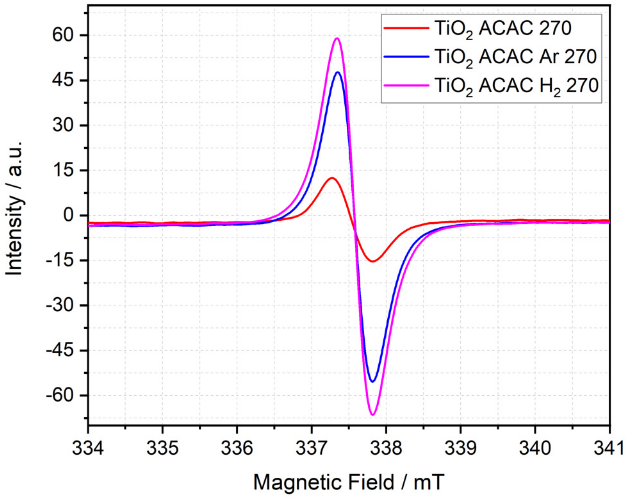

Figure 4.7: Electron paramagnetic resonance spectra of TiO_2-ACAC 270, TiO_2-ACAC Ar 270 and TiO_2-ACAC H_2 270.

X-ray photoelectron spectra of the TiO_2-ACAC CTCs were evaluated to determinate the valence states of the titanium on the CTCs surface. Figure 4.8 represents the Ti 2p spectra of TiO_2-ACAC 270 (a), TiO_2-ACAC Ar 270 (b), TiO_2-ACAC H_2 270 (c) and the comparison between Ti 2p spectra of CTCs (d). All CTCs exhibited a distance between the binding energies (ΔBE) of the Ti $2p_{1/2}$ and Ti $2p_{3/2}$ XPS peaks ($\Delta BE = BE(Ti\ 2p_{1/2}) - BE(Ti\ 2p_{3/2})$) of 5.7 eV, a characteristic of Ti^{4+}-O bonds in TiO_2 [85].

In addition, a shift to higher energies for the Ti 2p binding energies (BE) was observed for the CTCs calcined under reducing atmospheres compared to the CTC calcined under static air (Figure 4.8d), evidencing a BE positive displacement of 1.0 eV for TiO_2-ACAC H_2 270 in comparison to TiO_2-ACAC 270 and a BE positive shift of 0.88 eV in comparison to TiO_2-ACAC Ar 270. This positive displacement in the Ti 2p binding energy was attributed to the lattice distortions generated by the increase of surface/bulk extrinsic oxygen vacancies concentration in the CTCs [38, 40], previously reported through the XRPD results (Figure 4.3b), where the removal of an oxygen atom generates a repulsion between the second nearest neighbors, *i.e.*, causing an outward relaxation between the nearest titanium atoms and as a consequence, a reduction of Ti-O bond lengths and an increase in the Ti 2p binding energy [60, 38, 39]. Additionally, Ti^{3+} signal was not identified in the XPS spectra of Ti 2p, since a shift to lower binding energy was not evidenced and no additional peaks were observed at lower binding energies [39]. This is in agreement with the EPR results (Figure 4.7), confirming that the charge compensation process in the TiO_2-ACAC CTCs occurs, predominantly, through electronic compensation.

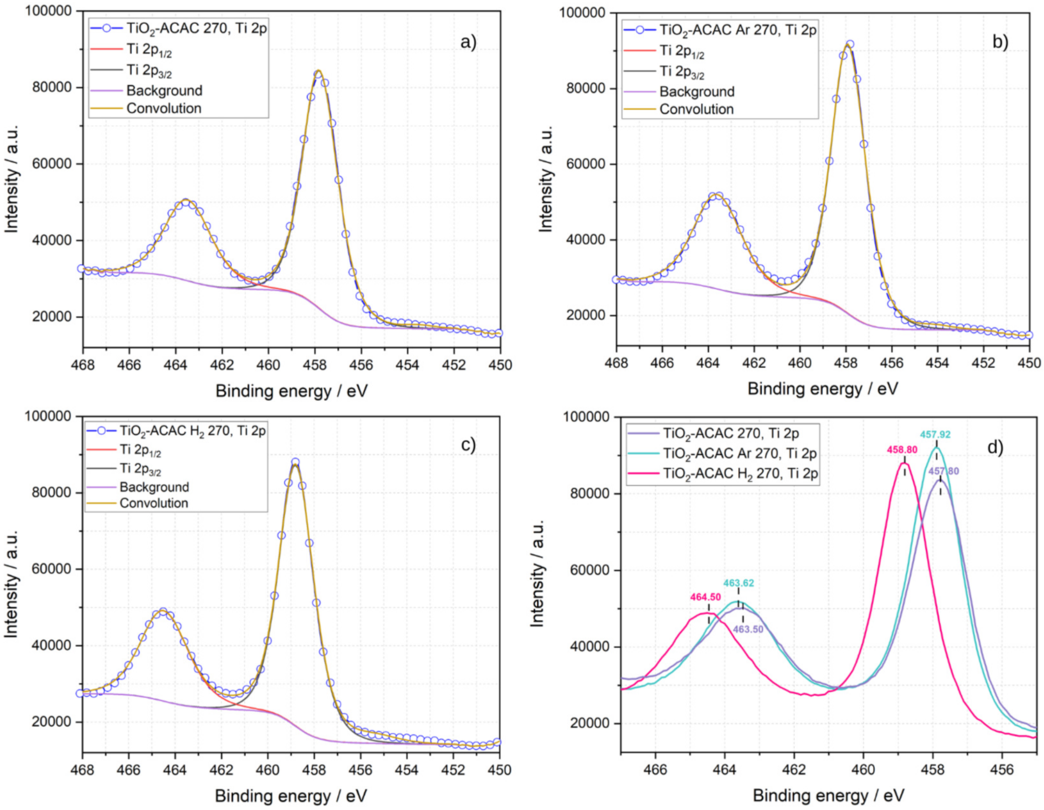

Figure 4.8: X-ray photoelectron spectra of Ti 2p for (**a**) TiO_2-ACAC 270, (**b**) TiO_2-ACAC Ar 270, (**c**) TiO_2-ACAC H_2 270 and (**d**) comparison between Ti 2p binding energy of the CTCs calcined at 270 °C.

4.2.5
Photocatalytic performance of TiO_2-ACAC CTCs

The photocatalytic activity of the TiO_2-ACAC CTCs was evaluated by monitoring the TC degradation in an aqueous medium using a very low photocatalyst concentration (50 mg·L^{-1}) under low-power visible light (26 W). Figure 4.9a shows the tetracycline evolution during its photocatalytic degradation in the presence of the TiO_2-ACAC CTCs as photocatalysts. Adsorption-desorption equilibrium (1h in dark) and TC photocatalytic degradation curves using TiO_2-ACAC CTCs as photocatalysts are shown in Figure S2 (see the Supplementary Information).

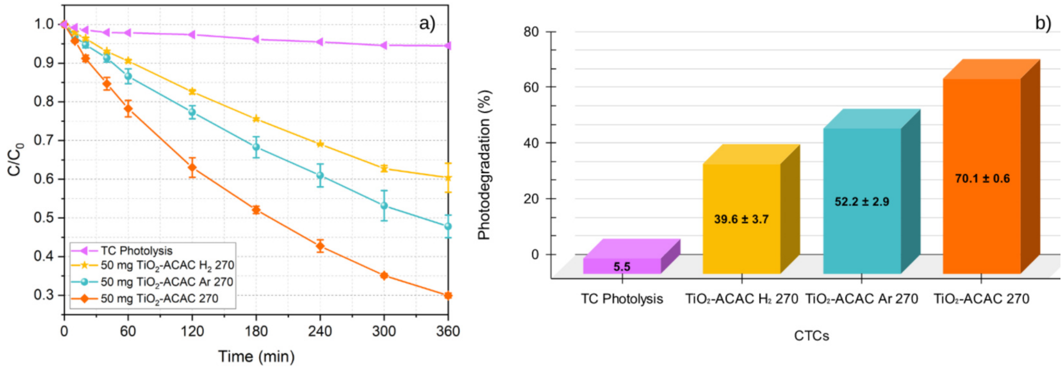

Figure 4.9: (**a**) Tetracycline evolution during its photocatalytic degradation using TiO_2-ACAC CTCs as photocatalysts and (**b**) Tetracycline photodegradation using TiO_2-ACAC CTCs after 6 h under visible light radiation.

As shown in Figure 4.9, photolysis showed insignificant TC degradation. On the other hand, all TiO_2-ACAC CTCs caused photocatalytic abatement of tetracycline. However, a variation in the photocatalytic performance of the different CTCs, studied in this work was evidenced. The CTC calcined under static air, TiO_2-ACAC 270, presented the highest photocatalytic degradation after 6 h (70.1% ± 0.6%). Additionally, it was observed that among the CTCs calcined under reducing atmospheres, TiO_2-ACAC Ar 270 presented a better photocatalytic performance than the TiO_2-ACAC H_2 270. After 6 h of visible light radiation, the TiO_2-ACAC Ar 270 CTC photodegraded 52.2% ± 2.9% of the TC, while the TiO_2-ACAC H_2 270 CTC exhibited a photocatalytic abatement of 39.6% ± 3.7%. This difference in the photocatalytic performance of TiO_2-ACAC CTCs for tetracycline abatement could be attributed to two factors. The first one is the increase in the concentration of bulk extrinsic oxygen vacancies in TiO_2-ACAC Ar 270 and TiO_2-ACAC H_2 270 samples, determined through EPR, which would be acting as recombination centers. In fact, Li et al. [40] already reported photocatalytic inactivity for CO_2 reduction using TiO_2-BO (TiO_2 coupled to bulk extrinsic oxygen vacancies), as photocatalyst, after 6 h exposure to 250 W high-pressure Hg lamp (visible light radiation). Additionally, Huang et al. [41] observed a decrease in the photocatalytic performance of Black-TiO_2 for NO removal with increasing concentration of oxygen vacancies. The second factor could be the higher amount of ACAC bound to the surface of the TiO_2-ACAC Ar 270 and TiO_2-ACAC H_2 270 CTCs (Figure 4.4), which could be occupying the active sites on the CTCs surface, resulting in a reduced photocatalytic abatement.

In order to evaluate the ROS production by TiO_2-ACAC CTCs, additional photocatalytic tests were carried out in aqueous medium using benzoquinone and isopropanol as superoxide ($^{\bullet}O_2^-$) and hydroxyl ($^{\bullet}OH$) scavengers, respectively, and a higher photocatalyst concentration (100 mg·L^{-1}) than the used in the previously performed tests.

Figure 4.10 shows the TC photodegradation in the presence of TiO_2-ACAC 270, as photocatalyst, with and without the addition of scavengers. As observed in Figure 4.10b, without the addition of scavengers, TiO_2-ACAC 270 photodegraded 78.4% ± 1.3% of TC after 6 h.

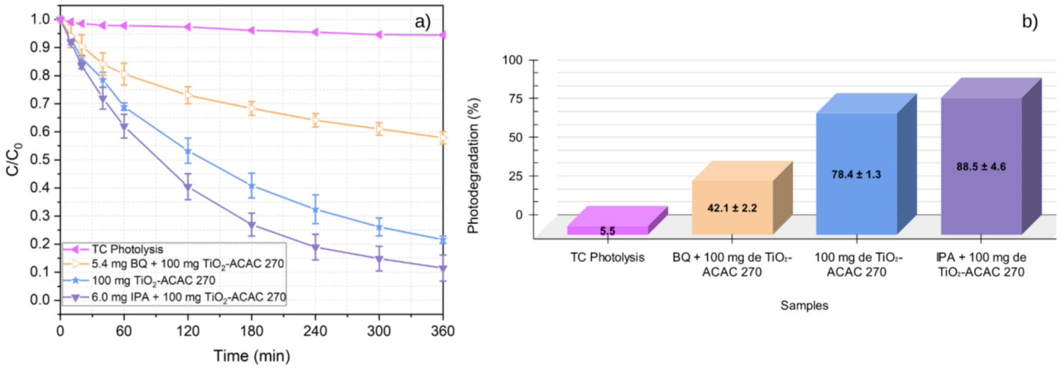

Figure 4.10: (**a**) Tetracycline evolution during its photocatalytic degradation using TiO_2-ACAC 270 as photocatalysts with and without addition of scavengers (BQ and IPA) and (**b**) Tetracycline photodegradation using TiO_2-ACAC 270 with and without addition of BQ and IPA after 6 h under visible light radiation.

The addition of the hydroxyl radical scavengers (IPA) did not reduce the photocatalytic performance of the TiO_2-ACAC 270 in the TC photodegradation (Figure 4.10), and even exhibited a 10% higher photocatalytic abatement (88.5% ± 4.6%) compared to that measured without the addition of quenchers (78.4% ± 1.3%). This result could be firstly attributed to the low efficiency in the hydroxyl radical production and also, to the reaction between hydroxyl scavengers and electronic holes (h^+), coming from the HOMO of ACAC, [86, 3], as subsequently reported in the spin trapping analysis (Section §4.2.6). On the other hand, it was observed that the addition of benzoquinone, as a superoxide radical scavenger, to aqueous solution, caused a decrease of the TC photodegradation, exhibiting a photocatalytic abatement of 42.1% ± 2.2% after 6 hours (Figure 4.10), indicating that the superoxide radical plays the main role in the TC photocatalytic degradation by TiO_2-ACAC 270 CTC. In addition, this reduced but considerable photocatalytic degradation obtained by using BQ as scavenger, could be an indication of the possible participation of electronic holes in the TC degradation [87] and/or formation of the hydroxyl radical by the TiO_2-ACAC 270 CTC (*vide infra* in the Section §4.2.6).

The evolution of the TC photocatalytic degradation in the presence of the TiO_2-ACAC Ar 270 as photocatalyst with and without addition of scavengers is shown in Figure 4.11a. As displayed in the Figure 4.11b, the use of 100 mg·L^{-1} TiO_2-ACAC Ar 270 without addition of scavengers led to an TC photodegradation of 66.5% ± 0.9%.

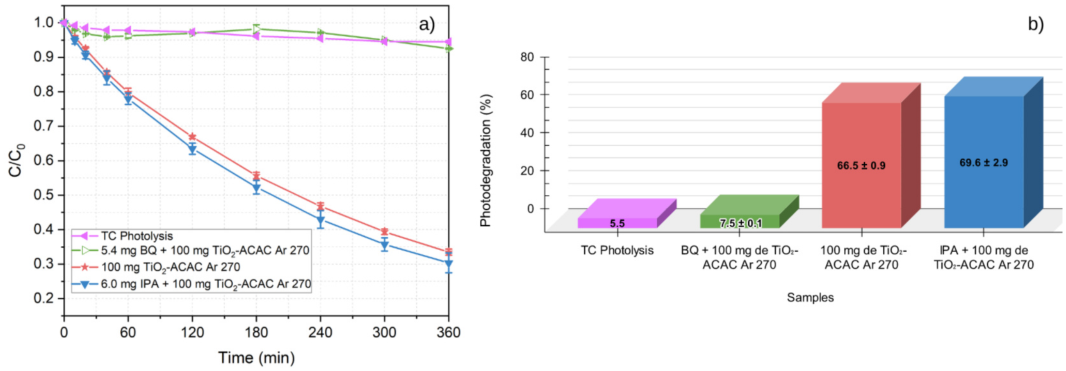

Figure 4.11: (**a**) Tetracycline evolution during its photocatalytic degradation using TiO_2-ACAC Ar 270 as photocatalysts with and without addition of scavengers (BQ and IPA) and (**b**) Tetracycline photodegradation using TiO_2-ACAC Ar 270 with and without addition of BQ and IPA after 6 h under visible light radiation.

The addition of the superoxide scavenger (BQ) had a significant impact on the tetracycline photodegradation, reducing photocatalytic degradation to only 7.5% ± 0.1% after 6 hours (Figure 4.11), indicating that the superoxide radical ($^{\bullet}O_2^-$) plays a dominant role in the photocatalytic performance of the TiO_2-ACAC Ar 270 in the TC photodegradation. On the other hand, the addition of the hydroxyl radical scavengers (IPA) did not significantly change the photocatalytic performance of the TiO_2-ACAC Ar 270 for the TC photodegradation. This result suggested that the TiO_2-ACAC Ar 270 is not efficient for the production of hydroxyl radicals ($^{\bullet}OH$) under visible light radiation.

TC photodegradation in the presence of TiO_2-ACAC H_2 270 as photocatalyst with and without addition of scavengers is shown in Figure 4.12. The use of 100 mg·L^{-1} of TiO_2-ACAC H_2 270 without addition of scavengers led to 65.1% ± 2.0% abatement of TC, after 6 h.

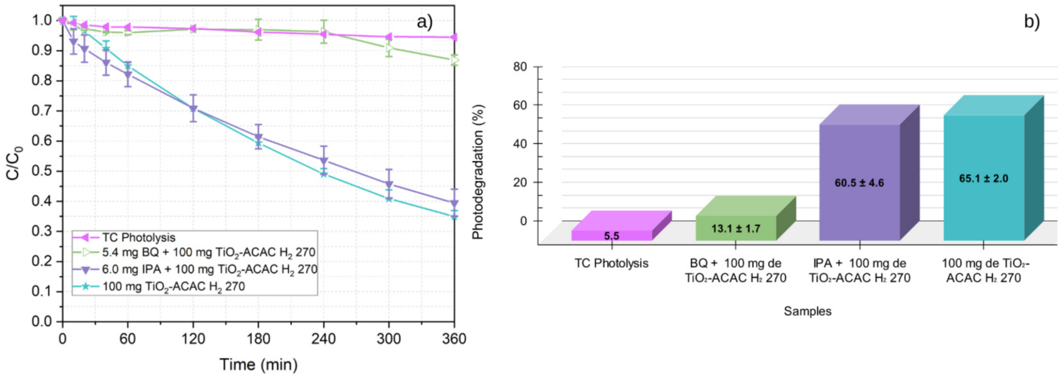

Figure 4.12: (**a**) Tetracycline evolution during its photocatalytic degradation using TiO_2-ACAC H_2 270 as photocatalysts with and without addition of scavengers (BQ and IPA) and (**b**) Tetracycline photodegradation using TiO_2-ACAC H_2 270 with and without addition of BQ and IPA after 6 h under visible light radiation.

The addition of the hydroxyl radical scavenger (IPA) led to a slight reduction in TC photodegradation. However, this decrease is within the error of the measurements (Figure 4.12b), evidencing the low efficiency of TiO_2-ACAC H_2 270 CTC for the formation of hydroxyl radical. On the other hand, the addition of the superoxide radical scavengers (BQ) caused a significant reduction in the photocatalytic performance of the TiO_2-ACAC H_2 270 in the TC photodegradation (Figure 4.10), exhibiting a photocatalytic abatement of 13.1% ± 1.7% after 6 hours. This result could be an indicative of two phenomena: the first is the high efficiency of TiO_2-ACAC H_2 270 to produce the superoxide radical and the second is the important role that the superoxide radical plays in the TC photodegradation.

4.2.6
Spin trapping of TiO_2-ACAC CTCs

In order to further investigate the photocatalytic mechanism involved in the TC photodegradation and to correlate it with the results of ROS formation study, obtained from TC photodegradation with scavengers (Section §5.2.6), EPR measurements using the spin trapping method were performed (Figure 4.13). The spin trap 5,5-dimethyl-1-pyrroline n-oxide (DMPO) was used to identify reactive oxygen species (ROS) generated by TiO_2-ACAC CTCs under visible light radiation (white LEDs with 16 mW $\cdot cm^{-2}$). The identification of the adducts, associated to ROS generated by TiO_2-ACAC CTCs, was carried out through the simulations of the EPR spectra using the Easyspin$^{@}$ routine in Matlab (Figures 4.13c and 4.13d).

Figures 4.13a and 4.13b represent the time evolution of the EPR-spin trapping signal of TiO_2-ACAC 270 under visible light radiation, with a maximum excitation time of 15 minutes and different solvents (water and ACN). The calculated EPR spectra, Figure 4.13c, indicated that the experimental spectrum in water is composed of DMPO-OH* and DMPO* adducts. The sum of both spectra (Figure 4.13c) reproduced the experimental one (Figure 4.13c), suggesting that the hydroxyl radical might be produced by the TiO_2-ACAC 270 CTC. However, it was evidenced in Figure 4.10 that the addition of IPA, as hydroxyl radical scavenger, did not reduce the photocatalytic performance of the TiO_2-ACAC 270 in the TC photodegradation, suggesting that the TiO_2-ACAC 270 is not efficient for the production of hydroxyl radicals under visible light radiation. In addition, it is known that the formation of the DMPO-OH* adduct may also be a result of two other different processes: (1) decomposition of hydroperoxyl adduct (DMPO-OOH*), formed through the capture of the superoxide radical by DMPO (Equation 4-5); (2) *via* oxidation of DMPO (Equation 4-6), where the cationic radical $DMPO^+$, due to DMPO oxidation, transforms to DMPO-OH* adduct through the hydrolysis process [88].

$$\mathrm{DMPO} \ + \ {}^{\bullet}\mathrm{O}_2^- \ \rightarrow \ \mathrm{DMPO-OOH}^* \ \overset{\text{decompose}}{\rightarrow} \ \mathrm{DMPO-OH}^* \qquad (4\text{-}5)$$

$$\mathrm{DMPO} \ + \ \mathrm{h}^+ \rightarrow \mathrm{DMPO}^+ \ \overset{\mathrm{H_2O}}{\rightarrow} \ \mathrm{DMPO-OH}^* \ + \ \mathrm{H}^+ \qquad (4\text{-}6)$$

On the other hand, Figure 4.10b evidenced that the addition of BQ, as a superoxide radical scavenger, led to a significant reduction of the TC photocatalytic abatement by TiO_2-ACAC 270, showing a photocatalytic degradation of 42.1% ± 4.6% after 6 hours. Considering the reactions described by Equations 4 and 5, the inefficient production of hydroxyl radical by TiO_2-ACAC 270, previously discussed, and the scavenging of the superoxide radical due to the addition of BQ, the TC photocatalytic degradation of 42.1% ± 4.6% by TiO_2-ACAC 270 can be attributed to the TC degradation *via* electronic holes from HOMO, as proposed by Ren et al. [87]. In fact, the TC photocatalytic abatement increased with the addition of IPA (10% higher compared to the percentage measured without addition of scavengers, Figure 4.10b) might be attributed to the interaction between electronic holes, coming from the HOMO of ACAC, with hydroxyl scavengers [86, 3], which could cause an inhibition of the subsequent secondary reactions, involving the interaction between H^+ (formed through electronic holes, Equation 4-7) and the superoxide radical (Equations 4-8-4-9). As a consequence, the addition of isopropanol, as a scavenger, would limit the chemical reactions of the superoxide radical, allowing only interaction between ${}^{\bullet}O_2^-$ and tetracycline, which results in increased TC photocatalytic degradation.

$$2H_2O + 4h^+ \rightarrow O_2 + 4H^+ \tag{4-7}$$

$$^{\bullet}O_2^- + H^+ \rightarrow HO_2^{\bullet} \tag{4-8}$$

$$^{\bullet}O_2^- + e^- + 2H^+ \rightarrow H_2O_2 \tag{4-9}$$

In order to detect superoxide radical, the spin trapping method were carried out using ACN as a solvent. The ACN was used, because of its high solubility for molecular oxygen (much higher than in water) and aproticity. The time evolution of the EPR spectra is shown in Figure 4.13b, where the EPR spectra simulation (Figure 4.13d) evidenced the formation of the DMPO-OOH* and DMPO* adducts (Figure 4.13d). The DMPO-OOH* adduct is the result of capture of superoxide radicals by DMPO, which afterwards are protonated [89].

From Figure 4.13b it was observed that the intensity of the EPR spectra of DMPO-OOH* adducts in ACN, determined by integration of the EPR signal, is $\sim$ 7.5 times higher compared to that of DMPO-OH* adducts in water, indicating that superoxide radicals are the dominant radical species produced by the TiO_2-ACAC 270 photocatalyst under visible light radiation. This result is in accord with the high TC photocatalytic abatement by TiO_2-ACAC 270 when IPA is used as scavenger and with the reduction in the TC photodegradation when BQ is used as scavenger in the aqueous solution (Figure 4.10).

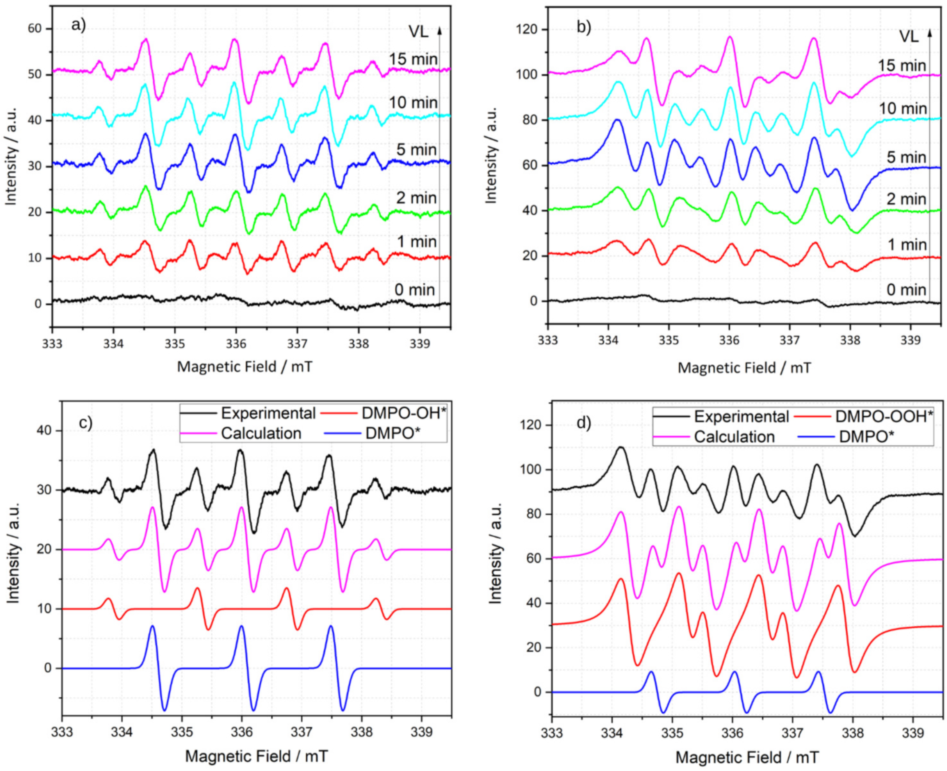

Figure 4.13: EPR spectra as a function of visible light (VL) radiation of (**a**) DMPO (0.2 M) spin trap in water and (**b**) DMPO (0.2 M) spin trap in acetonitrile (ACN) both containing in suspension 10 mg of TiO_2-ACAC 270 photocatalyst under magnetic stirring. EPR spectra simulations (**c**) and (**d**) using the Easyspin routine in Matlab for the spectra of (**a**) and (**b**), respectively.

In order to quantify the superoxide radicals production by TiO_2-ACAC CTCs, an indirect method was applied using the 2,2,6,6-tetramethylpiperidinol (TEMP) redox probe. TEMP is a spin trap that has singlet oxygen specificity, $^1O_2$, which after capture is transformed into the very stable free radical TEMPOL [90]. Furthermore, some authors reported that superoxide radicals can directly form TEMPOL, since superoxide radical often decays into singlet oxygen [90, 91, 88]. The EPR spectrum of the TEMP adduct, TEMPOL, is a characteristic triplet spectrum caused by hyperfine interaction between the electronic spin S = ½ and the nuclear spin I = 1 of ^{14}N nucleus with hyperfine constant of $a_N = 1.58$ mT in water. Due to the high stability of TEMP adduct (> 24 h) it could be reliably quantified by double integration of the EPR spectra and compared with a sample containing a known concentration of TEMPOL (0.1 M). The experiments with TEMP were performed using the same experimental method employed with DMPO spin trap, substituting DMPO with TEMP (0.1 M).

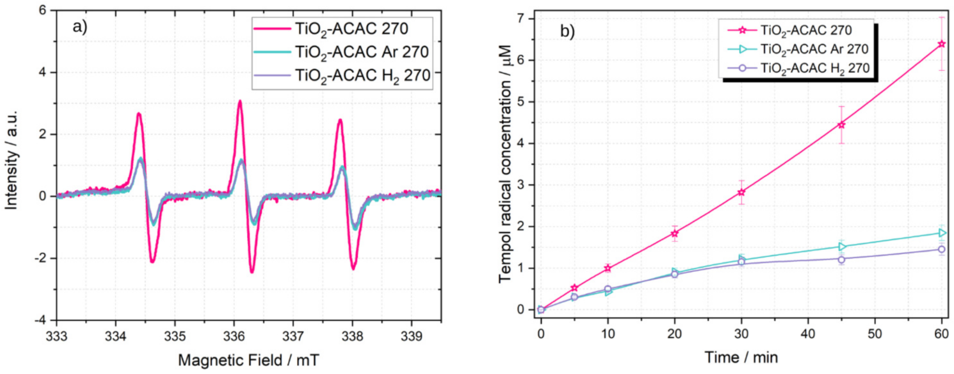

Figure 4.14: (**a**) EPR spectra of TEMPOL radical formed by 10 mg of TiO_2-ACAC 270 (magenta line), TiO_2-ACAC Ar 270 (cyan line) and TiO_2-ACAC H_2 270 (violet line) after 30 min under visible light radiation and (**b**) TEMPOL radical formation as a function of time under visible light radiation for all CTCs.

A comparison between the EPR spectra of TEMPOL radical formed by TiO_2-ACAC CTCs after 30 min under WL illumination is shown in Figure 4.14a. EPR spectra of TEMPOL radical formed by TiO_2-ACAC 270 exhibited the highest intensity compared to the TEMPOL formed by the CTCs calcined under reducing atmospheres. In order to quantify the TEMPOL formed by the TiO_2-ACAC CTCs, the TEMPOL radical concentration as a function of time under visible light radiation was evaluated in Figure 4.14b. Figure 4.14b revealed that the highest concentration of TEMPOL radical is produced by the TiO_2-ACAC 270 CTC, which indirectly implies that CTC calcined in static air produces superoxide radical with higher efficiency compared to CTCs calcined under reducing atmosphere. Consequently, the TC photodegradation efficiency of TiO_2-ACAC 270 should be higher compared to TiO_2-ACAC Ar 270 and TiO_2-ACAC H_2 270, as evidenced in Figure 4.9. In addition, the correlation between TC photodegradation results using scavengers and the DMPO spin trap experiments allows inferring that the superoxide radicals are the dominant ROS species formed by the TiO_2-ACAC CTCs under visible light illumination.

4.3
Discussion

4.3.1
Influence of extrinsic oxygen vacancies on the lattice parameters, optical and photochemical properties

The XRPD results of TiO_2-ACAC CTCs (Figure 4.3) evidenced a decrease in the lattice parameters of the CTCs calcined under reducing atmosphere (TiO_2-ACAC Ar 270 and TiO_2-ACAC H_2 270) in comparison to CTC calcined under static air due to crystal structure relaxation generated by the increase of extrinsic oxygen vacancies concentration in the TiO_2-ACAC CTCs. This lattice distortions, also observed by Pan et al. [38] and Chen et al. [39], led to positive displacement in the Ti 2p binding energy (Figure 4.8d).

The EPR and XPS measurements (Figures 4.7 and 4.8) did not reveal the presence of Ti^{3+}, which would imply a negative shift in the Ti 2p binding energy and as a consequence an increase in the lattice parameters [39, 42, 92, 93]. In addition, this result is an indication that the charge compensation in the TiO_2-ACAC CTCs occurs, predominantly, through electronic compensation, which led to the formation of F^+ centers (see Equation 4-3 in section §4.2.3 and Figure 4.6).

The increase of surface/bulk extrinsic oxygen vacancies in the TiO_2-ACAC CTCs extended the visible light sensitization of the CTCs due to the simultaneous action between the LMCT mechanism and the optical centers created through the calcination process (Figures 4.5 and 4.6).

Tetracycline photodegradation results (Figure 4.9) confirmed the hypothesis that TiO_2-ACAC CTCs are able to degrade pollutants in aqueous medium, using a low concentration of photocatalytic material ($50 \text{ mg} \cdot \text{L}^{-1}$) under low-power visible light (26 W). Wu et al. [42] reported 66.2% removal efficiency of TC after 4 h, using $20 \text{ mg} \cdot \text{L}^{-1}$ of Black-TiO_2 exposure to very high-power visible light (1000 W). Additionally, Almeida et al. [70] related 68.6% of TC photocatalytic abatement after 6 h, using $200 \text{ mg} \cdot \text{L}^{-1}$ of TiO_2 covered by ACAC and calcined at 300 °C exposure to low-power visible light excitation (26 W). Therefore, the TC photodegradation reported in our study (70.1%), using $50 \text{ mg} \cdot \text{L}^{-1}$ of TiO_2-ACAC 270 after 6 h under low-power visible light (26 W) was higher than that reported by Wu et al. [42] with 2.5-fold higher photocatalyst concentration but under $\sim$ 38.5-fold lower visible light power and was also slightly higher than that related by Almeida et al. [70] but with four times lower concentration of photocatalyst under the same visible light power (26 W).

In contrast to what has been reported by some authors [42, 43, 39, 14], it was observed that the calcined CTC with lowest light absorption (TiO_2-ACAC 270) exhibited the highest photocatalytic performance for TC degradation.

The results of TC photodegradation by TiO_2-ACAC CTCs (Figures 4.9 - 4.12) allowed for indirect determination of the presence of oxygen vacancies on the TiO_2-ACAC CTCs surface, since as reported by Li et al. [40] the coupling of TiO_2-based nanostructures with only bulk extrinsic oxygen vacancies would induce low photocatalytic activity.

4.3.2
ROS production capacity of TiO_2-ACAC CTCs

One of the main goals of this work was to study the ROS generation capacity of TiO_2-ACAC CTCs and to understand the mechanisms involved in the degradation of pollutants, using tetracycline as a testing pollutant. The photodegradation tests using BQ and IPA scavengers (Figures 4.10 - 4.12) revealed that the superoxide radical plays the main role in the TC degradation. Therefore, the highest photocatalytic performance of TiO_2-ACAC 270 in the TC degradation was directly related to its high efficiency in the superoxide radicals production compared to TiO_2-ACAC Ar 270 and TiO_2-ACAC H_2 270 (Figura 4.14).

This efficiency in the superoxide radicals generation for the TiO_2-ACAC 270 might be attributed to the coupling between an adequate concentration of extrinsic oxygen vacancies with LMCT mechanism, since, as reported by other authors [40, 41, 61], the oxygen vacancies in the bulk act as recombination centers, while the oxygen vacancies on the surface favor the photocatalytic process through the increase of the active sites on the surface and the enhancement of charge separation in the nanostructure. Furthermore, a higher content of ACAC in the TiO_2-ACAC Ar 270 and TiO_2-ACAC H_2 270 was not necessary beneficial for the photocatalytic process. This would be because ACAC might be occupying the active sites on the surface of CTCs, hindering the interaction of O_2 and H_2O with the nanostructure surface, and as a consequence, causing a reduction in the ROS generation.

To understand the mechanisms involved in the TC photodegradation by TiO_2-ACAC CTCs, the electronic bands scheme represented in the Figure 4.15 was proposed. The electronic bands model for LMCT mechanism, shown in Figure 4.15a, has been widely reported in literature [8, 44, 43]. In fact, the PL peak of TiO_2-ACAC CTCs centered at 2.40 eV (Figure 4.6) is the fingerprint of LMCT mechanism formed between organic molecule (ACAC) and anatase. Figure 4.15b represents the electronic band structure model for the oxygen vacancies in the anatase. This model, reported by Nakamura et al. [94], was based on the work carried out by Cronemeyer [95], who found that the bandgap energy between the conduction band and the donor states attributed to extrinsic oxygen vacancies varies between 0.75 - 1.18 eV for TiO_2. However, an extension of these donor states can be induced by increasing the concentration of extrinsic oxygen vacancies, being able to partially overlap the conduction band in the highly oxygen-deficient TiO_2 [96].

Considering the two previously described models, the electronic bands scheme for anatase with extrinsic oxygen vacancies coupled to the LMCT mechanism was proposed in Figure 4.15c, where the visible light absorption by TiO_2-ACAC CTCs could promote four electron transitions: (1) from HOMO of ACAC to CB of anatase, (2) from HOMO of ACAC to bulk extrinsic oxygen vacancies levels, (3) from bulk extrinsic oxygen vacancies levels to CB of anatase and (4) from the ground state of F^+ center to its corresponding excited state F^{+*} [39].

As a result of the electronic transitions (1) and (2), *i.e.*, from the HOMO to CB and from HOMO to bulk extrinsic oxygen vacancies, electronic holes are generated in the HOMO of ACAC. Additionally, there are different pathways for charge carriers as result of the electronic photoexcitation: (1) migration of charge carriers to the surface, where surface extrinsic oxygen vacancies can capture electrons promoting the separation of photogenerated charge carriers; (2) recombination of e^-/h^+ pair at the bulk. The migration of the photogenerated charge carriers to the surface leads to the generation of the superoxide radical, as a consequence of the interaction between the electron and oxygen (Equation 4-10), coming from conduction band of TiO_2 and the reaction medium (water or atmosphere), respectively, and to two types of interaction *via* h^+, coming from the HOMO of ACAC: (1) interaction with TC, which leads to a direct route of the pollutant degradation [87]; (2) interaction with water (Equation 4-11), leading to a water splitting through which superoxide radicals (Equation 4-10) and hydrogen (Equation 4-12) can be produced [3, 14].

$$O_2 + e^- \rightarrow^{\bullet} O_2^- \tag{4-10}$$

$$2H_2O + 4h^+ \rightarrow O_2 + 4H^+ \tag{4-11}$$

$$2H^+ + 2e^- \rightarrow H_2 \tag{4-12}$$

On the other hand, the recombination kinetics of carriers photogenerated by TiO_2-ACAC CTCs could be described as a function of bulk extrinsic oxygen vacancies concentration (Figures 4.15d and 4.15e), since, as reported by Kato et al. [82], the distribution of bulk extrinsic oxygen vacancies imposes an influence on the recombination rates of photogenerated carriers, *i.e.*, when the bulk extrinsic oxygen vacancies are dispersed, trapped electrons undergo repeated hopping and tunneling, reducing recombination rates. Therefore, the photogenerated carriers could reach the surface of the nanostructure, enhancing the photocatalytic activity. In contrast, when defects are in close proximity, trapped electrons rapidly migrate between defects, increasing recombination rates. Considering the model proposed by Kato et al. [82], TC photodegradation results (Figure 4.9) and bulk extrinsic oxygen vacancies concentration, obtained through EPR (Section §4.2.4), a slow recombination process of e^-/h^+

pair was proposed for TiO_2-ACAC 270 (Figure 4.15d), which exhibited a concentration of bulk extrinsic oxygen vacancies of 2.80×10^{15} cm^{-3}, $\sim$ 3.8 times lower compared to TiO_2-ACAC Ar 270 (1.06×10^{16} cm^{-3}) and $\sim$ 5.0 times lower compared to TiO_2-ACAC H_2 270 (1.30×10^{16} cm^{-3}), while a fast recombination model of e^-/h^+ pair was attributed to TiO_2-ACAC Ar 270 and TiO_2-ACAC H_2 270 (Figure 4.15e).

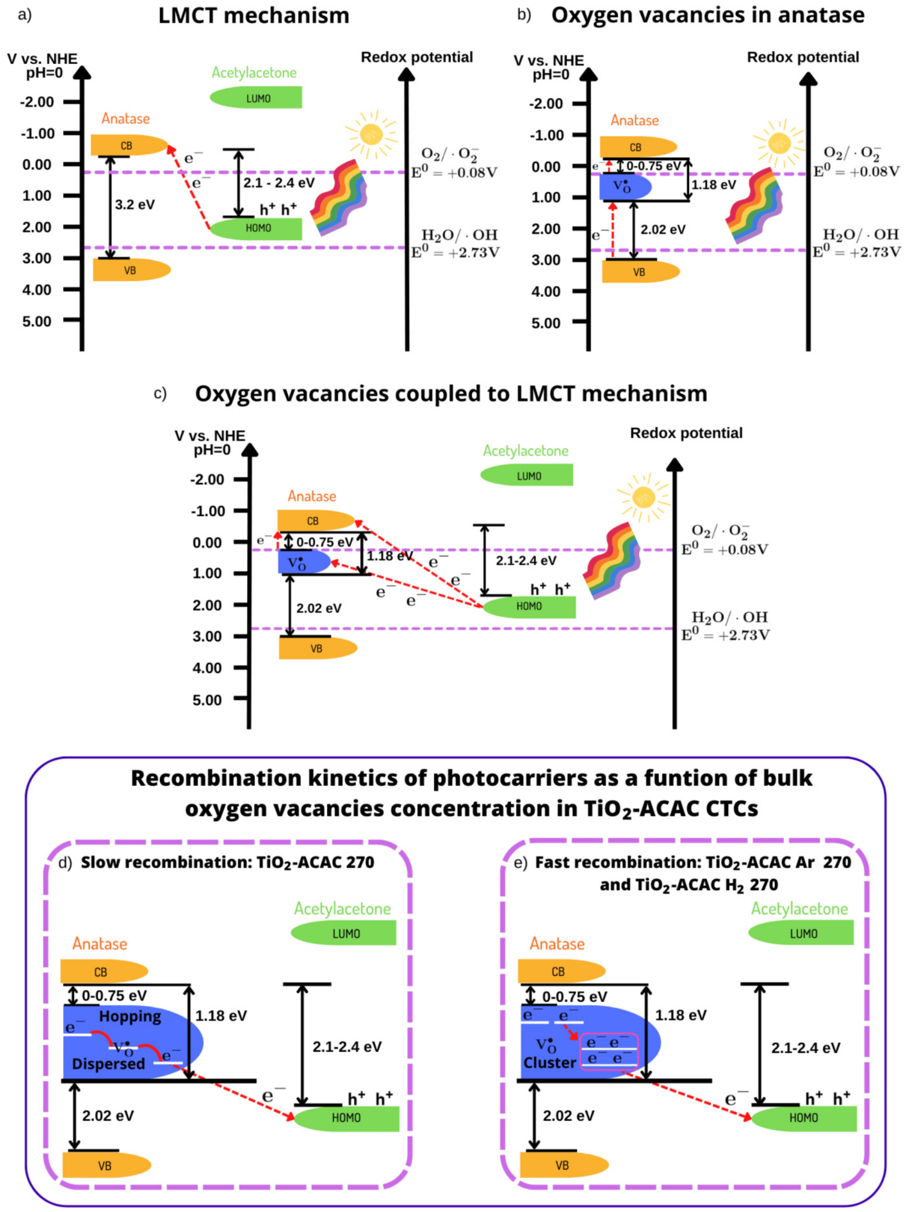

Figure 4.15: Electronic bands scheme for (**a**) TiO_2-ACAC CTCs (LMCT mechanism), (**b**) Oxygen vacancies coupled to anatase and (**c**) oxygen vacancies coupled to TiO_2-ACAC CTCs. (**d**) Slow recombination process of e^-/h^+ pair, proposed for TiO_2-ACAC 270 and (**e**) fast recombination process of e^-/h^+ pair, proposed for TiO_2-ACAC Ar 270 and TiO_2-ACAC H_2 270.

4.4
Conclusions

Dark TiO_2-ACAC CTCs were synthesized *via* sol-gel and calcined under different atmospheres (static air, Ar and H_2). EPR, XRPD and XPS revealed the existence of the bulk/surface extrinsic oxygen vacancies in the TiO_2-ACAC nanostructure and also, indicated that charge compensation mechanism due to the oxygen vacancies in the TiO_2-ACAC CTCs occurs through predominant electronic compensation.

The correlation between EPR-spin trapping analysis and TC photodegradation results using BQ and IPA, as scavengers, highlighted the key role of the superoxide radical in the TC degradation by CTCs.

The photodegradation results indicated that the calcination of TiO_2-ACAC under Ar and H_2 atmospheres was not beneficial for the photocatalytic performance of CTCs, partly because it led to a reduction of the active sites in the CTCs nanostructures due to the high preservation of ACAC on the TiO_2 surface. In addition, CTCs calcined under reducing atmospheres exhibited a high SETOV concentration (1.06×10^{16} cm^{-3} for TiO_2-ACAC Ar 270 and 1.30×10^{16} cm^{-3} for TiO_2-ACAC H_2 270), causing trapped electrons to rapidly migrate between defects due to the proximity between bulk extrinsic oxygen vacancies, resulting in increased recombination rates of photogenerated carriers and consequently in a reduction in ROS formation by these CTCs under visible light radiation.

TiO_2-ACAC 270 exhibited the highest photocatalytic performance in TC degradation due to the best coupling between the LMCT mechanism and an adequate concentration of bulk extrinsic oxygen vacancies, which led to the trapped electrons undergoing repeated hopping and tunneling, reducing the recombination rates and as a consequence, improving the efficiency in the superoxide radicals production.

The findings of this work provide fundamental information about the influence of surface/bulk extrinsic oxygen vacancies on photocatalytic performance, lattice parameters, optical and photochemical properties of TiO_2-ACAC CTCs, which might be extrapolated to other CTCs.

5
Functionalization of anatase nanoparticles with Glutaric acid and their photochemical and photocatalytic properties

5.1
Experimental methods

5.1.1
Synthesis of TiO_2-GA CTCs nanopowders

The synthesis of TiO_2-GA CTCs nanopowders was carried out *via* sol-gel, using two different processes. The reagents were purchased from Sigma-Aldrich and used without further purification. Ethanol (99.8%), glutaric acid (GA, 99%) and titanium isopropoxide ($Ti(OiPr)_4$, 97%) were used in both synthesis processes. Nitric acid (65%) was only used for the first synthesis method.

The first synthesis process for TiO_2-GA xerogel (described in Figure 5.1) was performed following a similar sol-gel route reported by Habran [52] and Almeida [43] for the TiO_2-ACAC, substituting acetylacetone by glutaric acid and keeping the complexing ratio of $(\frac{[GA]}{[Ti]}) = 2$.

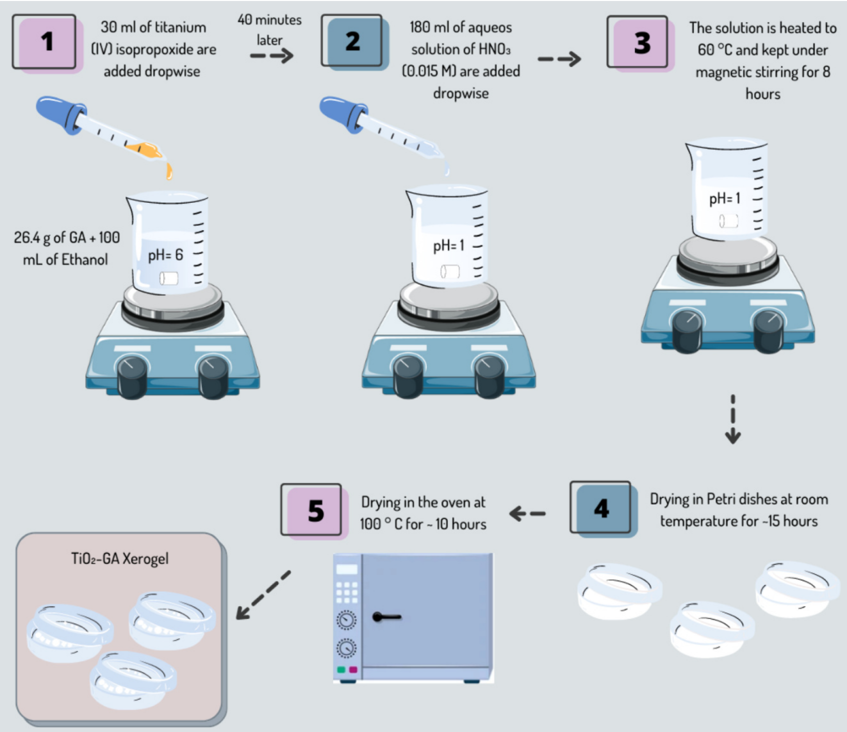

Figure 5.1: Illustration for the first sol–gel synthesis process of TiO_2-GA xerogel (TiO_2-GA1).

In the second synthesis process for TiO_2-GA xerogel (described in Figure 5.2), some modifications, optimized through many different syntheses, were performed compared to the first synthesis process. The second synthesis process was carried out without addition of nitric acid and using a complexing ratio of $(\frac{[GA]}{[Ti]}) = 1$. In this synthesis method, to induce the hydrolysis reaction, 180 mL of the acid solution (0.091 M) containing 2.20 g of GA were added dropwise to the isopropoxide solution, maintained under magnetic stirring, containing 17 mL of ethanol with 5 mL of titanium (IV) isopropoxide. Subsequently, the solution was kept under magnetic stirring and heated to 60 °C for 8 h to promote the condensation reaction. Afterwards, a white gel was obtained by drying at Petri dishes at room temperature for 37 h. Finally, the gel was dried at 80 °C for ∼15 h.

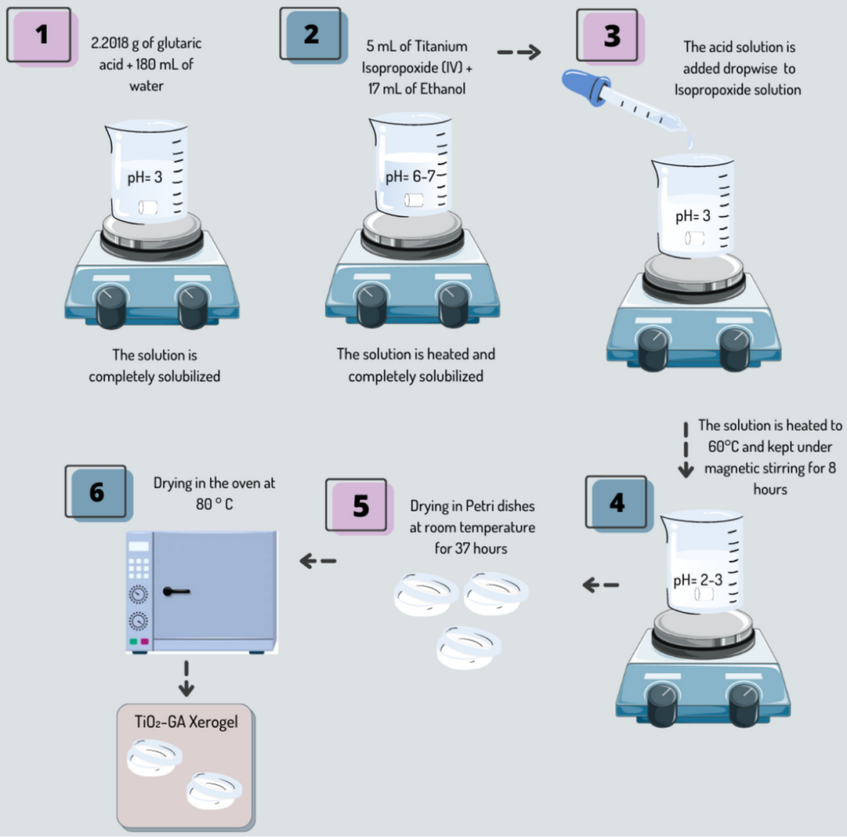

Figure 5.2: Illustration for the second sol–gel synthesis process of TiO_2-GA xerogel (TiO_2-GA2).

As a result of both synthesis methods, beige color TiO_2 xerogels (denoted TiO_2-GA) were obtained. TiO_2-GA xerogels were further ground in an agate mortar and calcined for 2 h, using a horizontal tubular furnace, at 270 °C under static air. Table 5.1 presents the nomenclature of the samples.

Table 5.1: TiO_2-GA nanopowders nomenclature.

Samples	**Description**
TiO_2-GA1	TiO_2-GA xerogel obtained by the first synthesis process
TiO_2-GA1 270	TiO_2-GA obtained through the first synthesis process and calcined at 270 °C under static air
TiO_2-GA2	TiO_2-GA xerogel obtained by the second synthesis process
TiO_2-GA2 270	TiO_2-GA obtained through the second synthesis process and calcined at 270 °C under static air

5.1.2
Characterization techniques

TiO_2-GA CTCs were studied using the same characterization techniques previously described in chapter §4 for the TiO_2-ACAC CTCs. Additionally, the functionalization of the anatase nanoparticles with Glutaric acid and the formation of the CTC were evaluated through Fourier transform infrared spectroscopy (FTIR). The FTIR was carried out through a Bruker FTIR Spectrometer ALPHA II (Bruker, Billerica, MA, USA). Spectra were recorded between a wave number of 4000 and 400 cm^{-1}, with 32 scans and 4 cm^{-1} resolution.

5.2
Results

5.2.1
XRPD of TiO_2-GA CTCs

Crystal phase analysis of TiO_2-GA1, TiO_2-GA2, TiO_2-GA1 270 and TiO_2-GA2 270 nanopowders was carried out by XRPD. The XRPD patterns of TiO_2-GA xerogels (TiO_2-GA1 and TiO_2-GA2), presented in Figure 5.3a, evidenced the presence of anatase (PDF-2: 21-1272) and glutaric acid phases (PDF-2: 38-1886 and 51-1902), while the XRPD patterns of TiO_2-GA1 270 and TiO_2-GA2 270, shown in Figure 5.3b, exhibited diffraction peaks corresponding only to crystallographic planes of the anatase phase (PDF-2: 21-1272). XRPD peaks corresponding to GA phases were not observed in TiO_2-GA1 270 and TiO_2-GA2 270 since the calcination of TiO_2-GA xerogels under static air at 270 °C led to partial decomposition of the glutaric acid on the TiO_2-GA nanostructure (*vide infra* §5.2.3).

In addition, a slight shift towards lower 2θ angles was observed for the diffraction peaks of TiO_2-GA2 270 compared to TiO_2-GA1 270 (inset of Figure 5.3b). This slight shift is directly related to the increase in unit-cell volume of anatase (Figure 5.3c) as a result of two competing effects: (1) the lattice contraction due to crystal structure relaxation generated by increase of oxygen vacancies in TiO_2-GA1 270 compared to TiO_2-GA2 270 [38, 39], (2) lattice expansion due to increase of cationic radius (from 0.48 Å to 0.56 Å) as a consequence of the partial reduction of cationic charge from Ti^{4+} to Ti^{3+}, identified for TiO_2-GA2 270 (*vide infra* §5.2.5) [97, 98, 99].

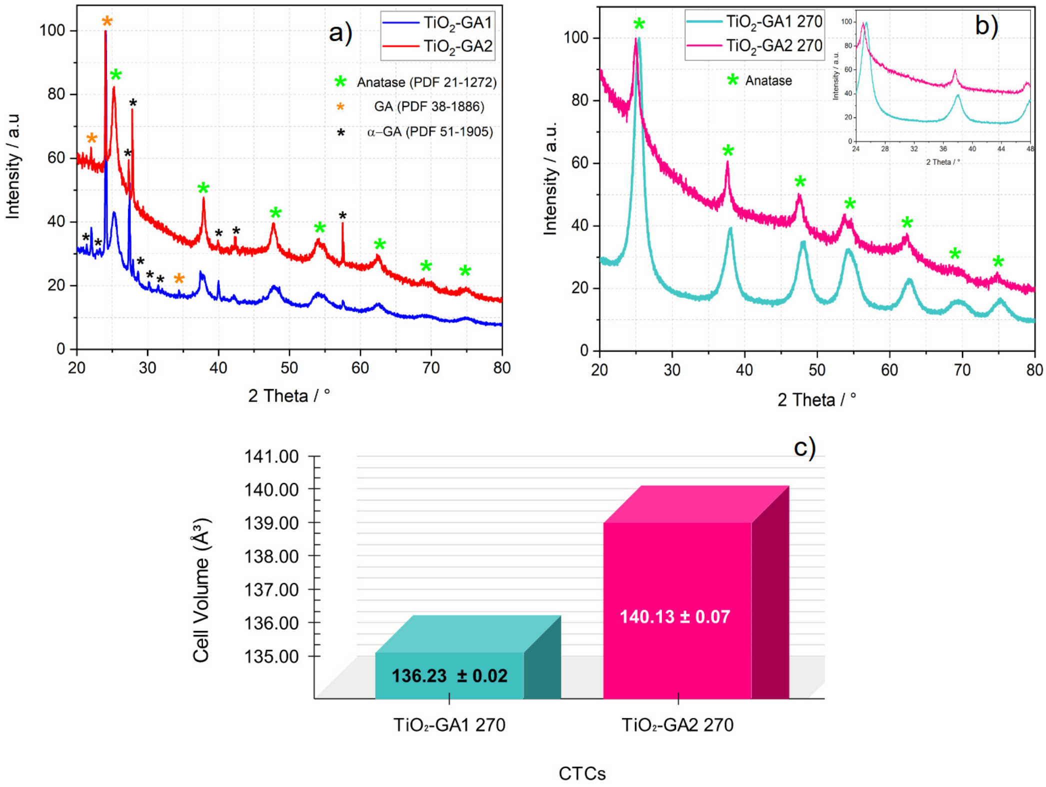

Figure 5.3: XRPD patterns of (**a**) TiO_2-GA1 and TiO_2-GA2 xerogels and (**b**) TiO_2-GA1 270 and TiO_2-GA2 270. (**c**) Comparison between the anatase unit-cell volumes of TiO_2-GA1 270 and TiO_2-GA2 270.

The mean crystallite size and lattice parameters of anatase in TiO_2-GA1 270 and TiO_2-GA2 270, determined by Rietveld refinement (see the XRPD patterns fitting in Figure S3, Supplementary Information), are shown in Table 5.2. TiO_2-GA1 270 and TiO_2-GA2 270 exhibited a mean crystallite size of 4.21 ± 0.03 nm and 6.14 ± 0.30 nm, respectively, supporting the influence of the chelating agent, previously reported by Scolan et al. [48] and Siwińska-Stefańska et al. [49], on the crystallite size of TiO_2 synthesized *via* sol-gel, since the rates of hydrolysis and condensation of the metal alkoxide can be controlled by the addition of the complexing ligands, such as dicarboxylic acids.

Table 5.2: Lattice parameters of anatase and mean crystalline sizes of TiO_2-GA1 270 and TiO_2-GA2 270, obtained by Rietveld refinement.

Sample	**a (Å)**	**c (Å)**	**Unit-cell volume ($Å^3$)**	**Mean crystallite size (nm)**
TiO_2-GA1 270	3.7878 ± 0.0002	9.4951 ± 0.0010	136.23 ± 0.02	4.21 ± 0.03
TiO_2-GA2 270	3.8300 ± 0.0007	9.5529 ± 0.0034	140.13 ± 0.07	6.14 ± 0.30

5.2.2
FTIR of TiO_2-GA CTCs

The functionalization by GA on the TiO_2 surface and formation of CTC were evaluated through FTIR spectra. Figure 5.4 shows a comparison between the FTIR spectra of GA, TiO_2-GA1 and TiO_2-GA1 270. TiO_2-GA1 exhibited almost the same FTIR bands as GA due to the free molecules unattached to the surface of TiO_2. The typical bands around 2500-3300 cm^{-1}, observed for GA and TiO_2-GA1, were attributed to the O–H stretching band, a characteristic of dicarboxylic acids, such as GA [100]. The C=O stretching vibration was observed at 1683 cm^{-1} for GA and at 1677 cm^{-1} for TiO_2-GA1. The bands located at 1406 cm^{-1} and at 909 cm^{-1}, observed for GA and TiO_2-GA1, were attributed, respectively, to the in-plane vibration and the out-plane vibration of O–H bending [100, 65]. C–O stretching bands for carboxylic acids were observed between 1320 and 1210 cm^{-1} in GA and TiO_2-GA1. The FTIR bands at 1522 cm^{-1} and at 1515 cm^{-1}, observed for TiO_2-GA1 and TiO_2-GA1 270, respectively, were attributed to asymmetric carboxyl stretching, while the FTIR band at 1401 cm^{-1}, observed for TiO_2-GA1 270, was attributed to symmetric carboxyl stretching [101, 66, 102]. The symmetric carboxyl stretching band, in the FTIR spectrum of TiO_2-GA1, is overlapped with other vibrational bands corresponding to free unreacted GA molecules.

The formation of the complex, formed between TiO_2 and GA molecule, for TiO_2-GA1 and TiO_2-GA1 270 was identified through the wavenumber distance between the asymmetric and symmetric carboxyl stretching bands ($\Delta\nu = \nu_{\text{asymmetric}} - \nu_{\text{symmetric}}$). The obtained value of $\Delta\nu = \nu_{\text{asymmetric}} - \nu_{\text{symmetric}} = \Delta\nu = 1515 - 1401 = 114$ cm^{-1} is a fingerprint of the formation of the complex *via* bidentate chelating-type interaction [103, 104, 105] between GA and titanium dioxide, as reported by Zavala et al. [66].

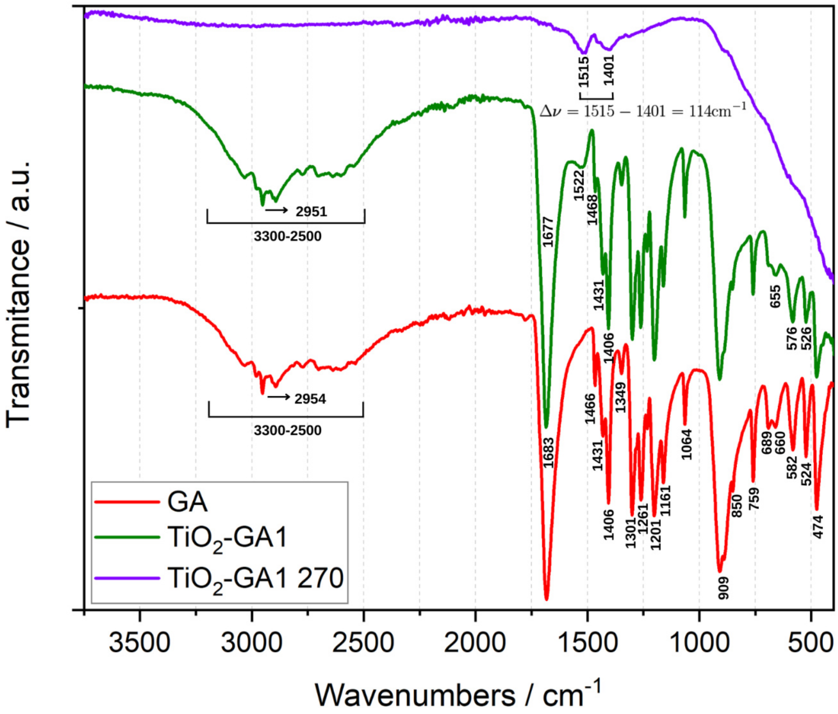

Figure 5.4: FTIR spectra of GA, TiO_2-GA1, TiO_2-GA1 270.

The comparison between the FTIR spectra of GA, TiO_2-GA2 and TiO_2-GA2 270 is shown in Figure 5.5. Unlike the TiO_2-GA1 FTIR spectra, TiO_2-GA2 did not show all the FTIR bands due to GA, which might be an indication of the lower amount of unreacted free GA molecules on the TiO_2 surface compared to TiO_2-GA1 complex. Furthermore, it was observed (Figure 5.5) that calcination under static air (TiO_2-GA2 270) led to stronger vibration bands related to the asymmetric vibration of carboxylate (1517 cm $^{-1}$) and the symmetric vibration of carboxylate (1404 cm $^{-1}$). These bands observed in TiO_2-GA2 270 and in TiO_2-GA2 (at 1520 cm $^{-1}$ and at 1408 cm $^{-1}$) evidenced the formation of the bidentate complex between GA and TiO_2, exhibiting a $\Delta\nu = 1520 - 1408 = 112$ cm^{-1} [66, 103, 104, 105], in accord to previously reported for TiO_2-GA1 270.

On the other hand, unlike TiO_2-GA1 270 CTC (Figure 5.4), other bands located between 1305 cm $^{-1}$ and 1006 cm $^{-1}$ were observed for the TiO_2-GA2 270 CTC (Figure 5.5), indicating a higher amount of the GA organic molecule on the TiO_2 surface for the TiO_2-GA2 270 CTC compared to the TiO_2-GA1 270 CTC (*vide infra* §5.2.3).

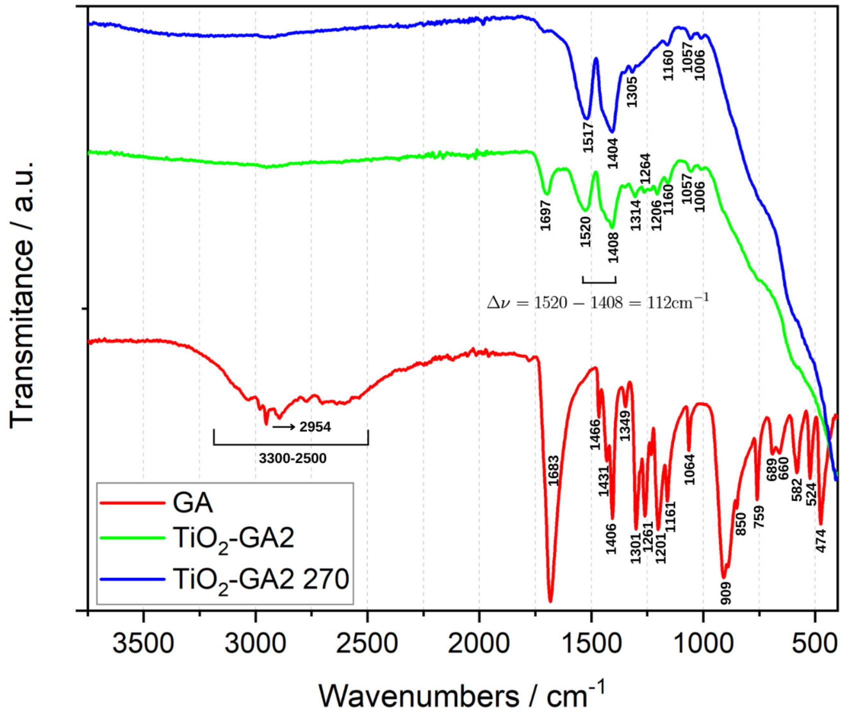

Figure 5.5: FTIR spectra of GA, TiO_2-GA2, TiO_2-GA2 270.

Therefore, considering the FTIR analysis and the possible binding modes of dicarboxylic acids to the TiO_2 surface as reported by Thomas et al. [106], the scheme of the two possible types of bidentate chelating bonds formed between GA and TiO_2 was drawn in Figure 5.6.

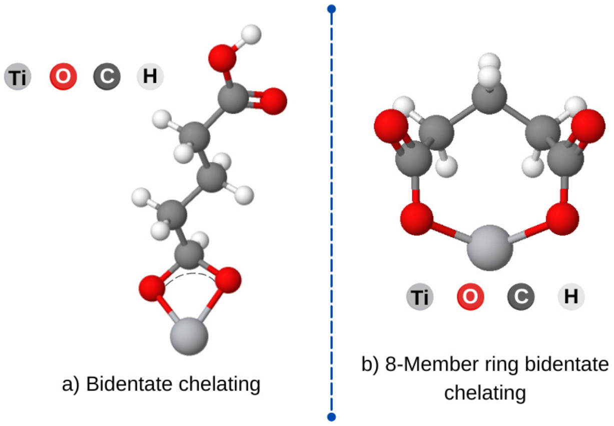

a) Bidentate chelating

b) 8-Member ring bidentate chelating

Figure 5.6: Two possible bidentate chelating-type functionalizations of TiO_2 by GA.

5.2.3
TGA of TiO_2-GA CTCs

The TGA curves of the TiO_2-GA1 270 and TiO_2-GA2 270 (Figure 5.7) showed three mechanisms of mass loss, evidenced through the maximum and minimum in the DTG curves, in accord to that reported by Zapata-Tello et al. [65]. The volatilization of adsorbed water was attributed to the first mechanism that occurs up to a temperature of 150 °C [48]. The other mechanisms of mass loss represented by the first local maximum and the second minimum in the DTG curves, located between 206 - 222 °C and between 365 - 379 °C, respectively, were assigned to the thermal fragmentation of the GA molecules bounded to the TiO_2 surface [65]. In addition, a fourth mechanism of mass loss was found only for TiO_2-GA2 270 at 478 °C, also attributed to the thermal decomposition of GA.

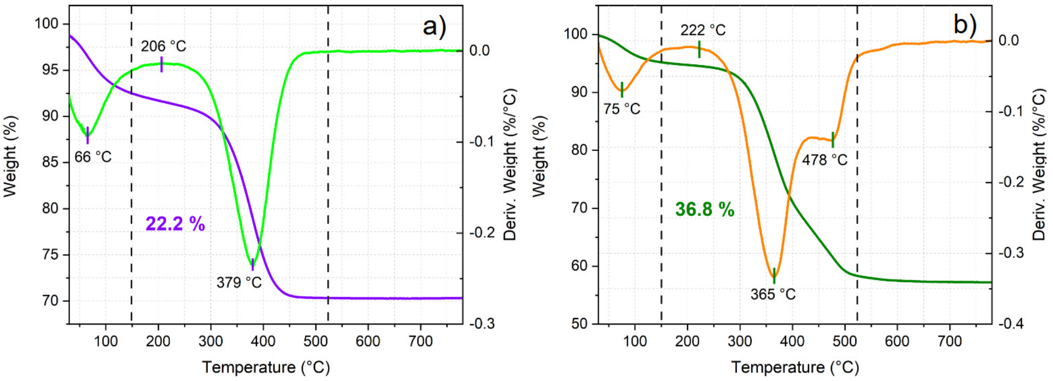

Figure 5.7: TGA/DTG curves of (**a**) TiO_2-GA1 270 and (**b**) TiO_2-GA2 270. The vertical dashed lines mark the temperature range related to the overall mass loss of GA. The percentages in Figures a and b represent the total mass loss of GA in the temperature range from 150 °C to 522 °C.

The amount of glutaric acid in the TiO_2-GA CTCs was determined through the overall mass loss due to glutaric acid fragmentation, which occurs in the temperature range from 150 °C to 522 °C (Figures 5.7 and S4, Supplementary Information). As expected, the calcination process led to a decrease in the content of GA molecules in the CTCs (Figure S4, Supplementary Information), from 70.4% for TiO_2-GA1 xerogel to 22.2% for TiO_2-GA1 270 and from 42.5% for TiO_2-GA2 xerogel to 36.8% for TiO_2-GA2 270, due to partial thermal decomposition of the GA during the calcination at 270 °C [65, 66]. However, a higher percentage of glutaric acid was detected for the TiO_2-GA2 270 CTC compared to the TiO_2-GA1 270 CTC (Figure 5.7). This result is in accordance with the observation in the FTIR (Section §5.2.2). Nevertheless, a high amount of the GA bounded to the TiO_2 surface, such as in TiO_2-GA2 270, might not be beneficial, since GA could occupy the active sites on the photocatalyst surface and might negatively affect the photocatalytic performance of the TiO_2-GA CTCs.

5.2.4
Optical properties of TiO_2-GA CTCs

Figure 5.8 represents the DRS spectra of TiO_2-GA1, TiO_2-GA2, TiO_2-GA1 270, TiO_2-GA2 270, GA and neat anatase (commercial TiO_2 powder, 99.9%, purchased from Vetec). GA and anatase showed no visible light absorption, with band-gap energy of 3.34 eV and 3.26 eV, respectively (Figure 5.8b). TiO_2-GA1 and TiO_2-GA2 exhibited a slight shift in the absorption tail to visible spectrum compared to anatase (Figure 5.8a), exhibiting an apparent band-gap energy of 3.18 eV and 3.24 eV, respectively (Figure 5.8b). This slight shift in the absorption edge could be attributed to the ligand-to-metal charge transfer (LMCT) mechanism, *i.e.*, to the excitation of the electrons in the HOMO of GA to the conduction band of the TiO_2, as reported by Milićević et al. [107] for the CTC formed between TiO_2 nanoparticles and thiosalicylic acid. TiO_2-GA1 and TiO_2-GA2 exhibited beige color, in accordance to reported by Kim et al. [108] for the CTC formed between glucose and TiO_2.

On the other hand, a high sensitization to visible light of TiO_2 was evidenced for the TiO_2-GA1 270 and TiO_2-GA2 270 CTCs, which presented long absorption tails in the visible light spectrum with a slight decrease in light absorption starting at 500 nm, exhibiting a brown color, with an apparent band-gap energy of 1.30 eV and 1.76 eV, respectively. The visible light sensitization of TiO_2, exhibited for TiO_2-GA1 270 and TiO_2-GA2 270 can be ascribed to the contributions of the LMCT mechanism, formed between GA and TiO_2, and the oxygen vacancies in the TiO_2-GA CTCs (*vide infra* §5.2.5), created through the partial decomposition of the glutaric acid molecules bounded to the TiO_2 surface, during the calcination process.

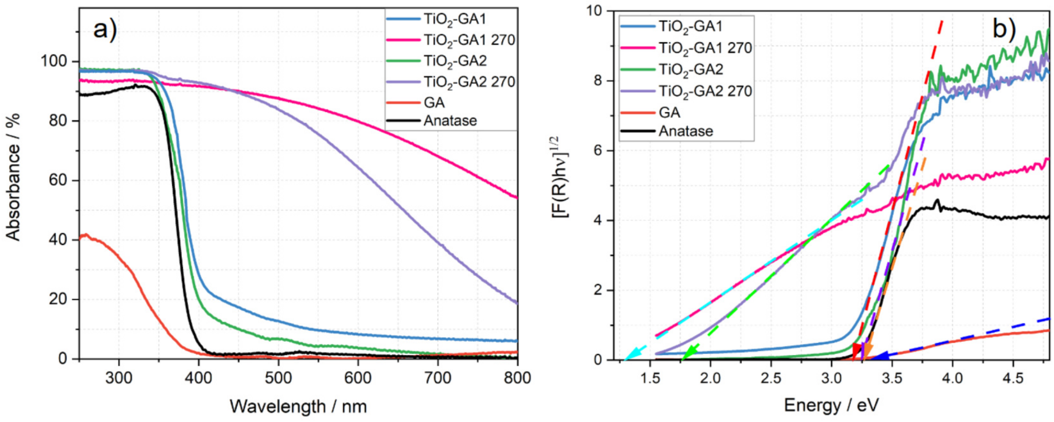

Figure 5.8: (**a**) DRS curves and (**b**) Kubelka-Munk plots of TiO_2-GA1, TiO_2-GA1 270, TiO_2-GA2, TiO_2-GA2 270, GA and neat anatase.

The optical centers created through oxygen vacancies into TiO_2-GA CTCs and the LMCT mechanism formed between GA and TiO_2 were evaluated by PL emission spectra. The emission spectra of TiO_2-GA1 270 (Figure 5.9a) and TiO_2-GA2 270 (Figure 5.9b), in the energy range from 1.82 eV to 3.0 eV, with excitation at 3.57 eV (λ_{exc} = 350 nm), were deconvoluted keeping the same parameters of the known bands.

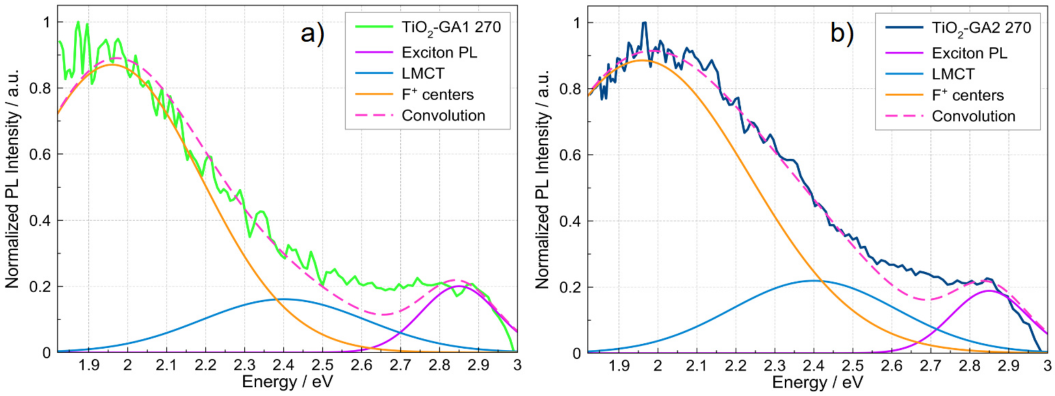

Figure 5.9: Normalized photoluminescence emission spectra of (**a**) TiO_2-GA1 270 and (**b**) TiO_2-GA2 270.

In both PL emission spectra, three bands were observed with maxima at 2.85 eV, 2.40 eV and 1.96, with HWHM of 0.10 eV, 0.25 eV and 0.32 eV, respectively. The band centered at 2.85 eV was attributed to the exciton photoluminescence [75, 76, 77], the second band (at 2.40 eV) to the emission of free electrons from the anatase conduction band (CB) to the highest occupied molecular orbital (HOMO) of glutaric acid through the LMCT mechanism [43, 52, 72, 44] and the third band (at 1.96 eV) was attributed by Serpone [58] and Chen et al. [59] to F^+ center electronic transitions. Therefore, the third band of PL emission spectra of TiO_2-GA CTCs is attributed to the excitation of the single electron trapped in oxygen vacancies (SETOV)[77].

5.2.5
Electron paramagnetic resonance and X-ray photoelectron spectroscopy of TiO_2-GA CTCs

Electron paramagnetic resonance spectra at room temperature were acquired to determine the presence of the oxygen vacancies in the TiO_2-GA CTCs. Figure 5.10a shows the EPR signals of TiO_2-GA1 270 and TiO_2-GA2 270. The first derivative of the absorption spectra of the CTCs evidenced the presence of the bulk oxygen vacancy $V_{O}^{\bullet}$, with a Landé g-factor g = 2.00, characteristic of the SETOV, *i.e.*, $V_{O}^{\bullet}$ in the TiO_2 [83]. In addition, the EPR signal with a Landé g-factor g = 1.94 was observed for the TiO_2-GA2 270 CTC. This EPR signal was attributed by Cui et al. [111] to Ti^{3+} in anatase. Therefore, the charge compensation in the TiO_2-GA1 270 structure would occur predominantly through an electronic compensation process (Equation 5-1), while for TiO_2-GA2 270 it would occur through ionic compensation (Equation 5-2).

$$\text{SETOV} = \text{V}_\text{O} + 1\text{e}^- = \text{V}_\text{O}^\bullet \equiv \text{F}^+ \tag{5-1}$$

$$\text{SETOV} + \text{Ti}^{3+} = \text{V}_\text{O} + 1\text{e}^- + \text{Ti}^{4+} + 1\text{e}^- = \text{V}_\text{O}^\bullet + \text{Ti}^{3+} \equiv \text{F}^+ + \text{Ti}^{3+} \tag{5-2}$$

In addition, it was observed that the intensity of the EPR signal corresponding to SETOV is higher for TiO_2-GA1 270 compared to TiO_2-GA2 270, which implies that the concentration of bulk oxygen vacancies of the TiO_2-GA1 270 CTC (2.1×10^{15} cm^{-3}) is higher compared to the TiO_2-GA2 270 CTC (6.0×10^{14} cm^{-3}), in accord to DRS results. The Ti^{3+} concentration of the TiO_2-GA2 270 CTC was also determined by double integration of the EPR signal, obtaining a value of 4.4×10^{15} cm^{-3}. Therefore, the concentration of Ti^{3+} defects is ~2-fold higher than the SETOV concentration of TiO_2-GA1 270 and one order of magnitude greater than the SETOV concentration of TiO_2-GA2 270, in agreement with the XRPD results. However, the X-ray photoelectron spectra of TiO_2-GA1 270 and TiO_2-GA2 270, shown in Figures 5.10b and 5.10c, did not show the presence of Ti^{3+}. In fact, the X-ray photoelectron spectra for both TiO_2-GA1 270 and TiO_2-GA2 270 exhibited two XPS peaks around ~458 eV and ~464 eV corresponding to Ti^{4+} $2p_{3/2}$ and Ti^{4+} $2p_{1/2}$, respectively [97], with a distance between the binding energies ($\Delta BE = BE(Ti^{4+}\ 2p_{1/2}) - BE(Ti^{4+}\ 2p_{3/2})$) of 5.7 eV, characteristic of Ti^{4+}-O bonds in TiO_2 [97, 85].

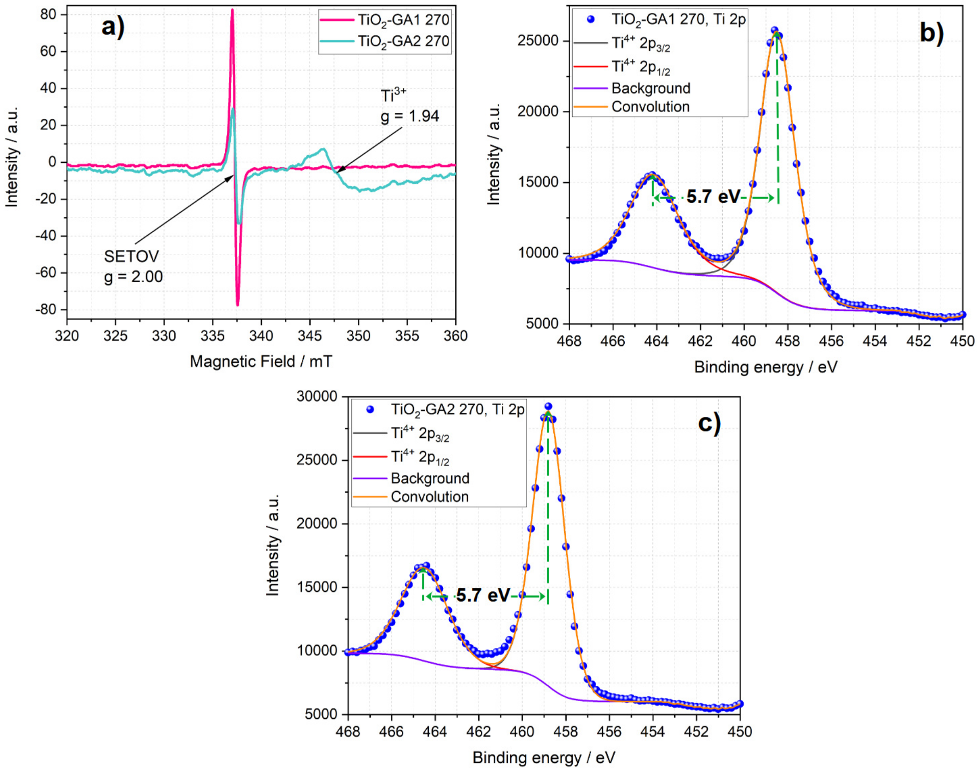

Figure 5.10: (**a**) Electron paramagnetic resonance spectra of TiO$_2$-GA1 270 and TiO$_2$-GA2 270. X-ray photoelectron spectra of Ti 2p for (**b**) TiO$_2$-GA1 270 and (**c**) TiO$_2$-GA2 270.

5.2.6
Photocatalytic performance of TiO$_2$-GA CTCs

The photocatalytic activity of the TiO$_2$-GA CTCs was evaluated by monitoring the tetracycline degradation in aqueous medium using a low photocatalyst concentration (100 mg·L^{-1}) under low-power visible light radiation (26 W). The TC reduction during its photocatalytic degradation in the presence of the TiO$_2$-GA CTCs, as photocatalysts, is shown in Figure 5.11a. Adsorption-desorption equilibrium (1 h in dark) and TC photodegradation curves using TiO$_2$-GA1 270 and TiO$_2$-GA2 270 CTCs as photocatalysts are shown in Figure S5 (see the Supplementary Information).

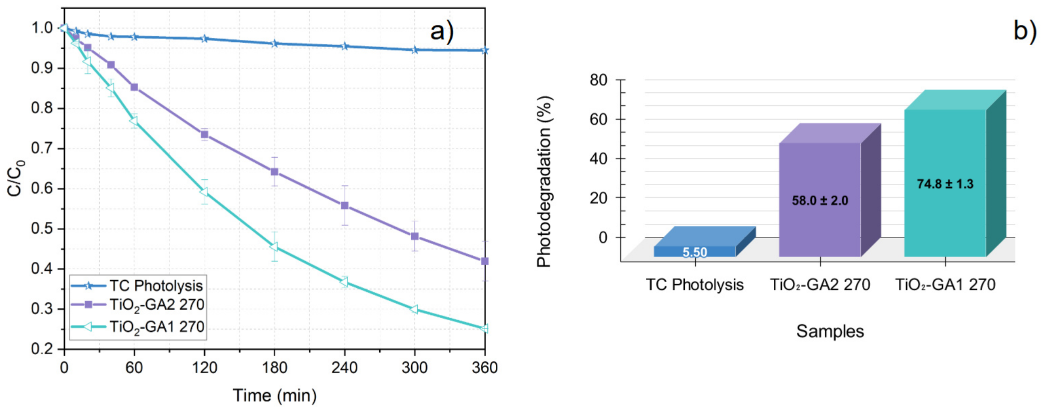

Figure 5.11: (**a**) TC reduction during photocatalytic degradation using TiO_2-GA1 270 and TiO_2-GA2 270 CTCs as photocatalysts and (**b**) TC photodegradation using TiO_2-GA1 270 and TiO_2-GA2 270 CTCs after 6 h under visible light radiation.

As shown in Figure 5.11, photolysis showed insignificant TC degradation. On the other hand, TiO_2-GA1 270 and TiO_2-GA2 270 CTCs caused significant photocatalytic degradation of tetracycline. TiO_2-GA1 270 photodegraded 74.8% ± 1.3% of the TC, while the TiO_2-GA2 270 CTC exhibited a photocatalytic abatement of 58.0% ± 2.0% after 6 h under visible light radiation.

This difference in photocatalytic performance between TiO_2-GA1 270 and TiO_2-GA2 270 for tetracycline abatement could be attributed to two factors: (1) the higher amount of GA bounded to the surface of the TiO_2-GA2 270 photocatalyst (Figure 5.7), which could be occupying the active sites on the TiO_2-GA2 270 surface, resulting in a reduced photocatalytic abatement [43]. (2) Reduced visible light absorption for TiO_2-GA2 270 in comparison to TiO_2-GA1 270 [42, 14, 39].

ROS production for the TiO_2-GA CTCs was evaluated through photocatalytic tests in aqueous medium using benzoquinone and isopropanol, as superoxide (${}^\bullet O_2^-$) and hydroxyl (${}^\bullet OH$) scavengers, respectively.

Figure 5.12 shows the TC photodegradation in the presence of TiO_2-GA1 270, as photocatalyst, with and without the addition of scavengers. As observed in Figure 5.12b, the addition of IPA, as hydroxyl radical scavengers, did not reduce the photocatalytic performance of TiO_2-GA1 270 in the TC photodegradation, but even exhibited a 7.7% higher photocatalytic abatement (82.5% ± 1.7%) compared to that measured without the addition of scavengers (74.8% ± 1.3%). This result could be attributed to the inefficiency in the hydroxyl radical production by the TiO_2-GA1 270 CTC. On the other hand, the addition of the superoxide radical quencher (BQ) caused a significant decrease in TC photodegradation (from 74.8% ± 1.3% to 18.9% ± 2.5%), indicating the key role of the superoxide radical ($^{\bullet}O_2^-$) in the TC photocatalytic degradation by TiO_2-GA1 270 CTC.

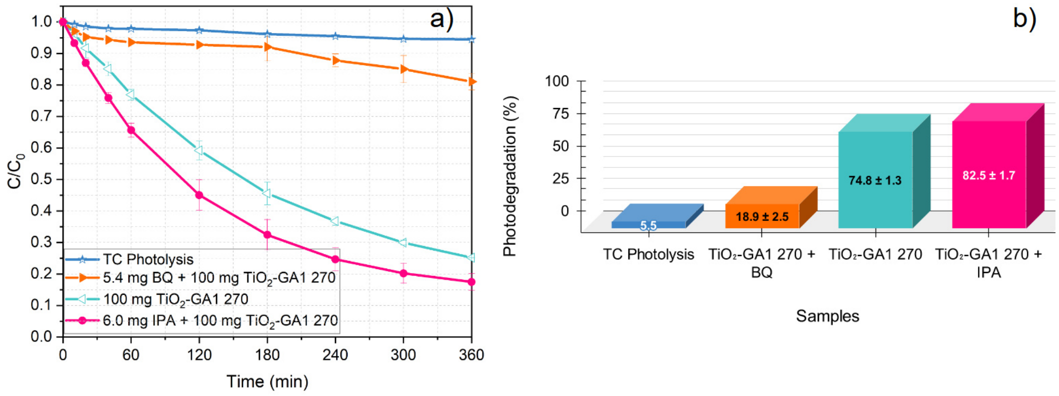

Figure 5.12: (**a**) TC reduction during photocatalytic degradation using TiO_2-GA1 270, as photocatalysts, with and without the addition of BQ and IPA, as scavengers, and (**b**) TC photodegradation using TiO_2-GA1 270 with and without the addition of scavengers (BQ and IPA) after 6 h under visible light radiation.

The evolution of the TC photocatalytic degradation in the presence of the TiO_2-GA2 270 as photocatalyst with and without the addition of scavengers is shown in Figure 5.13a. As displayed in Figure 5.13b, the addition of the scavengers in the presence of the TiO_2-GA2 270 CTC, exhibited a similar behaviour to that observed for TiO_2-GA1 270 CTC, *i.e.*, the addition of BQ caused a significant reduction in the TC photodegradation by the TiO_2-GA2 270 CTC, exhibiting a photocatalytic degradation of only 11.8% ± 2.4% after 6 hours, while the addition of the IPA did not reduce the photocatalytic performance of TiO_2-GA2 270 in the tetracycline photodegradation. In fact, led to a 11.3% higher photocatalytic abatement (69.3% ± 2.0%) compared to the percentage measured without the addition of scavengers (58.0% ± 2.0%). This results indicated that the superoxide radical plays a dominant role in the photocatalytic performance of the TiO_2-GA2 270 CTC in the TC photodegradation and also indicated that the TiO_2-GA2 270 does not efficiently produce hydroxyl radicals ($^{\bullet}OH$) under visible light radiation.

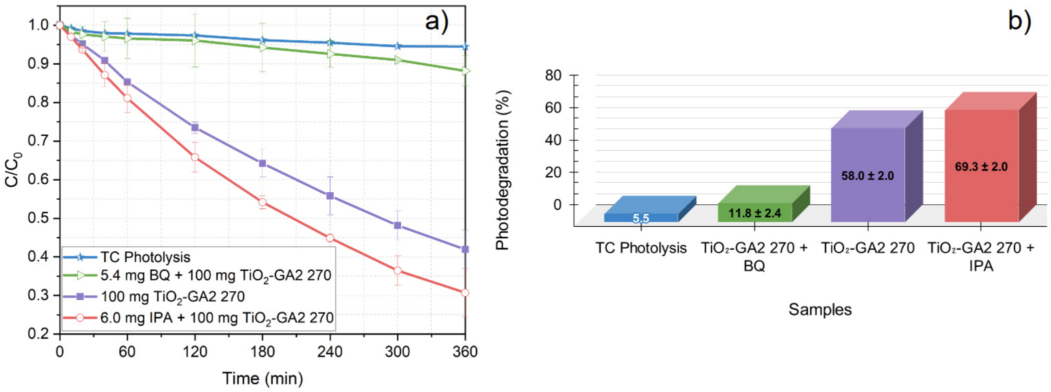

Figure 5.13: (**a**) TC reduction during photocatalytic degradation using TiO_2-GA2 270, as photocatalysts, with and without the addition of BQ and IPA, as scavengers, and (**b**) TC photodegradation using TiO_2-GA2 270 with and without the addition of scavengers (BQ and IPA) after 6 h under visible light radiation.

5.3
Discussion

5.3.1
Formation of the charge transfer complexes by anchoring glutaric acid onto TiO_2 surface

The FTIR results (Figures 5.4 and 5.5) evidenced the formation of the charge transfer complexes between GA and anatase in TiO_2-GA1, TiO_2-GA2, TiO_2-GA1 270 and TiO_2-GA2 270 materials through the bidentate chelating-type interactions (Figure 5.6). The DRS (Figure 5.8) revealed that the bidentate chelating-type interaction between GA and TiO_2 in TiO_2-GA1 and TiO_2-GA2 CTCs led to a slight shift in the absorption edge compared to neat anatase (Figure 5.8a), that would be attributed to the LMCT mechanism, in which light absorption by CTC promotes electrons from the HOMO of the chelating ligand to the CB of anatase. However, the high amount of GA molecules on the TiO_2 surface (Figures 5.4, 5.5 and S4, Supplementary Information) contributed to the low sensibility to visible light of the TiO_2-GA1 and TiO_2-GA2 CTCs, since, as reported by Almeida et al. [43], only the organic molecule strongly bounded to Ti^{4+} on the anatase surface would contribute to the LMCT mechanism. This low visible light absorption by the TiO_2-GA1 and TiO_2-GA2 CTCs was also reported by Bakre et al. [68] for different dicarboxylic acids anchored to TiO_2, by Kim et al. [108] for the CTC formed between glucose and TiO_2 and also by Milićević et al. [107] for the CTC formed between TiO_2 and thiosalicylic acid.

Calcination under static air at 270°C removed the free unreacted GA molecules and partially removed the GA molecules bounded to the TiO_2 surface, introducing oxygen vacancies (*vide infra* §5.3.2) in the structure and extending the light absorption tail far into the visible spectrum of TiO_2-GA1 270 and TiO_2-GA2 270 CTCs (Figure 5.8) due to the interplay between the LMCT mechanism and the F^+ optical centers, created through the calcination process (Figures 5.8 and 5.9). However, the TGA results (Figure 5.7) revealed that the TiO_2-GA CTCs calcined at 270 °C still preserve a high content of glutaric acid bounded to the TiO_2 surface, being higher for TiO_2-GA2 270 (36.8 %) in comparison to TiO_2-GA1 270 (22.2 %).

5.3.2
Formation of oxygen vacancies and their effects on TiO_2-GA CTCs

The XRPD of the TiO_2-GA1 270 and TiO_2-GA2 270 CTCs (Figure 5.3 and Table 5.2) evidenced an expansion in the lattice parameters of anatase for TiO_2-GA2 270 in comparison to TiO_2-GA1 270 as a consequence of the interplay of two opposite and competing effects: (1) the lattice contraction in TiO_2-GA1 270 due to the crystal structure relaxation caused by predominantly electronic charge compensation due to increased bulk oxygen vacancies in TiO_2-GA1 270 (Figure 5.10a), since the removal of an oxygen atom causes a reduction in the Ti-O bond lengths as a consequence of outward relaxation between the titanium atoms. This lattice contraction was also observed by Pan et al. [38] and Chen et al. [39]. (2) Increase of the cationic radius (from 0.48 Å to 0.56 Å) as a consequence of the partial reduction of the cationic charge (from Ti^{4+} to Ti^{3+}) caused by the ionic charge compensation due to bulk oxygen vacancies in the TiO_2-GA2 270 CTC (Figure 5.10a). In the case of TiO_2-GA2 270, the second effect predominates. This kind of lattice expansion was also observed in some other oxides such as TiO_2 [97, 98] and $Al_2W_3O_{12}$ [99].

EPR measurements revealed the existence of bulk oxygen vacancies in the TiO_2-GA1 270 and TiO_2-GA2 270 CTCs. TiO_2-GA1 270 CTC exhibited a higher SETOV concentration than TiO_2-GA2 270, enhancing its response to visible light absorption (Figure 5.8). In addition, bulk Ti^{3+} defects was also observed for TiO_2-GA2 270 CTC by EPR. The concentration of bulk Ti^{3+} defects was higher in comparison to SETOV defects (Section §5.2.5). These results indicated that the charge compensation in the bulk structure of the TiO_2-GA1 270 CTC occurs, predominantly, through electronic compensation leading to F^+ centers formation, while for the TiO_2-GA2 270 CTC occurs through ionic compensation leading to bulk Ti^{3+} defects (Figure 5.9). The difference between the concentration of the bulk Ti^{3+} defects and the SETOV defects for TiO_2-GA2 270 CTC may be attributed to the existence of non-paramagnetic F^{++} centers, *i.e.*, oxygen vacancies with no electrons, which are silent in PL and EPR spectroscopy [58].

On the other hand, some authors have reported that the presence of Ti^{3+} defects can increase the absorption of visible light [112, 113]. However, it was found that TiO_2-GA1 270 (CTC without Ti^{3+} defects) exhibited a longer absorption tail in the visible light spectrum compared to TiO_2-GA2 270 (Figure 5.8). This result could be attributed to the higher SETOV concentration in the TiO_2-GA1 270 CTC (Section §5.2.5), since the localized donor states due to oxygen vacancies contribute to a narrower titania band-gap compared to the localized donor states associated with Ti^{3+} defects in TiO_2. As a consequence, the TiO_2-GA CTC with the highest concentration of SETOV defects (TiO_2-GA1 270) exhibits higher absorption of visible light.

The XPS measurements (Figures 5.10b and 5.10c) did not reveal the presence of Ti^{3+} on the surface of the TiO_2-GA1 270 and TiO_2-GA2 270 CTCs, which is attributed to the predominant interaction between the free electrons with the oxygen, coming from the oxygen vacancies and the reaction medium (water or atmosphere), respectively, leading to the formation of superoxide radicals.

TC photodegradation results (Figure 5.11) proved the hypothesis that TiO_2-GA CTCs calcined at 270 °C are able to degrade pollutants in aqueous medium under low-power visible light radiation (26 W). The only research found in the literature on tetracycline photodegradation using TiO_2-based CTCs as photocatalysts was the work reported by Almeida et al. [70], who reported 68.6% of TC photocatalytic reduction after 6 h, using 200 mg $\cdot$ L^1 of TiO_2 functionalized with acetylacetone and calcined at 300 °C exposed to low-power visible light excitation (26 W). Therefore, the tetracycline photodegradation reported in our study (74.8%), using 100 mg $\cdot$ L^{-1} of TiO_2-GA1 270 after 6 h under low-power visible light radiation (26 W) was slightly higher than that reported by Almeida et al. [70] however, with a 2-fold lower concentration of photocatalyst under the same visible light power radiation (26 W).

5.3.3
ROS production capacity and photocatalytic mechanism of TiO_2-GA CTCs

The photodegradation tests using BQ and IPA scavengers (Figures 5.12 and 5.13) revealed that the superoxide radical plays the main role in the TC degradation. Therefore, the improved photocatalytic performance of TiO_2-GA1 270 in comparison to TiO_2-GA2 270 CTC for TC photodegradation can be attributed to the higher efficiency of superoxide radical generation by the TiO_2-GA1 270 CTC. Furthermore, it was observed that the addition of IPA, as a hydroxyl radical scavenger, led to an increase in TC photodegradation (Figures 5.12 and 5.13). This result could be attributed to the interaction between the electronic holes, coming from the HOMO of GA, with hydroxyl scavengers [86, 3], which could inhibit the secondary reactions between H^+ (formed through electronic holes, Equation 5-3) and $^\bullet O_2^-$ (Equations 5-4 and 5-5). As a consequence, the addition of IPA could limit the chemical reactions of the superoxide radical, promoting only the interactions between $^\bullet O_2^-$ and tetracycline, which results in increased photocatalytic degradation of tetracycline.

$$2H_2O + 4h^+ \rightarrow O_2 + 4H^+ \tag{5-3}$$

$$^\bullet O_2^- + H^+ \rightarrow HO_2^\bullet \tag{5-4}$$

$$^\bullet O_2^- + e^- + 2H^+ \rightarrow H_2O_2 \tag{5-5}$$

Li et al. [40, 41] and Xi et al. [61] reported that surface oxygen vacancies increase the active sites on the photocatalyst surface and enhance the charge separation, while the bulk oxygen vacancies may act as recombination centers. In fact, Xu et al. [98], Qiu et al. [114] and Ren et al. [115] reported that the interaction between surface oxygen vacancies and Ti^{3+} defects led to the separation of the photogenerated charge carriers, reducing the recombination rates and improving the photocatalytic performance. However, our study found that the CTC with lower SETOV bulk oxygen vacancies and Ti^{3+} defect (TiO_2-GA2 270) exhibited the lowest photocatalytic performance for TC degradation. Therefore, the lower TC abatement by TiO_2-GA2 270 in comparison to TiO_2-GA1 270 might be attributed to three factors: (1) the high content of GA molecules on the TiO_2 surface (Figure 5.7), since GA might be occupying the active sites on the surface, limiting the interaction of O_2 and H_2O with the photogenerated charge carriers, causing a reduction in the ROS generation [43]. (2) The enhaced visible light absorption by TiO_2-GA1 270 in comparison to TiO_2-GA2 270 [42, 14, 39], which promotes a higher production of photogenerated charge carriers and, as a consequence, a higher ROS concentration produced by the TiO_2-GA1 270 CTC under visible light radiation. (3) The predominant electronic charge compensation in the TiO_2-GA1 270 CTC, which promotes the formation of F^+ centers and free electrons. As a result, the free electrons can interact with the oxygen adsorbed on the surface, increasing the production of superoxide radicals by the TiO_2-GA1 270 CTC under visible light radiation.

Considering the electronic bands models for the LMCT mechanism formed between organic molecules and anatase [8, 44, 43], oxygen vacancies in TiO_2 [94, 95, 38] and bulk Ti^{3+} defects in anatase [116, 117], the electronic bands scheme for TiO_2-GA1 270 and TiO_2-GA2 270 was proposed in Figure 5.14. The visible light absorption by TiO_2-GA1 270 could promote four electronic transitions (Figure 5.14a): (1) from HOMO of GA to CB of anatase, (2) from HOMO of GA to bulk oxygen vacancies level, (3) from bulk oxygen vacancies levels to CB of anatase and (4) from the ground state of F^+ center to its corresponding excited state F^{+*} [39]. In addition to the electronic transitions mentioned above, electronic transitions involving the Ti^{3+} defect states could also be promoted to CB of anatase in TiO_2-GA2 270 (Figure 5.14b). As a result of the photoexcitation, the photogenerated charge carriers can migrate to the semiconductor surface generating ROS. As previously mentioned, the high ROS production by the TiO_2-GA1 270 CTC can be described as a function of the visible light absorption and the amount of GA molecule on the TiO_2 surface.

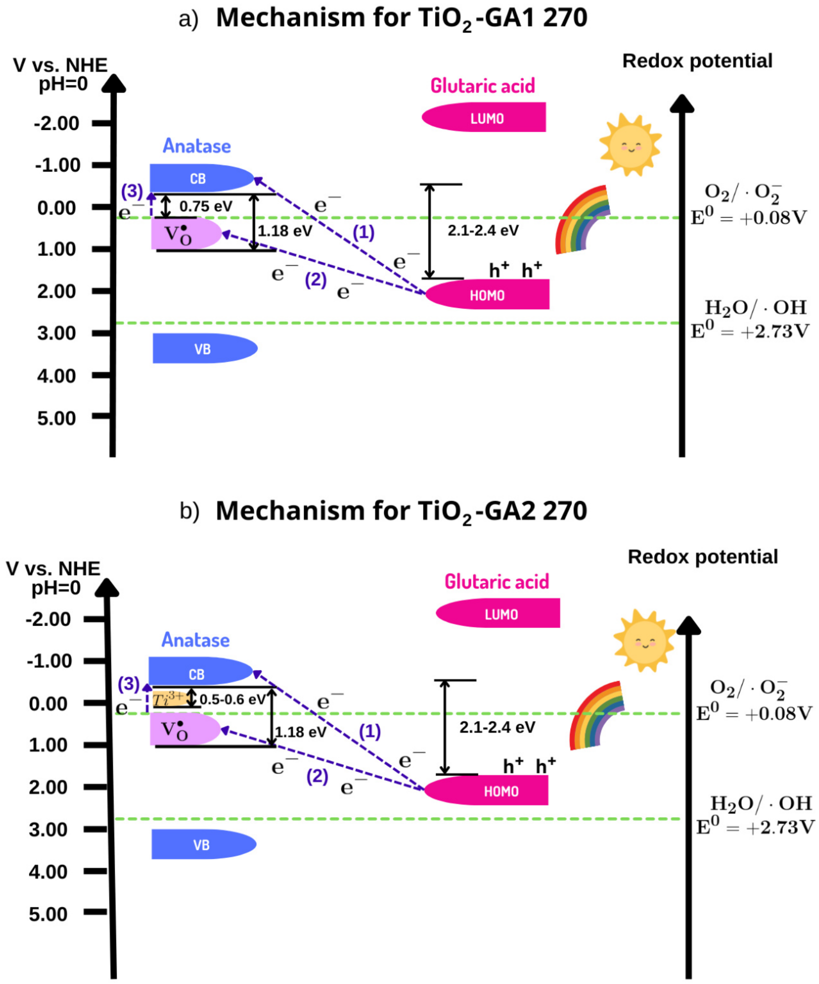

Figure 5.14: Electronic bands scheme for (**a**) TiO_2-GA1 270 and (**b**) TiO_2-GA2 270 CTCs.

5.4
Conclusions

Visible-light-sensitive TiO_2-GA nanomaterials were synthesized *via* sol-gel and calcined under static air at 270 °C. FTIR corroborated the formation of charge transfer complexes between GA organic molecule and TiO_2 through the bidentate chelating interaction.

EPR and XRPD revealed the existence of the bulk oxygen vacancies in the TiO_2-GA CTCs and indicated that the charge compensation mechanism due to the oxygen vacancies in the TiO_2-GA1 270 occurs, predominantly, through electronic compensation, while for TiO_2-GA2 270 through ionic compensation, evidencing the existence of bulk Ti^{3+} defects in the in the TiO_2-GA2 270 nanostructure by EPR measurements.

The TC photodegradation results using IPA and BQ, as scavengers, highlighted the key role of the superoxide radical in the photochemistry reactions and degradation of TC by TiO_2-GA CTCs.

It was found that the high content of GA molecules bounded to the TiO_2 surface, observed for TiO_2-GA2 270, was not beneficial for the photocatalytic performance, since the GA reduced the active sites in the nanostructure surface.

TiO_2-GA1 270 exhibited the highest photocatalytic performance in TC degradation due to the synergistic effect between an adequate content of GA bounded to the TiO_2 surface, the enhanced visible light absorption and the predominant electronic charge compensation, which improved the production of superoxide radicals by the TiO_2-GA1 270 CTC.

The findings of this work provide fundamental insights into the influence of GA, bulk Ti^{3+} defects and bulk oxygen vacancies on photocatalytic performance, lattice parameters, optical and photochemical properties of TiO_2-GA CTCs, which can be extrapolated to other CTCs.

6
General conclusions and prospects for future works

To summarize the developments related in the previous chapters, the main results of this research are described below:

- The TiO_2-ACAC CTCs, synthesized *via* sol-gel and calcined under different atmospheres (static air, Ar and H_2) exhibited different concentration of the bulk oxygen vacancies, revealing that charge compensation due to the oxygen vacancies in these CTCs occurs, predominantly, through electronic compensation.

- TiO_2-ACAC 270 exhibited the lowest concentration of bulk oxygen vacancies compared to CTCs calcined under reducing atmospheres.

- The recombination kinetics of the photogenerated charge carriers in the TiO_2-ACAC CTCs can be described as a function of the bulk oxygen vacancies concentration, since the proximity between the defects increases the charge carriers recombination rates, which causes a reduction in the ROS formation by the TiO_2-ACAC CTCs.

- The coupling between the adequate concentration of bulk oxygen vacancies and the LMCT mechanism contributed to the higher efficiency in the superoxide radical production by the TiO_2-ACAC 270 CTC and, as a consequence, to the higher photocatalytic performance in TC degradation.

- The TiO_2-GA nanopowders were synthesized *via* sol-gel, using two different synthesis processes and calcined at 270 °C. Calcined TiO_2-GA nanopowders obtained by the first synthesis method were denoted as TiO_2-GA1 270, while TiO_2-GA2 270 was assigned to the calcined TiO_2-GA nanopowders obtained by the second synthesis method.

- FTIR results proved the formation of the CTCs through bidentate chelating interaction between TiO_2 and GA.

- TiO_2-GA1 270 and TiO_2-GA2 270 exhibited different concentrations of bulk oxygen vacancies. In adittion, the EPR measurements revealed the existence of Ti^{3+} defects in the TiO_2-GA2 270 CTC, indicating that charge compensation due to oxygen vacancies in TiO_2-GA2 270 occurs, predominantly, through ionic compensation, while for TiO_2-GA1 270 takes place through electronic compensation.

- TiO_2-GA2 270 exhibited a higher content of GA molecules bounded to the TiO_2 surface compared to TiO_2-GA1 270.
- A higher production of the superoxide radical by the TiO_2-GA1 270 CTCs arises from the synergistic effect between an adequate content of GA molecules bounded to the TiO_2 surface, the enhanced visible light absorption and predominant electronic charge compensation. As a consequence, the TiO_2-GA1 270 CTC exhibited a higher photocatalytic performance in TC degradation.

Based on the general conclusions of this research, the following prospects are proposed as future works:

- Correlation of our results with electronic band structure models, previously reported, for the LMCT mechanism and oxygen vacancies in TiO_2, allowed us to propose electronic bands schemes for the TiO_2-ACAC and TiO_2-GA CTCs and also propose a recombination mechanism for the TiO_2-ACAC CTCs. In order to corroborate the models proposed in this research, the implementation of density functional theory (DFT) calculations is recommended to determine the electronic and crystalline structures of our CTCs with oxygen vacancies. Additionally, it is suggested to perform transient absorption spectroscopy (TAS) measurements to study the dynamics of photogenerated charge carriers, *i.e.*, charge carrier migration and recombination rates.
- Our findings indicated that TiO_2-ACAC and TiO_2-GA CTCs are able to degrade pollutants *via* interactions with electronic holes and principally superoxide radicals. Therefore, the use of these CTCs for the degradation of nitrogen oxides (NO_x) and for the photocatalytic hydrogen production is suggested.
- The TC photodegradation results using IPA and BQ, as scavengers, highlighted the inefficient production of hydroxyl radical by the TiO_2-ACAC and TiO_2-GA CTCs. Therefore, in order to promote the production of the hydroxyl radical, the synthesis of double Z-scheme heterojunction photocatalysts based on these CTCs looks promising.
- Considering the environmental and social approach of photocatalysis, it is suggested to carry out a synergistic theoretical and experimental study on the use of paints based on TiO_2-ACAC and TiO_2-GA CTCs in urban areas. The use of Machine Learning (ML) algorithms appears as a possibility to determine the optimal conditions for the applicability of these CTCs in urban environmental remediation.

7
Bibliography

1 BEN, Y. et al. Human health risk assessment of antibiotic resistance associated with antibiotic residues in the environment: A review. **Environmental Research**, v. 169, p. 483–493, 2019.

2 DJURISIĆ, A. B.; LEUNG, Y. H.; NG, A. M. C. Strategies for improving the efficiency of semiconductor metal oxide photocatalysis. **Mater. Horiz.**, The Royal Society of Chemistry, v. 1, p. 400–410, 2014.

3 CHRISTOFORIDIS, K. C.; FORNASIERO, P. Photocatalytic hydrogen production: A rift into the future energy supply. **ChemCatChem**, v. 9, p. 1523–1544, 2017.

4 HAGGERTY, J. E. S. et al. High-fraction brookite films from amorphous precursors. **Scientific Reports**, v. 7, p. 15232, 2017.

5 BARCZAK, M.; MCDONAGH, C.; WENCEL, D. Micro- and nanostructured sol-gel-based materials for optical chemical sensing (2005–2015). **Microchimica Acta**, v. 183, p. 2085–2109, 2016.

6 SWAMINATHAN, J.; RAVICHANDRAN, S. Insights into the electrocatalytic behavior of defect-centered reduced titania ($TiO_{1.23}$). **The Journal of Physical Chemistry C**, v. 122, p. 1670–1680, 2018.

7 ZHAO, H.; PAN, F.; LI, Y. A review on the effects of TiO_2 surface point defects on CO_2 photoreduction with H_2O. **Journal of Materiomics**, v. 3, p. 17–32, 2017. Special Issue on "Photocatalytic Materials".

8 ZHANG, G.; KIM, G.; CHOI, W. Visible light driven photocatalysis mediated via ligand-to-metal charge transfer (LMCT): an alternative approach to solar activation of titania. **Energy Environ. Sci.**, The Royal Society of Chemistry, v. 7, p. 954–966, 2014.

9 JAY, L.; CHIRWA, E.; TICHAPONDWA, S. The effect of reaction conditions on the degradation of phenol by UV/TiO_2 photocatalysis. **Chemical Engineering Transactions**, v. 76, p. 1375–1380, 2019.

10 AHMAD, F.; ZHU, D.; SUN, J. Environmental fate of tetracycline antibiotics: degradation pathway mechanisms, challenges, and perspectives. **Environmental Sciences Europe**, v. 33, p. 64, 2021.

11 CHEN, J.; POON, C. sun. Photocatalytic construction and building materials: From fundamentals to applications. **Building and Environment**, v. 44, p. 1899–1906, 2009.

12 ZHAO, J.; YANG, X. Photocatalytic oxidation for indoor air purification: a literature review. **Building and Environment**, v. 38, p. 645–654, 2003.

13 MILLS, A. et al. Photocatalytic oxidation of deposited sulfur and gaseous sulfur dioxide by TiO_2 films. **The Journal of Physical Chemistry C**, v. 111, p. 5520–5525, 2007.

14 REN, H. et al. Photocatalytic materials and technologies for air purification. **Journal of Hazardous Materials**, v. 325, p. 340–366, 2017.

15 ZHANG, H.; BANFIELD, J. F. Thermodynamic analysis of phase stability of nanocrystalline titania. **J. Mater. Chem.**, The Royal Society of Chemistry, v. 8, p. 2073–2076, 1998.

16 HERRMANN, J.-M. Heterogeneous photocatalysis: state of the art and present applications in honor of Pr. R.L. Burwell Jr. (1912–2003), former head of ipatieff laboratories, northwestern university, evanston (ill). **Topics in Catalysis**, v. 34, p. 49–65, 2005.

17 LUTTRELL, T. et al. Why is anatase a better photocatalyst than rutile? - model studies on epitaxial TiO_2 films. **Scientific Reports**, v. 4, p. 4043, 2014.

18 ZHOU, Y. et al. Synthetic organic antibiotics residues as emerging contaminants waste-to-resources processing for a circular economy in china: Challenges and perspective. **Environmental Research**, v. 211, p. 113075, 2022.

19 BARALLA, E. et al. An overview of antibiotics as emerging contaminants: Occurrence in bivalves as biomonitoring organisms. **Animals**, v. 11, p. 3239, 2021.

20 WU HAIYANG HU, Y. L.-J. Z. S.; HU, Y. H. Visible light photocatalytic degradation of tetracycline over TiO_2. **Chemical Engineering Journal**, v. 382, p. 122842, 2020.

21 LIU, M. et al. Abundance and distribution of tetracycline resistance genes and mobile elements in an oxytetracycline production wastewater treatment system. **Environmental Science & Technology**, v. 46, p. 7551–7557, 2012.

22 ORGANIZATION, W. H. Publications. **WHO report on surveillance of antibiotic consumption: 2016-2018 early implementation**. [S.l.]: World Health Organization, 2018. 113 p.

23 WANG, P.; YAP, P.-S.; LIM, T.-T. C–N–S tridoped TiO_2 for photocatalytic degradation of tetracycline under visible-light irradiation. **Applied Catalysis A: General**, v. 399, p. 252–261, 2011.

24 GOTHWAL, R.; SHASHIDHAR, T. Antibiotic pollution in the environment: A review. **CLEAN – Soil, Air, Water**, v. 43, p. 479–489, 2015.

25 TROVÓ, A. G. et al. Degradation of the antibiotic amoxicillin by photo-fenton process – chemical and toxicological assessment. **Water Research**, v. 45, p. 1394–1402, 2011.

26 KÜMMERER, K. Antibiotics in the aquatic environment – A review – Part I. **Chemosphere**, v. 75, p. 417–434, 2009.

27 MARTINEZ, L. et al. Effect of TiO_2 nanoshape on the photoproduction of hydrogen from water-ethanol mixtures over Au_3Cu/TiO_2 prepared with preformed Au-Cu alloy nanoparticles. **Applied Catalysis B: Environmental**, v. 248, p. 504–514, 2019.

28 ZHOU, C. et al. Recent advances in niobium-based semiconductors for solar hydrogen production. **Coordination Chemistry Reviews**, v. 419, p. 213399, 2020.

29 LASEK, Y.-H. Y. J.; WU, J. C. Removal of NOx by photocatalytic processes. **Journal of Photochemistry and Photobiology C: Photochemistry Reviews**, v. 14, p. 29–52, 2013.

30 ZUAREZ-CHAMBA, M. et al. Bi-based photocatalysts for bacterial inactivation in water: Inactivation mechanisms, challenges, and strategies to improve the photocatalytic activity. **Environmental Research**, v. 209, p. 112834, 2022.

31 BORUAH, B. et al. Enhanced photocatalysis and bacterial inhibition in Nb_2O_5 via versatile doping with metals (Sr, Y, Zr, and Ag): a critical assessment. **Nanoscale Adv.**, RSC, v. 1, p. 2748–2760, 2019.

32 AJIBOYE, T. O.; BABALOLA, S. O.; ONWUDIWE, D. C. Photocatalytic inactivation as a method of elimination of E. coli from drinking water. **Applied Sciences**, v. 11, 2021.

33 RICHTER, R. de; CAILLOL, S. Fighting global warming: The potential of photocatalysis against CO_2, CH_4, N_2O, CFCs, tropospheric O_3, BC and other major contributors to climate change. **Journal of Photochemistry and Photobiology C: Photochemistry Reviews**, v. 12, p. 1–19, 2011.

34 TSANG, C. H. A. et al. Titanium oxide based photocatalytic materials development and their role of in the air pollutants degradation: Overview and forecast. **Environment International**, v. 125, p. 200–228, 2019.

35 TAKASHIMA, M.; OHTANI, B. Chapter 10 - titanium(IV) oxide. In: GARCÍA-LÓPEZ, E. I.; PALMISANO, L. (Ed.). **Materials Science in Photocatalysis**. [S.l.]: Elsevier, 2021. p. 159–170. ISBN 978-0-12-821859-4.

36 KUMAR, S. G.; DEVI, L. G. Review on modified TiO_2 photocatalysis under UV/Visible light: Selected results and related mechanisms on interfacial charge carrier transfer dynamics. **The Journal of Physical Chemistry A**, v. 115, p. 13211–13241, 2011.

37 FAGAN, R. et al. A review of solar and visible light active TiO_2 photocatalysis for treating bacteria, cyanotoxins and contaminants of emerging concern. **Materials Science in Semiconductor Processing**, v. 42, p. 2–14, 2016. Materials for applications in water treatment and water splitting.

38 PAN, X. et al. Defective TiO_2 with oxygen vacancies: synthesis, properties and photocatalytic applications. **Nanoscale**, The Royal Society of Chemistry, v. 5, p. 3601–3614, 2013.

39 CHEN, S. et al. A facile approach to prepare black TiO_2 with oxygen vacancy for enhancing photocatalytic activity. **Nanomaterials**, v. 8, p. 245, 2018.

40 LI, J. et al. Synergistic effect of surface and bulk single-electron-trapped oxygen vacancy of TiO_2 in the photocatalytic reduction of CO_2. **Applied Catalysis B: Environmental**, v. 206, p. 300–307, 2017.

41 LI, G. et al. Effect of oxygen vacancies and its quantity on photocatalytic oxidation performance of titanium dioxide for NO removal. **Colloids and Surfaces A: Physicochemical and Engineering Aspects**, v. 614, p. 126156, 2021.

42 WU, S. et al. Excellent photocatalytic degradation of tetracycline over black anatase-TiO_2 under visible light. **Chemical Engineering Journal**, v. 406, p. 126747, 2021.

43 ALMEIDA, L. A. et al. The influence of calcination temperature on photocatalytic activity of TiO_2-acetylacetone charge transfer complex towards degradation of NOx under visible light. **Catalysts**, v. 10, p. 1463, 2020.

44 SANNINO, F. et al. Hybrid TiO_2–acetylacetonate amorphous gel-derived material with stably adsorbed superoxide radical active in oxidative degradation of organic pollutants. **RSC Adv.**, The Royal Society of Chemistry, v. 5, p. 93831–93839, 2015.

45 LANA-VILLARREAL, T. et al. A spectroscopic and electrochemical approach to the study of the interactions and photoinduced electron transfer between catechol and anatase nanoparticles in aqueous solution. **Journal of the American Chemical Society**, v. 127, p. 12601–12611, 2005.

46 VARAGANTI, S.; RAMAKRISHNA, G. Dynamics of interfacial charge transfer emission in small molecule sensitized TiO_2 nanoparticles: Is it localized or delocalized? **The Journal of Physical Chemistry C**, v. 114, p. 13917–13925, 2010.

47 WANG, N. et al. Visible light photocatalytic reduction of Cr(VI) on TiO_2 in situ modified with small molecular weight organic acids. **Applied Catalysis B: Environmental**, v. 95, p. 400–407, 2010.

48 SCOLAN, E.; SANCHEZ, C. Synthesis and characterization of surface-protected nanocrystalline titania particles. **Chemistry of Materials**, v. 10, p. 3217–3223, 1998.

49 SIWIŃSKA-STEFAŃSKA, K. et al. The influence of addition of a catalyst and chelating agent on the properties of titanium dioxide synthesized via the sol–gel method. **Journal of Sol-Gel Science and Technology**, v. 75, p. 264–278, 2015.

50 BOKOV, D. et al. Nanomaterial by sol-gel method: Synthesis and application. **Advances in Materials Science and Engineering**, Hindawi, v. 2021, p. 5102014, 2021.

51 NIEDERBERGER, M. Nonaqueous sol–gel routes to metal oxide nanoparticles. **Accounts of Chemical Research**, v. 40, p. 793–800, 2007.

52 HABRAN, M. et al. Visible light sensitive mesoporous nanohybrids of lepidocrocite-like ferrititanate coupled to a charge transfer complex: Synthesis, characterization and photocatalytic degradation of NO. **Journal of Photochemistry and Photobiology A: Chemistry**, v. 365, p. 133–144, 2018.

53 OSKAM, G. et al. The growth kinetics of TiO_2 nanoparticles from Titanium (IV) Alkoxide at high water/titanium ratio. **The Journal of Physical Chemistry B**, v. 107, p. 1734–1738, 2003.

54 NYAMUKAMBA, P. et al. Synthetic methods for titanium dioxide nanoparticles: A review. In: ______. [S.l.: s.n.], 2018. ISBN 978-1-78923-326-1.

55 JAYASHREE, S.; ASHOKKUMAR, M. Switchable intrinsic defect chemistry of titania for catalytic applications. **Catalysts**, v. 8, 2018.

56 NOWOTNY, J.; BAK, T.; BURG, T. Electrical properties of polycrystalline TiO_2 at elevated temperatures. electrical conductivity. **Physica status solidi (B)**, v. 244, p. 2037–2054, 2007.

57 NOWOTNY, M. K. et al. Defect chemistry of titanium dioxide. application of defect engineering in processing of TiO_2-based photocatalysts. **The Journal of Physical Chemistry C**, v. 112, p. 5275–5300, 2008.

58 SERPONE, N. Is the band gap of pristine TiO_2 narrowed by anion- and cation-doping of titanium dioxide in second-generation photocatalysts? **The Journal of Physical Chemistry B**, v. 110, p. 24287–24293, 2006.

59 CHEN, J.; LIN, L.-B.; JING, F.-Q. Theoretical study of F-type color center in rutile TiO_2. **Journal of Physics and Chemistry of Solids**, v. 62, p. 1257–1262, 2001.

60 JANOTTI, A. et al. Hybrid functional studies of the oxygen vacancy in TiO_2. **Phys. Rev. B**, American Physical Society, v. 81, p. 085212, 2010.

61 XIE, T.-H.; LIN, J. Origin of photocatalytic deactivation of TiO_2 film coated on ceramic substrate. **The Journal of Physical Chemistry C**, v. 111, p. 9968–9974, 2007.

62 ZHANG, G.; CHOI, W. A low-cost sensitizer based on a phenolic resin for charge-transfer type photocatalysts working under visible light. **Chem. Commun.**, The Royal Society of Chemistry, v. 48, p. 10621–10623, 2012.

63 MEDIĆ, M. M. et al. Enhanced photoredox chemistry in surface-modified Mg_2TiO_4 nano-powders with bidentate benzene derivatives. **RSC Adv.**, The Royal Society of Chemistry, v. 6, p. 94780–94786, 2016.

64 XUE, T.; ZHANG, Z.; ZENG, R. Photoinduced ligand-to-metal charge transfer (LMCT) of Fe alkoxide enabled C–C bond cleavage and amination of unstrained cyclic alcohols. **Organic Letters**, v. 24, p. 977–982, 2022.

65 ZAPATA-TELLO, D. L. et al. Chemical modification of titanium dioxide nanoparticles with dicarboxylic acids to mediate the uv degradation in polyethylene films. **Polymer Bulletin**, v. 77, p. 6409–6431, 2020.

66 MONTES-ZAVALA, I. et al. Rheological improvement of TiO_2 nanoparticles modified by dicarboxylic acids. **Journal of Dispersion Science and Technology**, Taylor Francis, v. 0, p. 1–13, 2021.

67 GONZÁLEZ-RODRÍGUEZ, V. et al. Improving titanium dioxide dispersion in water through surface functionalization by a dicarboxylic acid. **Journal of Dispersion Science and Technology**, Taylor Francis, v. 40, p. 1039–1045, 2019.

68 BAKRE, P. V.; TILVE, S. G. Dicarboxylic acids as soft templates for the sol-gel synthesis of mesoporous nano TiO_2 with enhanced photocatalytic activity. **ChemistrySelect**, v. 2, p. 7063–7072, 2017.

69 ZHAO, H. et al. Synthesis and biochemical applications of a solid cyclic nitrone spin trap: A relatively superior trap for detecting superoxide anions and glutathiyl radicals. **Free radical biology medicine**, v. 31, p. 599–606, 10 2001.

70 ALMEIDA, L. A. et al. TiO_2-acetylacetone as an efficient source of superoxide radicals under reduced power visible light: Photocatalytic degradation of chlorophenol and tetracycline. **Catalysts**, v. 12, p. 116, 2022.

71 ACIK, I. O. et al. Titanium (IV) acetylacetonate xerogels for processing titania films. **Journal of Thermal Analysis and Calorimetry**, v. 97, p. 39, 2009.

72 ARONNE, A. et al. Electronic properties of TiO_2-based materials characterized by high Ti^{3+} self-doping and low recombination rate of electron–hole pairs. **RSC Adv.**, The Royal Society of Chemistry, v. 7, p. 2373–2381, 2017.

73 WANG, G. et al. Hydrogen-treated TiO_2 nanowire arrays for photoelectrochemical water splitting. **Nano Letters**, v. 11, p. 3026–3033, 2011.

74 SINHAMAHAPATRA, A.; JEON, J.-P.; YU, J.-S. A new approach to prepare highly active and stable black titania for visible light-assisted hydrogen production. **Energy Environ. Sci.**, The Royal Society of Chemistry, v. 8, p. 3539–3544, 2015.

75 LEI, Y. et al. Preparation and photoluminescence of highly ordered TiO_2 nanowire arrays. **Applied Physics Letters**, v. 78, p. 1125–1127, 2001.

76 LI, S. et al. Self-trapped excitons in all-inorganic halide perovskites: Fundamentals, status, and potential applications. **The Journal of Physical Chemistry Letters**, v. 10, p. 1999–2007, 2019.

77 SANTARA, B. et al. Evidence of oxygen vacancy induced room temperature ferromagnetism in solvothermally synthesized undoped TiO_2 nanoribbons. **Nanoscale**, The Royal Society of Chemistry, v. 5, p. 5476–5488, 2013.

78 ONISHI, Y. et al. Ultrafast carrier relaxation through auger recombination in the topological insulator $\mathrm{Bi_{1.5}Sb_{0.5}Te_{1.7}Se_{1.3}}$. **Phys. Rev. B**, American Physical Society, v. 91, p. 085306, 2015.

79 YASUDA, H. et al. Spatial distribution of carriers in $SrTiO_3$ revealed by photoluminescence dynamics measurements. **Phys. Rev. B**, American Physical Society, v. 78, p. 233202, 2008.

80 SHYICHUK, A.; ZYCH, E. Oxygen vacancy, oxygen vacancy–vacancy pairs, and frenkel defects in cubic lutetium oxide. **The Journal of Physical Chemistry C**, v. 124, p. 14945–14962, 2020.

81 ADORMAA, B. B.; DARKWAH, W. K.; AO, Y. Oxygen vacancies of the TiO_2 nano-based composite photocatalysts in visible light responsive photocatalysis. **RSC Adv.**, The Royal Society of Chemistry, v. 8, p. 33551–33563, 2018.

82 KATO, K. et al. Role of oxygen vacancy in the photocarrier dynamics of WO_3 photocatalysts: The case of recombination centers. **The Journal of Physical Chemistry C**, v. 126, p. 9257–9263, 2022.

83 CHO, J. M. et al. Electron spin resonance from annealed titania nanotubes. **Applied Physics A**, v. 88, p. 751–755, 2007.

84 MAO, L. et al. A newly designed porous oxynitride photoanode with enhanced charge carrier mobility. **Nano Energy**, v. 39, p. 172–182, 2017.

85 ZHU, Q. et al. Stable blue TiO_{2-x} nanoparticles for efficient visible light photocatalysts. **J. Mater. Chem. A**, The Royal Society of Chemistry, v. 2, p. 4429–4437, 2014.

86 SCHNEIDER, J. T. et al. Use of scavenger agents in heterogeneous photocatalysis: truths, half-truths, and misinterpretations. **Phys. Chem. Chem. Phys.**, The Royal Society of Chemistry, v. 22, p. 15723–15733, 2020.

87 REN, L. et al. Defects-engineering of magnetic γ-Fe_2O_3 ultrathin nanosheets/mesoporous black TiO_2 hollow sphere heterojunctions for efficient charge separation and the solar-driven photocatalytic mechanism of tetracycline degradation. **Applied Catalysis B: Environmental**, v. 240, p. 319–328, 2019.

88 NOSAKA, Y.; NOSAKA, A. Y. Generation and detection of reactive oxygen species in photocatalysis. **Chemical Reviews**, v. 117, p. 11302–11336, 2017.

89 DVORANOVÁ, D.; BARBIERIKOVÁ, Z.; BREZOVÁ, V. Radical intermediates in photoinduced reactions on TiO_2 (an EPR spin trapping study). **Molecules**, v. 19, p. 17279–17304, 2014.

90 KOPPENOL, W.; BUTLER, J. Mechanism of reactions involving singlet oxygen and the superoxide anion. **FEBS Letters**, v. 83, p. 1–6, 1977.

91 KONOVALOVA, T. A.; LAWRENCE, J.; KISPERT, L. D. Generation of superoxide anion and most likely singlet oxygen in irradiated TiO_2 nanoparticles modified by carotenoids. **Journal of Photochemistry and Photobiology A-chemistry**, v. 162, p. 1–8, 2004.

92 CHEN, J. et al. Ti^{3+} self-doped dark rutile TiO_2 ultrafine nanorods with durable high-rate capability for lithium-ion natteries. **Advanced Functional Materials**, v. 25, p. 6793–6801, 2015.

93 MIRZAEI, A. et al. Black TiO_2 nanotube array/$BiVO_4$ heterojunction photocatalysts for tetracycline removal with high solution detoxification efficiency. **ACS Applied Nano Materials**, v. 5, p. 7161–7174, 2022.

94 NAKAMURA, I. et al. Role of oxygen vacancy in the plasma-treated TiO_2 photocatalyst with visible light activity for NO removal. **Journal of Molecular Catalysis A-chemical**, v. 161, p. 205–212, 2000.

95 CRONEMEYER, D. C. Infrared absorption of reduced rutile TiO_2 single crystals. **Phys. Rev.**, American Physical Society, v. 113, p. 1222–1226, 1959.

96 Von Oertzen, G. U.; GERSON, A. R. The effects of O deficiency on the electronic structure of rutile TiO_2. **Journal of Physics and Chemistry of Solids**, v. 68, p. 324–330, 2007.

97 GUAN, D. et al. Aerosol synthesis of trivalent titanium doped titania/carbon composite microspheres with superior sodium storage performance. **Nano Research**, v. 10, p. 4351–4359, 2017.

98 XU, Y. et al. Introducing Ti^{3+} defects based on lattice distortion for enhanced visible light photoreactivity in TiO_2 microspheres. **RSC Adv.**, The Royal Society of Chemistry, v. 7, p. 32461–32467, 2017.

99 DIAZ, E. C. M. et al. Extrinsic point defects in low-positive thermal expansion $Al_2W_3O_{12}$ and their effects on thermal and optical properties. **Inorganic Chemistry**, v. 61, p. 14086–14094, 2022.

100 MITRA, T.; SAILAKSHMI, G.; GNANAMANI, A. Could glutaric acid (GA) replace glutaraldehyde in the preparation of biocompatible biopolymers with high mechanical and thermal properties? **Journal of Chemical Sciences**, v. 126, p. 127–140, 2014.

101 GONZÁLEZ-CALDERÓN, J. et al. Functionalization of multi-walled carbon nanotubes (MWCNTs) with pimelic acid molecules: effect of linkage on β-crystal formation in an isotactic polypropylene (iPP) matrix. **Journal of Materials Science**, v. 50, 2014.

102 SUTTON, C. C. R.; DASILVA, G.; FRANKS, G. V. Modeling the IR spectra of aqueous metal carboxylate complexes: Correlation between bonding geometry and stretching mode wavenumber shifts. **Chemistry – A European Journal**, v. 21, p. 6801–6805, 2015.

103 CASTILLO, P. C. H. D.; MANUEL, S. R.; RUIZ, F. An easy and efficient method to functionalize titanium dioxide nanoparticles with maleic anhydride. **Soft Nanoscience Letters**, Scientific Research Publishing, v. 4, p. 53–62, 2014.

104 MA, L.-J.; WU, Y. FTIR spectroscopic study on the interaction between a fluoroionophore and metal ions. **Anal. Sci.**, Springer Science and Business Media LLC, v. 23, p. 799–802, 2007.

105 MA, Y. et al. Bidentate carboxylate linked TiO_2 with NH_2-MIL-101(Fe) photocatalyst: a conjugation effect platform for high photocatalytic activity under visible light irradiation. **Science Bulletin**, v. 65, p. 658–669, 2020.

106 THOMAS, A. G.; SYRES, K. L. Adsorption of organic molecules on rutile TiO_2 and anatase TiO_2 single crystal surfaces. **Chem. Soc. Rev.**, The Royal Society of Chemistry, v. 41, p. 4207–4217, 2012.

107 MILIĆEVIĆ, B. et al. Charge-transfer complex formation between TiO_2 nanoparticles and thiosalicylic acid: A comprehensive experimental and dft study. **Optical Materials**, v. 73, p. 163–171, 2017.

108 KIM, G.; LEE, S.-H.; CHOI, W. Glucose–TiO_2 charge transfer complex-mediated photocatalysis under visible light. **Applied Catalysis B: Environmental**, v. 162, p. 463–469, 2015.

109 SAINI, C. P. et al. Impact of self-trapped excitons on blue photoluminescence in TiO_2 nanorods on chemically etched Si pyramids. **The Journal of Physical Chemistry C**, v. 121, p. 11448–11454, 2017.

110 LIU, J. et al. Structure and photoluminescence study of TiO_2 nanoneedle texture along vertically aligned carbon nanofiber arrays. **The Journal of Physical Chemistry C**, v. 112, p. 17127–17132, 2008.

111 CUI, X. et al. Facile regulation of crystalline phases and exposed facets on Ti^{3+} self-doped TiO_2 for efficient photocatalytic hydrogen evolution. **Journal of Materials Science**, v. 51, p. 10819–10832, 2016.

112 BHARTI BANDNA; KUMAR, S. L. H.-N.; KUMAR, R. Formation of oxygen vacancies and Ti^{3+} state in TiO_2 thin film and enhanced optical properties by air plasma treatment. **Scientific Reports**, v. 6, p. 32355, 2016.

113 WEN, P. et al. Ti^{3+} self-doped TiO_2 as a photocatalyst for cyclohexane oxidation under visible light irradiation. **Journal of Materiomics**, v. 5, p. 696–701, 2019.

114 QIU, J. et al. Correlation of Ti^{3+} states with photocatalytic enhancement in TiO_2-passivated p-GaAs. **Journal of Catalysis**, v. 337, p. 133–137, 2016.

115 REN, R. et al. Controllable synthesis and tunable photocatalytic properties of Ti^{3+}-doped TiO_2. **Scientific Reports**, v. 5, p. 10714, 2015.

116 RAHMAN, K. A. et al. Toward sustainable energy: photocatalysis of Cr-doped TiO_2: 1. electronic structure. **Ionics**, v. 24, p. 309–325, 2018.

117 AMANO, F. et al. Effect of Ti^{3+} ions and conduction band electrons on photocatalytic and photoelectrochemical activity of rutile titania for water oxidation. **The Journal of Physical Chemistry C**, v. 120, p. 6467–6474, 2016.

A

Supplementary information to support section 4.2

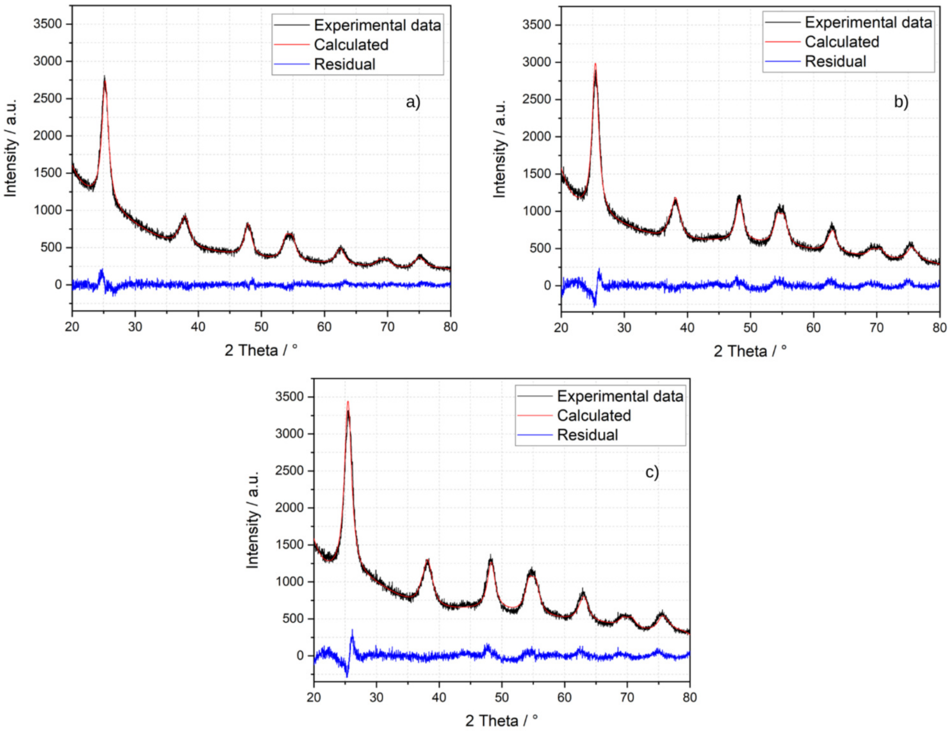

Figure S1: Rietveld refinement of the XRPD pattern of TiO_2-ACAC CTCs. (**a**) TiO_2-ACAC 270, (**b**) TiO_2-ACAC Ar 270 and (**c**) TiO_2-ACAC H_2 270. The black line stands for experimental patterns, red for adjusted and blue for the differences between the two patterns.

Table S1: Lattice parameters and mean crystalline sizes of TiO_2-ACAC 270, TiO_2-ACAC Ar 270 and TiO_2-ACAC H_2 270, obtained by the Rietveld refinement.

Sample	**a (Å)**	**c (Å)**	**Unit-cell volume (Å^3)**	**Mean crystallite size (nm)**
TiO_2-ACAC 270	3.8006 ± 0.0005	9.5130 ± 0.0024	137.42 ± 0.05	4.53 ± 0.06
TiO_2-ACAC Ar 270	3.7746 ± 0.0005	9.4540 ± 0.0021	134.70 ± 0.04	4.62 ± 0.05
TiO_2-ACAC H_2 270	3.7696 ± 0.0004	9.4450 ± 0.0020	134.22 ± 0.04	4.17 ± 0.04

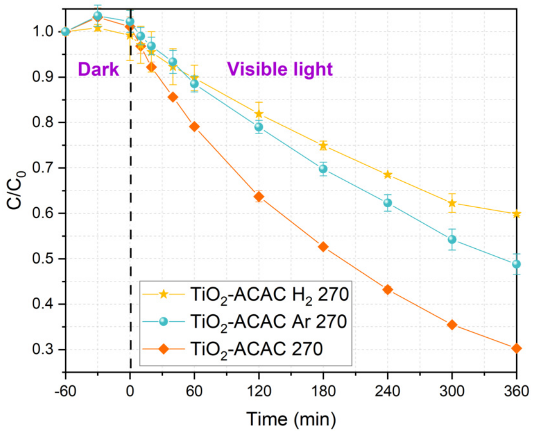

Figure S2: Adsorption-desorption equilibrium (1 h in dark) and TC photocatalytic degradation curves in the presence of TiO_2-ACAC CTCs as photocatalysts.

B
Supplementary information to support section 5.2

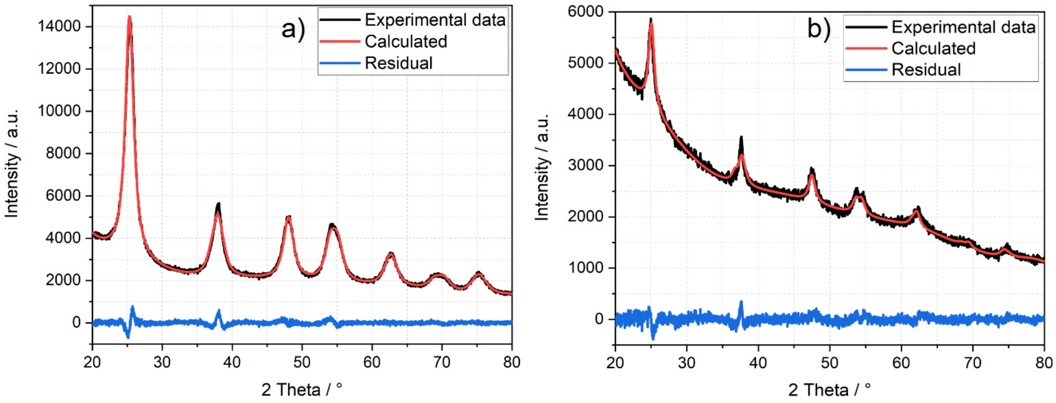

Figure S3: Rietveld refinement of the XRPD patterns of (**a**) TiO_2-GA1 270 and (**b**) TiO_2-GA2 270. The black line stands for experimental patterns, red for adjusted and blue for the differences between the two patterns.

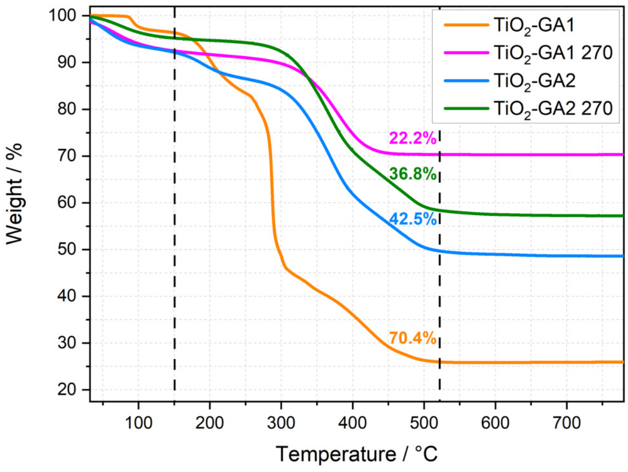

Figure S4: TGA curves of TiO_2-GA1, TiO_2-GA2, TiO_2-GA1 270 and TiO_2-GA2 270. The vertical dashed lines mark the temperature range related to the overall mass loss of GA. The percentages represent the total mass loss of GA in the temperature range from 150 °C to 522 °C.

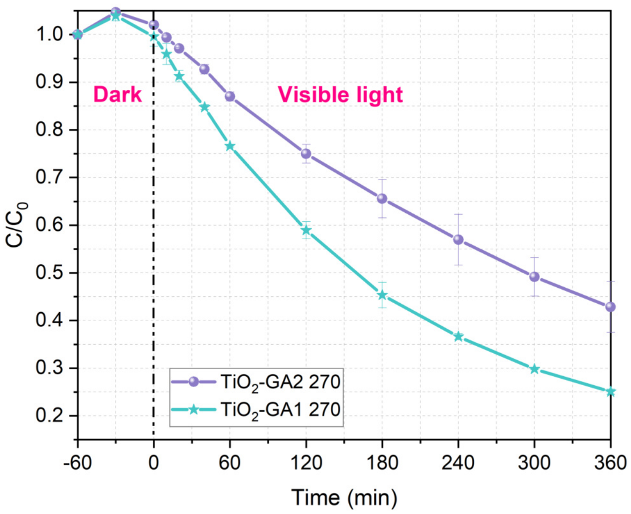

Figure S5: Adsorption-desorption equilibrium (1 h in dark) and TC photodegradation curves using TiO_2-GA1 270 and TiO_2-GA2 270 CTCs as photocatalysts.

C
Scientific production and participation in scientific events

C.1
Scientific production

The results of this study are part of two articles:

- Article submitted to Inorganic Chemistry of the American Chemical Society (ACS), classified as A1 in Qualis Capes, Manuscript ID ic-2022-04016m:

  Extrinsic Point Defects in TiO_2-Acetylacetone Charge Transfer Complex and Their Effects on Optical and Photochemical Properties

  Jessica Gil-Londoño [1], Klaus Krambrock[2], Raphaela de Oliveira [2], Marco Cremona [3], Marcelo E. H. Maia da Costa [3] and Bojan A. Marinkovic[1,*]

  [1] Department of Chemical and Materials Engineering, Pontifical Catholic University of Rio de Janeiro (PUC-Rio), Rio de Janeiro 22453-900, Brazil
  [2] Department of Physics, Federal University of Minas Gerais, 31270-901 Belo Horizonte, MG, Brazil
  [3] Department of Physics, Pontifical Catholic University of Rio de Janeiro (PUC-Rio), Rio de Janeiro 22453-900, Brazil

- Article to be submitted:

  Functionalization of Anatase Nanoparticles with Glutaric Acid and Their Photochemical and Photocatalytic Properties Under Visible Light

  Jessica Gil-Londoño [1], Marco Cremona[2], Klaus Krambrock [3], Marcelo E. H. Maia da Costa [2] and Bojan A. Marinkovic[1,*]

  [1] Department of Chemical and Materials Engineering, Pontifical Catholic University of Rio de Janeiro (PUC-Rio), Rio de Janeiro 22453-900, Brazil
  [2] Department of Physics, Pontifical Catholic University of Rio de Janeiro (PUC-Rio), Rio de Janeiro 22453-900, Brazil
  [3] Department of Physics, Federal University of Minas Gerais, 31270-901 Belo Horizonte, MG, Brazil

C.2
Participation in scientific events

Some of the results of this research were presented at the following conferences:

★ XI Regional congress of optics - CReO 2022, Ensenada, México.

CReO
XI Congreso Regional de Óptica

El capítulo estudiantil OSA/SPIE-CICESE otorga el presente

RECONOCIMIENTO

A: Jessica Gil Londoño

Por su participación en la sesión de ponencias orales en el
XI CONGRESO REGIONAL DE ÓPTICA - CReO 2022

Llevado a cabo del 21 al 23 de septiembre del 2022

Dannareli B.O
M. en C. Dannareli Barron Ortiz
Presidenta del capítulo estudiantil
OPTICA/SPIE-CICESE

Dr. Jacob Licea
Tutor OPTICA

Ruiz
Dr. Victor Ruiz Cortés
Tutor SPIE

CONACYT SPIE. STUDENT CHAPTER CICESE CICESE Student Chapter OPTICA Formerly OSA

Figure S6: Oral presentation at the XI Regional congress of optics (CReO 2022), Ensenada, México.

★ XI Tenth Serbian Ceramic Society Conference »Advanced Ceramics and Application«,Belgrade, Serbia.

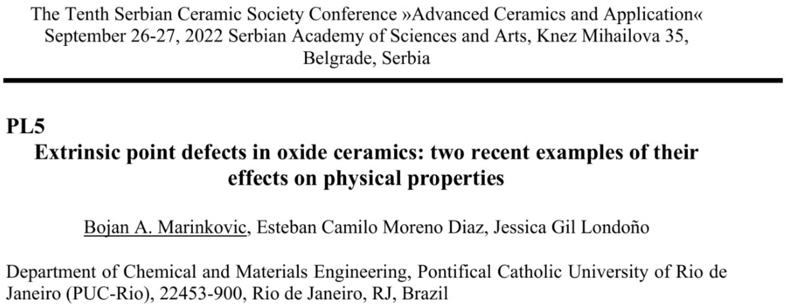

The Tenth Serbian Ceramic Society Conference »Advanced Ceramics and Application«
September 26-27, 2022 Serbian Academy of Sciences and Arts, Knez Mihailova 35,
Belgrade, Serbia

PL5
Extrinsic point defects in oxide ceramics: two recent examples of their effects on physical properties

Bojan A. Marinkovic, Esteban Camilo Moreno Diaz, Jessica Gil Londoño

Department of Chemical and Materials Engineering, Pontifical Catholic University of Rio de Janeiro (PUC-Rio), 22453-900, Rio de Janeiro, RJ, Brazil

Figure S7: Oral presentation at the Tenth Serbian Ceramic Society Conference »Advanced Ceramics and Application«,Belgrade, Serbia.